NUREG/CR-2478
ISGS Contract/Grant Report: 1983-3
Vol. 2

A Study of Trench Covers to Minimize Infiltration at Waste Disposal Sites

NUREG/CR--2478-Vol.2

DE83 903082

Task II Report
Laboratory Evaluation and Computer Modeling of Trench Cover Design

Manuscript Completed: January 1983
Date Published: August 1983

Prepared by
T. M. Johnson, T. H. Larson, B. L. Herzog,
K. Cartwright, C. J. Stohr, S. J. Klein

Illinois State Geological Survey
Natural Resources Building
615 East Peabody Drive
Champaign, IL 61820

Prepared for
Division of Waste Management
Office of Nuclear Material Safety and Safeguards
U.S. Nuclear Regulatory Commission
Washington, D.C. 20555
NRC FIN B6965

MASTER

ACKNOWLEDGMENTS

We are grateful to David Siefken, Project Officer for the Nuclear Regulatory Commission, who gave us guidance and support throughout this study; to Henry J. H. Harris, who designed the gamma-ray attenuation unit and provided instruction in its use; and to Walter J. Morse, Anthony G. Devine, and others, who conducted tests to determine the properties of the materials. Special thanks are due to Mary Z. Glockner, Jacqueline Hannah, and Mary McGuire for their assistance in preparing this manuscript. James A. Shaffner has recently been named Project Officer for this project.

ABSTRACT

Laboratory tests were conducted on geologic materials selected for use in covers for waste disposal sites: the materials included fine-grained loess and glacial till, used in covers and liners for waste disposal sites, and various coarse-grained materials used in drainage systems associated with covers. The physical, engineering, and hydrologic properties of these materials were determined in respect to their performance in trench covers.

A dual-energy, gamma-ray attenuation apparatus was constructed to measure simultaneously the moisture content and density of a laboratory soil column. Measurements of moisture content during initial experiments indicated that moisture movement in unsaturated materials is inhibited by the presence of an interface between materials of highly contrasting texture as predicted by mathematical modeling.

One-dimensional and two-dimensional models were used for computer simulations of moisture movement through several cover designs. The modeling indicated that a layer of coarse-textured, unsaturated material overlain by a layer of fine-grained material, could serve as a barrier to moisture movement. The effectiveness of the barrier is related to the contrast in texture and saturated hydraulic conductivity between the two layers. Where moisture breakthrough does occur, the moisture content of the overlying layer is less than saturation and the pressure head at the interface is less than zero. The simulations also suggested that moisture buildup in the fine-grained layer overlying the coarse-textured layer will flow laterally downslope above the interface, prior to breakthrough.

TABLE OF CONTENTS

LIST OF FIGURES

LIST OF TABLES

I. INTRODUCTION

This report describes the initial results of the activities of the second of four tasks to be undertaken at the Illinois State Geological Survey in a 42-month study aimed at developing trench covers to minimize infiltration at shallow land burial waste disposal sites. The study was conducted under U.S. Nuclear Regulatory Commission Contract/Award NRC-02-80-074.

Included in the report are:

1. the results of laboratory tests to determine the physical, hydrologic, and engineering properties of selected natural earth materials to be used in subsequent laboratory and field experiments and in computer modeling of proposed trench cover designs

2. a description of the dual gamma-ray attenuation system for simultaneous determination of water content and density in laboratory soil columns and the preliminary results from the initial experiment involving layered soils

3. a discussion of the application and availability of mathematical models and computer programs describing the flow of moisture through variably saturated materials

4. the initial results of one-dimensional and two-dimensional computer modeling of infiltration through alternative cover designs involving single- and multi-layered covers at both the laboratory column scale and at the field scale

5. an evaluation of the properties of earth materials, the procedures used to determine those properties, and the models available to simulate factors of importance in the selection, installation, and maintenance of covers.

Further results of work performed in Task II will be included in the Task IV report. The results of Task I--A Review of Present Practices and Annotated Bibliography (Herzog et al., 1981) were published previously.

II. LABORATORY EVALUATION OF SELECTED EARTH MATERIALS

A. SELECTION OF MATERIALS

The fine-grained geologic materials selected for testing included glacial till and windblown silt (loess). These materials are common in Illinois and are likely to be used in the construction of landfill covers or liners.

The Fairgrange Till of Late Wisconsinan age was sampled in De Witt County and is fairly widespread in central Illinois. The Fairgrange is genetically related to the Tiskilwa Till, found near the disposal site in Bureau County, and consequently has physical properties similar to the Tiskilwa.

The widespread Peoria Loess, also of Late Wisconsinan age, was sampled in Madison County and Bureau County. Peoria Loess has been used as cover material at the disposal site in Bureau County.

Most of the sands tested were collected from stockpiles at the Vulcan Materials gravel pit in Champaign County. The samples denoted PS are standard size grades stockpiled at the pit. The coarse and very coarse sands were separated from torpedo sand by sieving in the laboratory. All of these sands originally were separated from a poorly-sorted (and therefore, somewhat angular) pit-run sand and gravel.

B. PHYSICAL PROPERTIES

Particle size

Samples of loess consisted of 1 to 6 percent sand, 80 to 88 percent silt, 10 to 20 percent clay-sized particles, and about 1 percent gravel sized materials, generally carbonate concretions.

The composition of glacial till is typically highly variable. The Fairgrange Till classified texturally as a loam till, has a gravel content of about 4 percent. The fine fraction (less than 2 mm) of the till averages 32 percent sand, 38 percent silt, and 30 percent clay.

Clay mineralogy

The Peoria Loess contained a characteristically high percentage of expandable (montmorillonitic) clay minerals, ranging from 30 to 50 percent of the clay mineral fraction in these samples. The remainder of the clay mineral fraction was predominantly illite; kaolinite and chlorite accounted for about 5 percent. Quartz was the predominant nonclay mineral in the loess. Significant amounts of plagioclase and potassium feldspar were also found in the loess, and there is usually more dolomite than calcite. The Fairgrange Till consisted of approximately 9 percent expandable clay minerals, 72 percent illite, and 19 percent kaolinite plus chlorite.

C. ENGINEERING PROPERTIES

Atterberg limits

The loess materials tested were marginally plastic. The loess was classified as ML or NP in the Unified Systems (ASTM D2487). Liquid limits for samples of loess were 24 to 25 percent; plastic limits were 25 to 27 percent. The plastic limits were very close to, or greater than, the liquid limits of the samples tested, and therefore would generally be considered as nonplastic materials.

Shrinkage limits of the loess samples were 24 percent. Specific gravity values approximated from the tests were 2.70 to 2.71.

After crushing, the tills were dry-sieved through a number 40 sieve. The sieved portion of the till exhibits moderate to low plasticity, and was classified as CL or CL-ML in the Unified System (ASTM D2487). The tills exhibited shrinkage limits near the plastic limit, which is at the optimum moisture content for compacted dry density. However, the natural moisture content generally approached the liquid limit which illustrates the contribution of the coarse-grained components of the well-graded till. Liquid limits varied from 22 to 26 percent. Plastic limits ranged from 12.5 to 14.8 percent, shrinkage limits ranged from 11.4 to 13 percent. Specific gravity was estimated to vary between 2.66 and 2.75.

Moisture-density relationships

Samples of loess compacted by the Standard Proctor procedure achieved moisture contents of 17 to 18.5 percent to as low as 13.5 percent, and had a maximum dry density of 105.5 to 106.5 pounds per cubic foot.

Samples of till compacted by the Modified Proctor Method had an optimum moisture content of about 8 percent and a maximum dry density of 137 pounds per cubic foot. The optimum moisture content is far less than the natural moisture content of 24 percent.

Dispersion tests

Only samples of loess were tested for dispersion characteristics. In the double hydrometer and pinhole tests, the material was found to be nondispersive.

D. HYDROLOGIC PROPERTIES

Introduction

The hydraulic behavior of unsaturated, compacted, fine-grained materials affects the performance of several types of engineering installations, including covers for waste disposal sites. Unsaturated moisture movement may be significant with respect to infiltration through trench covers.

In one of the first studies of the hydraulic conductivity of compacted, fine-grained soils, Lambe (1954) pointed out that the hydraulic conductivity of selected soils was affected by the soil composition, the chemistry of the pore fluid, the void ratio (or porosity), the soil structure, and the degree of saturation.

The influence of soil structure on the hydraulic conductivity of fine-grained soils is one of the more interesting of these factors. Several investigators (Cary et al., 1943; Lambe, 1954; and Mitchell et al., 1965) have observed much lower values of saturated hydraulic conductivity for samples compacted at moisture contents wetter than optimum moisture content (wet of optimum) than for samples compacted at moisture contents drier than optimum (dry of optimum). Lambe (1960) explained this behavior in terms of differences in soil structure (or fabric) for samples compacted at moisture contents wet or dry of optimum. Fine-grained soils compacted dry of optimum have a more flocculated structure than those compacted wet of optimum, and those compacted wet of optimum have a more dispersed structure than do those compacted dry of optimum (fig. 1). The more flocculated structure indicates a more random orientation of the soil particles and therefore larger pores--which explains the greater saturated hydraulic conductivity of fine-grained soils compacted dry of optimum (Lambe, 1960).

Direct measurement of the unsaturated hydraulic conductivity is a difficult process. It can be done (Brooks and Corey, 1964), but the current trend is to estimate the unsaturated hydraulic conductivity from the results of simpler laboratory tests. The estimates are based on the pore-size distribution of the materials (reflected by the moisture content-capillary pressure relationship during desaturation) and measurement of the saturated hydraulic conductivity. A method proposed by Marshall (1958) has been modified and evaluated in several other studies (Millington and Quirk, 1959; Green and Corey, 1971; and Elzeftawy and Cartwright, 1979). These studies have concluded that empirical methods can provide reasonable estimates of the unsaturated hydraulic conductivity. Mualem (1976, 1978) proposed an alternative method of calculating hydraulic conductivity from moisture retention curves.

Laboratory test results

The laboratory testing program consisted of standard moisture content-density tests (described in Section II-C), moisture content-capillary pressure tests, and measurements of the saturated hydraulic conductivity. The methods used for each test are described in Appendix 1.

Saturated hydraulic conductivity. The relationship between compaction moisture content, density, and saturated hydraulic conductivity for Peoria Loess and Fairgrange Till are shown on figures 2 and 3, respectively. As should be expected, much lower values of saturated hydraulic conductivity are observed for samples compacted at moisture contents higher than optimum than for samples compacted at moisture contents below optimum. Some of the decrease in hydraulic conductivity for the till sample compacted wet of optimum in figure 3 is also due to decreased sample porosity.

Values of the saturated hydraulic conductivity of various samples of sand used in this study are listed in table 1.

Table 1. Saturated hydraulic conductivity (K_s) of coarse-grained materials

Sample no.	Material	K_s(cm/sec)
PS-1	"Blend sand"--very fine to medium	1.67 x 10-5
PS-3	"Torpedo sand"--fine to very coarse	2.68 x 10-5
HT-1	Very fine to medium sand some coarse	6.75 x 10-5
CS-1	Coarse sand	2.67 x 10-4
VCS-1	Very coarse sand	7.31 x 10-4

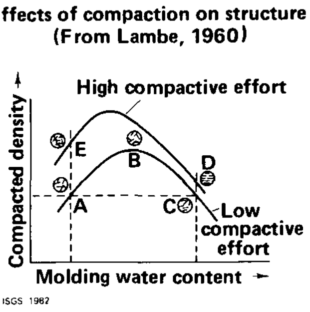

FIGURE 1. Effects of compaction on soil structure (from Lambe, 1960).

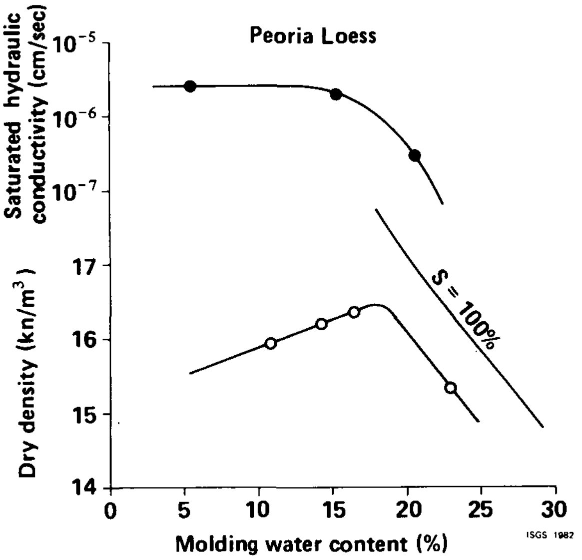

FIGURE 2. Results of compaction and saturated hydraulic conductivity tests for Peoria Loess showing decrease in hydraulic conductivity for samples compacted at moisture contents greater than optimum.

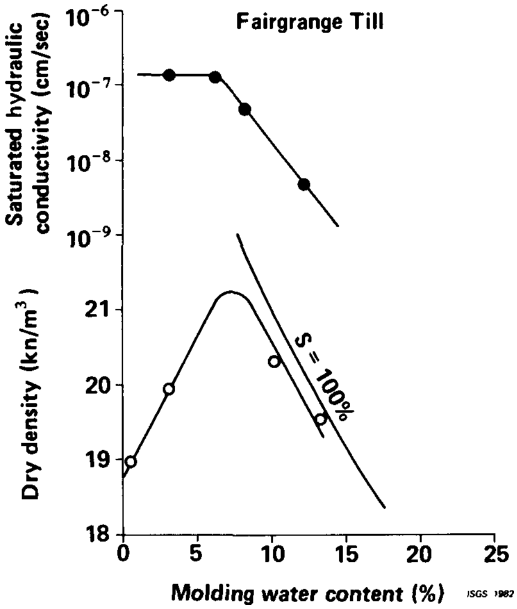

FIGURE 3. Results of compaction and saturated hydraulic conductivity tests for Fairgrange Till showing decrease in hydraulic conductivity for samples compacted at water contents wet of optimum.

Moisture content-capillary pressure relationship. Desaturation tests were conducted to determine the moisture content-retention relationship (soil-moisture characteristic curve) for each material, using Tempe cells or a pressure membrane extractor (Appendix 1). Moisture content-retention curves for samples of undisturbed till, loess, and silty sand are shown in figure 4, and curves for samples of various sands in figure 5. Soil moisture characteristic curves from Tempe cell data for samples of compacted loess and till are presented in figures 6 and 7, respectively. Figure 8 carries the curve out to three bars for the Fairgrange Till with data from the pressure membrane extractor. Samples compacted at moisture contents above optimum retain more moisture at higher pressures than samples compacted dry of optimum. The smaller pores of the samples contracted wet of optimum are not desaturated as easily as the larger pores of the samples compacted dry of optimum.

Calculation of unsaturated hydraulic conductivity

In the equations used to describe unsaturated flow, curves describing $\Psi(\Theta)$ and $K(\Theta)$ must generally be defined for each porous material considered in a model. The measurement of moisture content versus tension, $\Psi(\Theta)$, is a relatively straightforward procedure; however, the hydraulic conductivity function ($K(\Theta)$) is very difficult to measure directly. For this reason, several methods have been proposed to calculate $K(\Theta)$ from the $\Psi(\Theta)$ curve (Marshall, 1958; Millington and Quirk, 1959; Green and Corey, 1971; and Mualem, 1976, 1978). Green and Corey (1971) concluded that valid calculations of $K(\Theta)$ for a range of soil types are possible if a matching factor, typically the saturated hydraulic conductivity, is used. We have compiled several alternative methods and associated computer programs for the calculation of K as a function of pressure head, Ψ. The methods of Mualem (1978) and Green and Corey (1971) have been used in this study.

In the one-dimensional finite difference model of moisture movement (MOMOLS) used in this study (Rojstaczer, 1981), the equation of Mualem (1978) is used to calculate $K(\Theta)$. The equation is:

$$K = K_s \frac{(\Theta - \Theta_r)^n}{(\Theta_s - \Theta_r)} \qquad (1)$$

where Θ_r is the residual moisture content, K_s is the saturated hydraulic conductivity, and n is a function of the pore size distribution:

$$n = (0.015 \int_{\Theta_r}^{\Theta_s} \Psi d\Theta) + 3.0 \qquad (2)$$

Equation (1) must be employed in conjunction with an equation describing the measured values of $\Psi(\Theta)$. The available methods for describing $\Psi(\Theta)$ include the Brooks and Corey (1964) method for calculation of pore-size distribution index parameters and a method of curve fitting given by King (1965). In the one-dimensional flow model MOMOLS, an equation suggested by King (1965) is used to describe the known Ψ versus Θ curve:

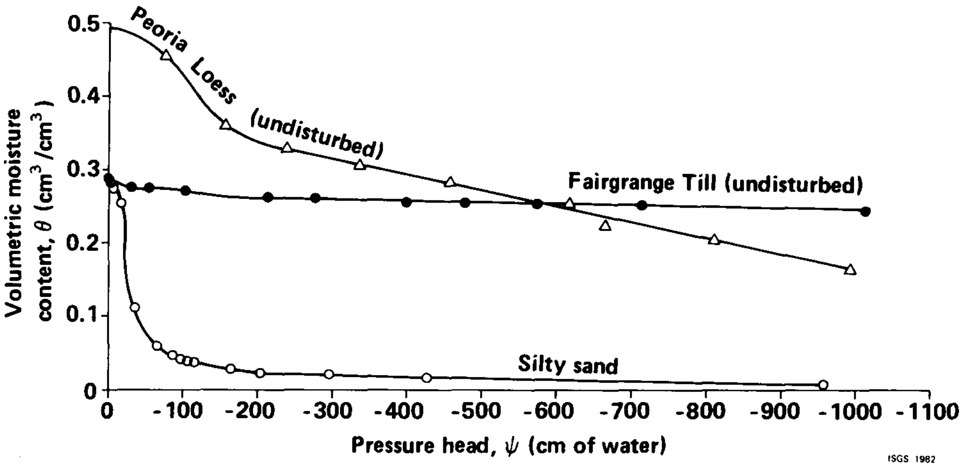

FIGURE 4. Soil-moisture retention curves for undisturbed samples of Peoria Loess and Fairgrange Till and of silty sand.

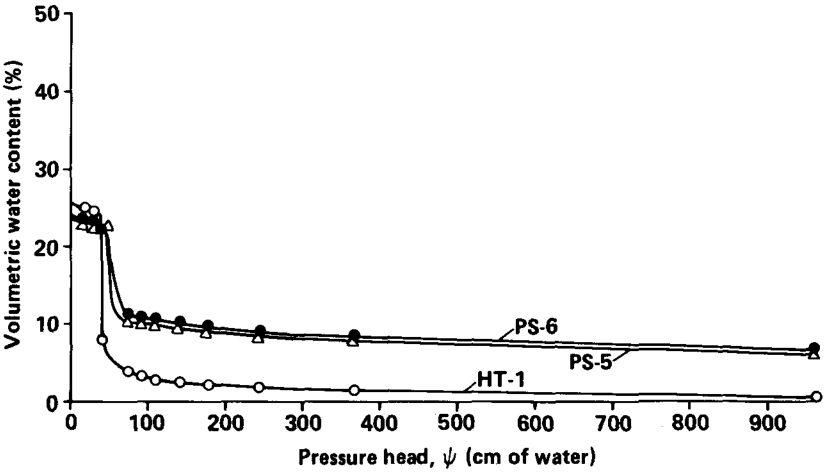

FIGURE 5. Soil-moisture retention curves for various sands. HT-1, a fine to medium sand, is used in subsequent simulations.

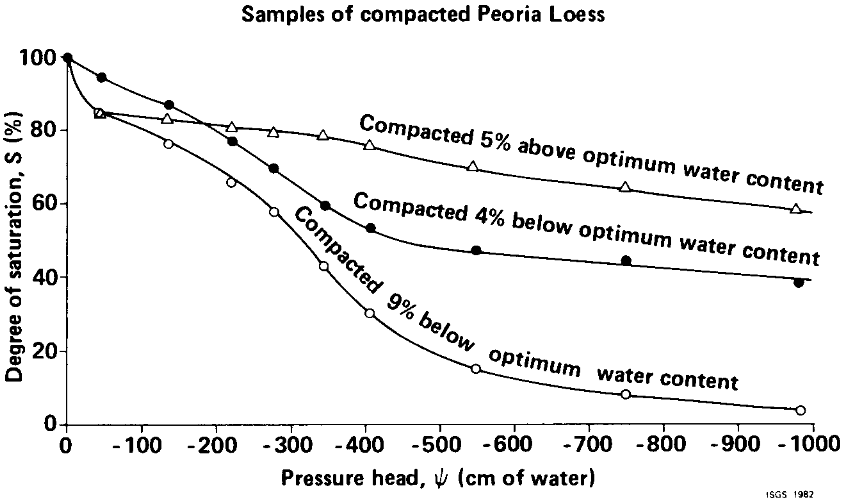

FIGURE 6. Soil-moisture retention curves for samples of compacted Peoria Loess.

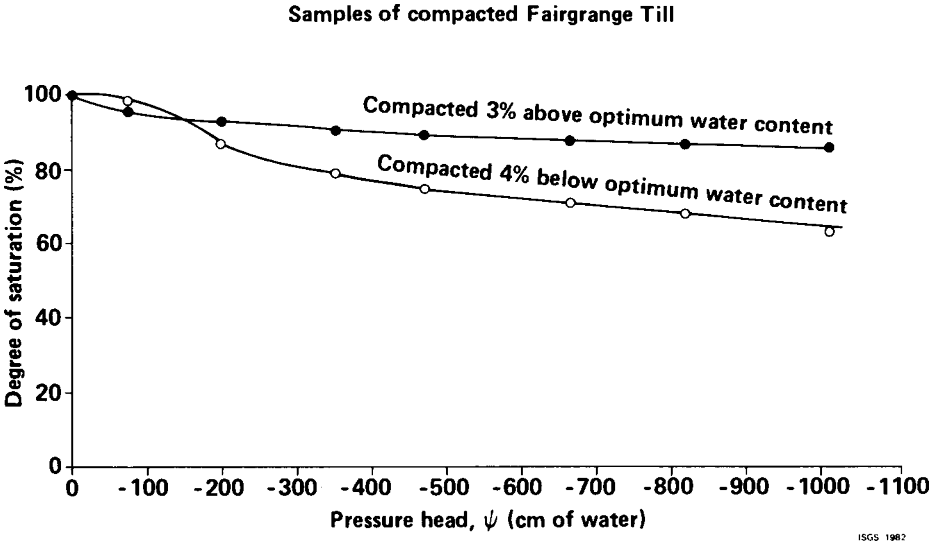

FIGURE 7. Soil-moisture retention curves for samples of compacted Fairgrange Till.

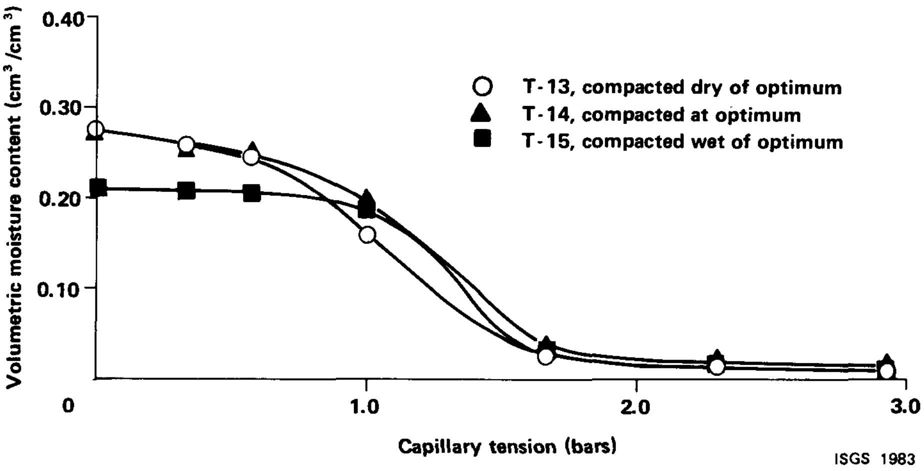

FIGURE 8. Soil-moisture retention curves for samples of compacted Fairgrange Till using the pressure membrane extractor.

$$\Theta = \Theta_s \left\{ \frac{\cosh \left[(\Psi/P_o)^{\beta} + \varepsilon \right] - \gamma}{\cosh \left[(\Psi/P_o)^{\beta} + \varepsilon \right] - \gamma} \right\} , \qquad (3)$$

where Θ_s is the saturated moisture content and P_o, β, ε, and γ are curve fitting parameters. The values of the curve-fitting parameters for each Ψ versus Θ curve are determined using a least-squares mathematical computer library routine (LMDIF1). The residual moisture content is then determined by taking the value of Θ as Ψ approaches infinity:

$$\Theta_r = \frac{\Theta_s (\cosh \varepsilon - \gamma)}{\cosh \varepsilon + \gamma} . \qquad (4)$$

KPROG, a subroutine of MOMOLS, makes all of the calculations associated with equations (1) through (4).

The preceding equations imply that Ψ and K are single-valued functions of Θ. In fact, natural soils show hysteresis in both the Ψ versus Θ and the Ψ versus K relationships (fig. 9). However, hysteresis is only slightly evident in the K versus Θ relationship for most nonswelling materials (Topp and Miller, 1966). A negligible loss of accuracy was shown to result from the simplifying assumption that K is a single-valued function of Θ.

The method of Green and Corey (1971) was used to describe the $K(\Theta)$ relationship, primarily in two-dimensional simulations of moisture movement using UNSAT2. This procedure utilizes the soil-moisture retention curve and a value for saturated hydraulic conductivity. The hydraulic conductivity is estimated by dividing the soil moisture-capillary pressure curve into m equal moisture content increments and solving the following equation at each moisture content.

$$K(\Theta)_i = \frac{K_s}{K_{sc}} \cdot \frac{30\ \gamma 2}{\rho g n} \cdot \frac{\varepsilon^{\rho}}{n^2} \sum_{j=i}^{m} (2i + 1 - 2i) h_j^{-2} \qquad (5)$$

$$i = 1, 2, \ldots, m$$

where

$K(\Theta)_i$ is the calculated conductivity for a specified water content or pressure (cm/min);
Θ is the water content (cm^3/cm^3),
i denotes the last water content class on the wet end, (e.g., k - 1 identifies the pore class corresponding to the saturated water content and i = m identifies the pore class corresponding to the lowest water content for which conductivity is calculated),
K_s/K_{sc} is the matching factor (measured saturated conductivity/calculated saturated conductivity),
γ is the surface tension of water (dynes/cm),
ρ is the density of water (g/cm^3),
g is the gravitational constant (cm/sec^2),

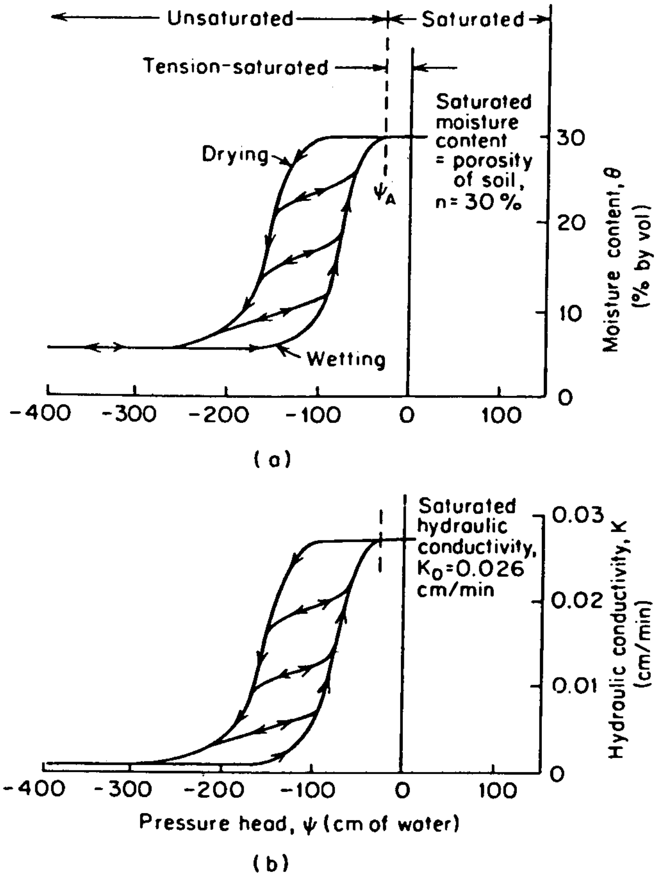

FIGURE 9. Characteristic curves relating hydraulic conductivity and moisture content to pressure head for a sand (after Liakopoulos, 1965).

η is the viscosity of water (g/cm $\sec^{-1}$),
ε is the porosity (cm^3/cm^3), equal to Θ_s,
p is a parameter that accounts for interaction of pore classes, equal to 2.0 for these calculations,
n is the total number of pore classes between $\Theta = 0$ and Θ_s, the saturated water content: $r = m \left(\frac{\Theta_s}{\Theta_s \Theta\lambda}\right)$
h_j is the pressure for a given class of water-filled pores (cm of H_2O).

The pressure is evaluated at the midpoint of each moisture content increment. A matching factor K_s/K_{sc} is used to bring the saturated hydraulic conductivity into agreement with calculated value. This essential step serves to calibrate the procedure for each soil type and yields good results (Elzeftawy and Cartwright, 1979).

The results of the hydraulic conductivity calculations as a function of degree of saturation based on the method of Green and Corey (1971) are shown in figures 10 and 11. Calculations were performed for samples compacted wet and dry of optimum for the loess and the till. The figures indicate an increasing difference in the hydraulic conductivities of soils compacted wet and dry of optimum as the soils are desaturated. When the two soils are saturated, the ratio of hydraulic conductivity of the soil compacted dry of optimum to that of the soil compacted on the wet side is 30 for loess and 26 for the till. This ratio increases to 2500 for loess and 60,000 for till when the degree of saturation drops to 80 percent.

Previous studies have shown that saturated hydraulic conductivity of fine-grained soils compacted wet of optimum moisture is much lower than that for soils compacted on the dry side. Our study has shown that this behavior is also observed in unsaturated soils and that the difference in hydraulic conductivities actually increases as the soils become less saturated.

The range of capillary pressures investigated in this study was limited to between 0 and 1000 cm of water (the observed range of capillary pressures in the field for the relatively humid eastern part of the United States). Capillary pressures in more arid regions are much greater. Although the conclusions of this study would probably be valid for more arid regions, we have not explicitly shown this.

E. DUAL GAMMA-RAY ATTENUATION SYSTEM--COLUMN EXPERIMENTS

Theory

The attenuation of monoenergetic gamma radiation at a fixed source-detector distance is described by,

$$I = I_o \exp(-\mu\rho_m x) \qquad (6)$$

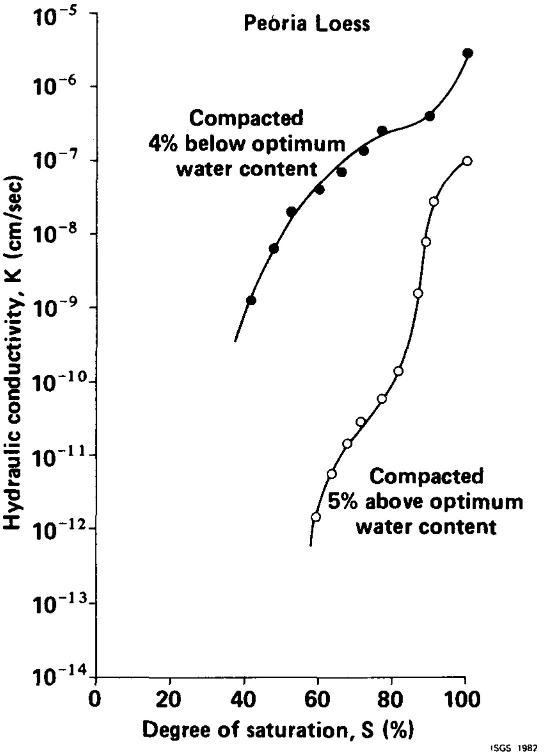

FIGURE 10. Hydraulic conductivity as a function of degree of saturation for samples of compacted Peoria Loess, calculated using method of Green and Corey (1971).

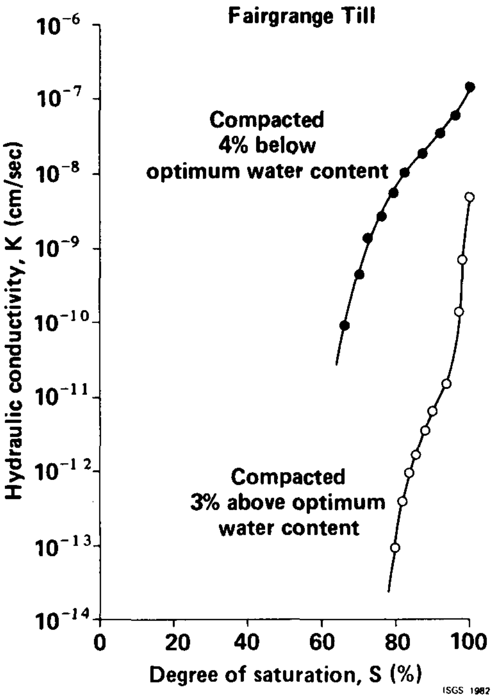

FIGURE 11. Hydraulic conductivity as a function of degree of saturation for samples of compacted Fairgrange Till, calculated using method of Green and Corey (1971).

where I_o is the radiation intensity with no interference, μ the mass adsorption coefficient (cm^2/g) of the absorber (medium) for the quantum energy of the radiation, ρ_m the density of the medium (g/cm^3), and x the thickness of the medium sample (cm). A radiation analyzer that rejects all radiation above and below a certain energy range can be used to ensure that the measured radiation is of the same energy.

Accurate experimental values of the mass adsorption coefficients of the soil and of the water are needed if equation (6) is to be used for determining density and moisture content of the soil. With these mass adsorption coefficients, equation (6) can be rewritten as

$$I = I_o \exp - (\mu_s \rho_s + \mu_w \rho_w \Theta)x \qquad (7)$$

where ρ_s is the bulk density of soil (g/cm^3), Θ is the volumetric water content (cm^3/cm^3), ρ_w is the density of water (g/cm^3) and μ_s and μ_w are the mass adsorption coefficients of oven-dry soil and water, respectively. As the water content increases, the radiation passing through the soil decreases. It is apparent from equation (7) that similar changes in bulk density of soil, ρ_s (due to swelling or frost heave), cause corresponding variation in the radiation intensity passing through the soil-water system. During the measurements of the soil-water content only, using one monoenergetic radioactive source (such as Cs^{137})--the soil bulk density ρ_s is assumed to be a constant (the soil particles do not rearrange during a wetting or drying process). However, for swelling soils or similar porous media in which pore volumes are changing during the transport of mass and heat, a second monoenergetic radioactive source (such as Am^{241}) can be used to evaluate the changes in the soil system bulk density, ρ_s. In other words, by using two equations of the form of equation (7) with two unknowns (primarily ρ_s and Θ), the pore-volume changes and the water content can be evaluated and studied independently and simultaneously.

Apparatus

A dual-energy gamma ray system, 60 KeV of Am^{241} and 660 KeV of Cs^{137}, is used as a nondestructive method to measure simultaneously the moisture content and the changes in bulk density of the porous medium during the study of the water transport. The use of a Lambert-Beer type of attenuation equation, equation (6), for each gamma energy permits determination of ρ_s and Θ (to the accuracy of ±2%) by solving the two equations simultaneously.

The two sources of radioisotopes, each containing 300 mCi of radioactive material, are housed in separate stainless steel capsules. The two source capsules are mounted coaxially inside a 25-cm cube of lead. Radiation from the cesium penetrates the americium source, and the emerging dual-energy radiation is collimated through 1.0-cm diameter holes in the lead cube into a single beam. Both source rods can be removed independently to permit selection of monoenergetic radiation from either Am or Cs. When the system is operating normally, dual-energy radiation is emitted from both radioisotopes.

A two-channel gamma-ray spectrometer system includes a scintillation sodium iodide (thallium-activated) crystal, photomultiplier tube, preamplifier detector, high-voltage power supply, linear amplifier, two single-channel pulse-height analyzers, two scaler-timers, NIM power supply, and digital printer (fig. 12). Electrical impulses produced by absorption of gamma rays in the scintillation detector are amplified and shaped to minimize the coincidence loss in the spectrometer during counting. Symmetrical square-wave bipolar electrical pulses are maintained by operating the preamplifier in the long-time constant mode and the linear amplifier in the double delay line differentiation mode. A standard delay line of 0.1 microsecond gives a pulse resolving time of 0.2 microsecond. Square-wave bipolar pulses permit measurement of high count rates but minimize detrimental effects due to high frequency noise, pile-up distortion, base line shift, timing error, and distortion due to overload effects. Elzeftawy (1974) found that adding a spectrum stabilizer between the linear amplifier and pulse-height analyzer would provide fast and accurate corrections for gain shift (as large as -50 to +100 percent), insure drift-free data acquisition over indefinitely long collection times, and compensate for the base line shift.

Channel 1 of the spectrometer is arbitrarily set to measure photons in an energy window of 40-80 KeV, and Channel 2 is set for a window of 46-860 KeV. The counts measured in Channel 1 require correction for down-scattering, coincidence interference loss due to simultaneous detection of 60 and 660 KeV photons, and coincidence loss due to pulse resolving time of the spectrometer. Counts in Channel 2 require correction only for resolving time coincidence loss.

Mass attenuation coefficients for each porous material and for each of the two energy channels can be calculated from attenuation measurements with radiation emitted from only the Am source, only the Cs source, and both sources simultaneously. The ability to remove each source independently of the other from the photon beam can provide a convenient way of calibrating the apparatus and testing the technique. Initial testing on standard material and experimental soils is accomplished with both sources in place. Attenuation coefficients for the test soils are determined by making a large number of measurements (up to 100) on individual samples packed to various known densities at known water contents.

The validity of the results is made using the standard materials, aluminum and water. Attenuation coefficients for these materials are determined and compared to published values.

Soil sample preparation

Moisture-density relationships of fine-grained materials (silt and clay) were determined with a Standard Proctor test (ASTM D698-70), and from the results the amount of material needed to achieve a particular density was calculated. Actual densities and molding moisture contents were determined after placement of the material into the test cells. These results are reported in table 2.

To determine the gamma-ray attenuation characteristics of each material, a single cell was filled with the material to be tested in four equal lifts. A modified Harvard Miniature compactor with a 16-pound spring and a square base having 2.85 cm sides was used for compaction. The number of passes made

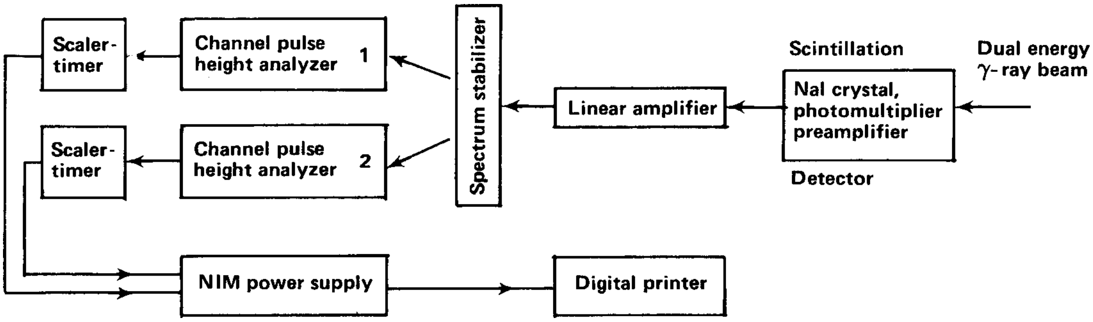

ISGS 1983

FIGURE 12. Dual gamma-ray attenuation system.

per lift varied with the density that was desired. The sands were tamped only with the compactor to avoid heaving and lateral displacement. With fine-grained material, the top of each of the first three lifts was scarified to a depth of about 3 cm to avoid the creation of layers with abnormally low hydraulic conductivities. Three runs were made at each of three densities for each material.

Table 2. Gamma Column Calibration Runs

Run No.	Unit	Dry Density (g/cm^3)	Volumetric Moisture Content (%)
FRG-1A	Fairgrange Till	2.025	25.74
FRG-1B	Fairgrange Till	2.047	24.22
FRG-1C	Fairgrange Till	2.045	23.62
FRG-2A	Fairgrange Till	1.991	22.90
FRG-2B	Fairgrange Till	1.998	26.05
FRC-2C	Fairgrange Till	2.007	25.31
FRG-3A	Fairgrange Till	1.982	26.99
FRG-3B	Fairgrange Till	2.001	26.43
FRG-3C	Fairgrange Till	1.996	25.77
PRL-1A	Peoria Loess	1.602	35.60
PRL-1B	Peoria Loess	1.637	35.16
PRL-1C	Peoria Loess	1.617	34.96
PRL-2A	Peoria Loess	1.623	35.30
PRL-2B	Peoria Loess	1.629	35.12
PRL-2C	Peoria Loess	1.616	35.12
PRL-3A	Peoria Loess	1.627	35.37
PRL-3B	Peoria Loess	1.624	35.27
PRL-3C	Peoria Loess	1.609	35.16
SND-1A	very coarse sand	1.495	6.58
SND-1B	very coarse sand	1.517	7.65
SND-1C	very coarse sand	1.531	7.69
SND-2A	coarse sand	1.569	18.55
SND-2B	coarse sand	1.575	15.75
SND-2C	coarse sand	1.550	21.03
SND-2D	coarse sand	1.548	4.95
SND-2E	coarse sand	1.560	4.88

Test run PSP-1A consisted of three soil layers in a two-cell column. The bottom layer was 10.2 cm of Peoria Loess. Over the loess was 9.1 cm of very coarse sand (VCS-1). A layer of filter fabric was placed on top of the sand. The top layer was 9 cm of Peoria Loess.

Each layer was emplaced in three lifts. The loess was compacted to a volumetric moisture content of about 36 percent (wet of optimum), and a dry density of about 1.6 g/cm^3. The sand layer was placed damp (in three lifts) and was tamped to a dry density of about 1.6 g/cm^3.

Column preparation

Calibration runs. The instrument settings, column configuration, and sampling procedure were identical for all samples tested during the calibration phase of this task. A record of this information was automatically recorded by the computer at the start of each run.

Column runs. The instrument settings used in the column runs were identical to those used in the calibration tests, except that for some column runs the counter was set for a 2-minute instead of a 1-minute count time. The column configuration and experimental procedure differed from the calibration tests, but were identical for all the column runs. As with the calibration tests, a record of the procedure was made before each column run. A sample of one such record is included as figure 13. A graphic representation of the column (fig. 14) shows the location of the various soils in the column relative to an arbitrary depth. This depth corresponds to the same depth scale used to describe the location of the column trips in the experimental protocol. Figure 14 shows the apparatus schematically with the 3-layer column in place.

Data collection and reduction procedures

Data collection. The gamma column is controlled by an Apple II microcomputer using a Pascal language program written specifically for this task. This program, GAMCOL, is available from the authors on request.

Program GAMCOL is a menu-driven program that provides for control of the gamma column. The program leads the user through the process of setting up the experiment and then runs the column and stores the data automatically. Prompt lines request detector specifications, number, and location of column stops, the order in which stops are made, time interval between stops, and speed of source/detector mechanism as it moves between stops. GAMCOL automatically starts the detector system's counter and stores the counts, depth in column, and elapsed time when the counts are completed. GAMCOL then advances the source/detector mechanism to the next programmed stop and waits a prescribed length of time before starting another count routine. When the data collection run is complete, GAMCOL signals this to the user. Data transfer to paper printer and console monitor is automatic, with disk storage provided as a user option.

Detector Specifications

H.V. power supply setting (KV): 1.1
Amplifier gain: 19.1
Shaping (μsec): 0.5

Counter/timer settings:	Channel A	Channel B
Preset (count, time, in, out)	T	0
Prescaler in or out (I or 0)	I	I
NxM:	2x1	2x1
Time base 0.1 (M or S):	M	
Connected to SCA (1 or 2):	1	

SCA 1		SCA 2	
E	↑E	E	↑E
0.6	0.2	4.8	10.0

Spectrum stabilizer:
Peak position: 5.6
Spacing: 0.05
Window width: 0.25

Description of Column

Column Trip Positions

Trip #	1	2	3	4	5	6	7	8	9	10
Depth	124	129	141	143	146	148	150	157	159	166

Experimental Procedure

The time required for the experiment (less actual sampling time) is approximately 3.74 hours.

Sampling Procedure

The speed of the blocks is set at 1.00 cm/sec.

The time interval between samples is 0.0 hrs, 0.0 mins, and 45.0 secs.

The number of sample stops is 15.
These stops will be repeated 20 times.
In temporal order and by trip number, the sample stops are:
1 2 3 6 7 3 4 5 6 7 8 9 10 6 7

Figure 13. Record of procedure for column run.

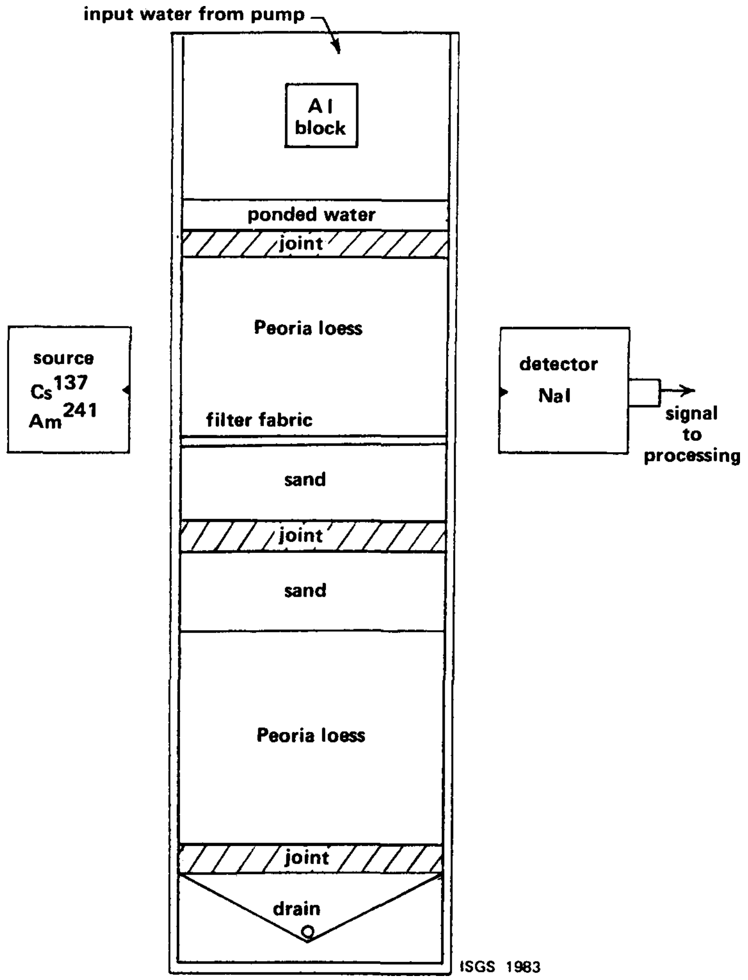

FIGURE 14. Schematic drawing of gamma column used to simultaneously determine moisture content and bulk density.

Data reduction. Several Pascal language programs (all available from the authors on request) were written to process data from the calibration and analytical runs. The most basic program, CHARACT, accepts data from prescribed data collection runs, computes intensities of detected gamma energy, and calculates simple statistics for the intensities, the standard block, and the empty slot (a portion of the column segment that does not contain soil). Output from this program includes sample size, variance, mean and standard deviation for the intensities from both sources through soil; as well as sample size and mean of the intensities from both sources through the standard block and empty slot. Because each calibration run included approximately 100 samples of measured intensity for each source through soil and then through the standard block and empty slot, this program facilitated the task of analyzing the data. The output provided the basis for most of the analyses.

Modifications to CHARACT (STAND and WAT) were written to accept data from sample runs of the standard aluminum block alone and deionized water in place of soil. Output from these programs consists of the results of the statistical analysis of the computed intensities. Attenuation coefficients calculated manually from these runs provided a comparison of this system to previously constructed gamma-ray detection systems (for which published values of attenuation coefficients for the standard materials, aluminum and water, were available). The high-energy (660 KeV) cesium attenuation coefficients computed for both standards from this system deviate less than one percent from published values. The low-energy (60 KeV) americium attenuation coefficients computed for the standard materials from this system did deviate markedly (greater than 25 percent) from published values. Implications of these findings are discussed in a subsequent section of this report.

Output from CHARACT was also used as the basis for manual calculation of cesium attenuation coefficients for the various experimental soils. These calculations incorporated intensities of cesium only.

Column runs. Actual test column runs were automatically controlled by GAMCOL, the same program used to control calibration runs. Measurements were made at the aluminum calibration block, an empty column section, and selected points in the column. Comparison of the column trip positions in figure 13 with the graphic representation of the column in figure 14 provides an example of a typical experimental set-up. Particularly close attention was paid to sample points ("trip positions") just above or below the interfaces of the column materials. These sampling locations were programmed as close to the interface as allowed by the resolution of the gamma beam (1.0 cm). The sampling sequence was designed to repeat the measurements above and below the loess/sand interface (trip positions 6 and 7) at regular, short intervals, and at the same time to measure moisture movement through the rest of the column at somewhat greater time intervals. The shorter time intervals between measurements at positions 6 and 7 provide greater resolution in the measurement of moisture movement across this critical interface.

Manual calculation of moisture content, assuming constant density, was made for portions of the column containing sand. These calculations were made from the cesium intensities and the cesium coefficients were calculated manually without regard to americium intensities or attenuation coefficients. The manual calculations were carried out only on selected measurements from each run. They were not carried out on other soil types because the assumption of constant density as hydration progresses is not valid for these clay-rich soils. However, this assumption was assumed to be valid for sand.

Results

Calibration tests. The following results (tables 3-5) were produced by CHARACT. The results of programs STAND and WAT are given in table 6.

Table 3. Intensity of gamma beam after passage through samples of Peoria Loess

Sample	Americium Intensity (counts/minute)	Cesium Intensity (counts/minute)
PRL1A	52844.6	875782
PRL1B	51626.5	864513
PRL1C	52621.7	874534
PRL2A	51757.9	866906
PRL2B	51766.6	867902
PRL2C	51235.1	864185
PRL3A	50935.2	859963
PRL3B	52153.1	871694
PRL3C	53017.8	878432

Table 4. Intensity of gamma beam after passage through samples of very coarse sand

Sample	Americium Intensity (counts/minute)	Cesium Intensity (counts/minute)
SND1A	73597.0	1078730
SND1B	70730.9	1054550
SND1C	70297.5	1055070
SND2A	66511.0	978527
SND2B	69466.4	1001990
SND2C	65454.4	969328
SND2D	73819.3	1053820
SND2E	73931.0	1055140

Table 5. Intensity of gamma beam after passage through samples of Fairgrange Till

Sample	Americium Intensity (counts/minute)	Cesium Intensity (counts/minute)
FRG1A	38692.1	744320
FRG1B	38632.4	743177
FRG1C	37900.3	735453
FRG2A	40041.1	759513
FRG2B	38878.4	745330
FRG2C	39278.8	750241
FRG3A	38977.5	747959
FRG3B	39404.7	752268
FRG3C	39688.5	755001

Table 6. Intensity of gamma beam during calibration tests

Sample	Americium Intensity (counts/minute)	Cesium Intensity (counts/minute)
Standard block	159425	1512370
Water (WAT1)	241453	1384210
Water (WAT2)	241414	1385130

Manually calculated attenuationn coefficients for the cesium source derived from the results of CHARACT are tabulated in table 7. The mean value of the attenuation coefficient was used to calculate moisture content in the column runs.

Table 7. Cesium attenuation coefficients

Soil	μ_s	Standard deviation
Sand 1 (very coarse)	0.07537	0.0002935
Sand 2 (coarse)	0.07456	0.0007587
Peoria Loess	0.07364	0.0003971
Fairgrange Till	0.07402	0.0004356
Water	0.0827	
Aluminum	0.0748	

Column runs. By assuming constant density in the sand and by using only data from the cesium source, it was possible to compute the change in moisture content in the sand. Measurements were made at both the top of the sand portion of the column (depth 150) and at the bottom of the sand portion (depth 157). In figures 15 and 16 moisture content is plotted against time on a semilogarithmic graph for both of these depths.

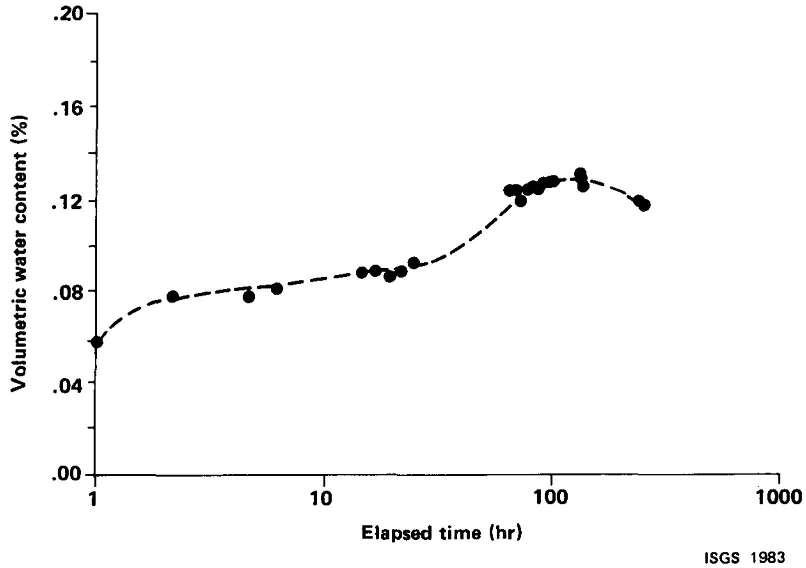

FIGURE 15. Variation of water content with time at the top of the very coarse sand (depth 150) determined by gamma-ray attenuation unit.

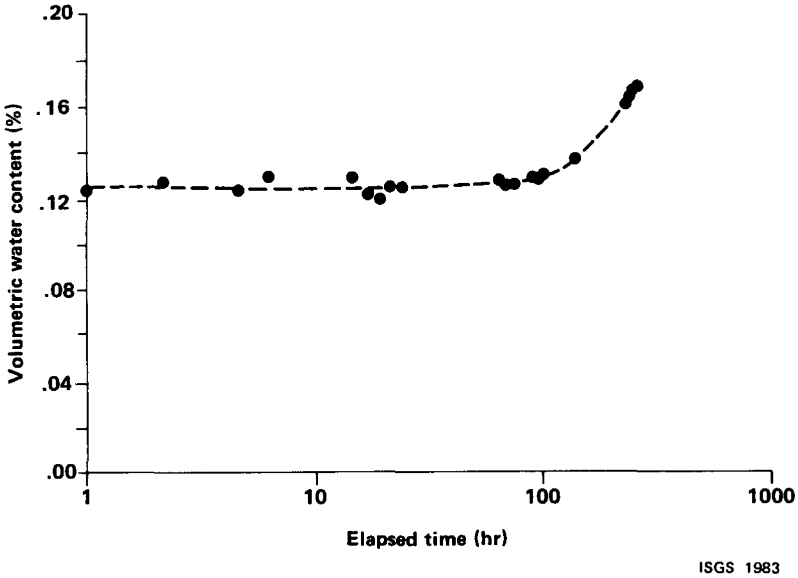

FIGURE 16. Variation of water content with time at the base of the very coarse sand (depth 157) determined by gamma-ray attenuation unit.

Discussion

The failure of the system to replicate published values of attenuation coefficients of standard materials for the low-energy americium source implies that the low-energy counts have not been sufficiently corrected for energy down-scattered from the cesium source. The phenomenon of down-scattering is discussed by Santo and Tsuji (1977) and Nofziger and Swartzendruber (1974), who suggest a method for correction. This lengthy correction procedure involves the removal of the cesium source so that measurements of the photon beam due solely to americium can be made. The present system was designed in anticipation of this procedure, which can be accomplished as necessary.

The results of the first column runs on this system, although imperfect, do provide insight into the wetting process known as the 'wick effect'. The initial moisture content was measured upon construction of the column at 6.81 percent. Assuming that initial uniformity was achieved, rapid and distinct variations developed in the column material. At the top of the sand unit, the initial water content measurement made by the gamma system agreed closely with the original value. The moisture content rose immediately to approximately 8.0 percent, where it remained with only a slight (though continual) increase for more than 25 hours. Between 25 and 65 hours the moisture content rose significantly to more than 12.5 percent. This increase corresponds to the 'break-through' time predicted from the computer simulations. After this major change in moisture content, the sand showed only slow, gradual increases in moisture for the duration of the experiment, concluding at 13.6 percent after 140 hours.

The wetting history of the base of the sand unit was quite different from that of the top of the unit. The initial gamma measurement at the base was more than 12.5 percent, and this value was maintained with only minor fluctuation for more than 60 hours. Then the moisture content began to increase at a fairly rapid rate over the remaining hours of the experiment to a value of 13.6 percent after 140 hours. This indicates that although the moisture content at the top of the sand unit may continually increase, this is not the case in the rest of the unit. In fact, after establishing an initial level, the moisture content does not vary for a considerable length of time. The moisture break-through in the upper portions of the unit occurs between 25 and 65 hours, but is not detected in the lower part of the unit until 90 hours, more than 30 hours after upper break-through.

III. MATHEMATICAL MODELING AND COMPUTER SIMULATION OF MOISTURE MOVEMENT THROUGH TRENCH COVERS

A. INTRODUCTION

The evaluation of alternative cover designs that will limit the infiltration of moisture into waste disposal sites involves the use of predictive techniques. Predictive mathematical models have been developed to describe the flow of moisture through variably saturated porous media. These models are based either on analytical solutions or on approximate numerical solutions to the equations governing moisture flow. In general, analytical solutions are available only for simple problems, whereas numerical methods are able to deal with the more complex problems typically encountered. Predictive techniques are also used to derive relationships necessary to solve the equations governing moisture flow; these relationships are derived from measurable properties of a material. For example, the variation in hydraulic conductivity, K, with moisture content, Θ, is derived from the more easily measured water content vs. pressure curve. Using specified boundary conditions and the predicted relationship between K and Θ for each material, a mathematical model can simulate the flow of moisture through individual materials and layered combinations of materials in a wide range of hypothetical problems.

In our study, models of moisture flow are being calibrated and verified using laboratory column experiments. The selection of materials to be used in alternative cover designs are based on the behavior of these materials in column experiments and in numerical simulations. In the initial stages of our study, one-dimensional models were used to evaluate many different layered systems. More sophisticated, multi-dimensional models are now being used to test selected cover designs under a variety of simulated field conditions.

B. BASIC EQUATIONS OF MATHEMATICAL MODELS

The flow of water through porous media is described using Darcy's law, which can be stated as:

$$v_z = -K\frac{\partial\phi}{\partial z}, \qquad (8)$$

where v_z is the flux in the z direction (positive downward), ϕ is the total potential, and K is the hydraulic conductivity (the measure of the ability of the material to transmit fluid). The total potential (ϕ) consists of the pressure head, Ψ, and the depth, z:

$$\phi = \Psi - z \qquad (9)$$

For unsaturated flow, Ψ is always less than zero, indicating tension; whereas, for saturated flow, $\Psi>0$.

Under saturated conditions the hydraulic conductivity, K, depends on the internal geometry of the porous medium and on the properties of the fluid. For a given saturated, homogeneous material, K is a constant. For unsaturated flow, the hydraulic conductivity of a given material is a function of volumetric water content, Θ. For a homogeneous, unsaturated material, Darcy's law thus becomes:

$$v_z = -K(\Theta)\frac{\partial\phi}{\partial z}, \qquad (10)$$

The hydraulic conductivity decreases rapidly as Θ decreases. This decrease in conductivity is caused by a reduction in water-filled pore space; the large pores, with the greatest ability to transmit fluid, are the first to empty.

The general, nonlinear, partial-differential equation describing flow in an unsaturated, rigid porous medium can be written as:

$$\frac{\partial \Theta}{\partial t} = -\nabla \cdot v, \qquad (11)$$

where ∇ is the vector differential operator and v is the velocity. If flow is vertical, equations (10) and (11) may be combined to yield the general equation for unsaturated flow through homogeneous material (Richards, 1931):

$$\frac{\partial \Theta}{\partial t} = \frac{\partial}{\partial z} \left[K(\Theta) \frac{\partial \phi}{\partial z}\right]. \qquad (12)$$

This relation, known as Richard's equation, may be expanded using Equation (9) to obtain:

$$\frac{\partial \Theta}{\partial t} = \frac{\partial}{\partial z} \left[K(\Theta) \frac{\partial \Psi}{\partial z}\right] - \frac{\partial K(\Theta)}{\partial z} . \qquad (13)$$

When Ψ and K are single-valued functions of Θ, Equation (13) can be rewritten as:

$$\frac{\partial \Theta}{\partial t} = \frac{\partial}{\partial z} \left[D(\Theta) \frac{\partial \Theta}{\partial z}\right] - \frac{\partial K(\Theta)}{\partial z} . \qquad (14)$$

with Θ as the sole dependent variable and where:

$$D(\Theta) = K(\Theta) \frac{\partial \Psi}{\partial \Theta} . \qquad (15)$$

D is also a function of Θ and is called the diffusivity.

By introducing the identity $C = \frac{\partial \Theta}{\partial \Psi}$, where C is the specific moisture capacity, Equation (13) may be written with Ψ as the sole dependent variable:

$$C(\Psi)\frac{\partial \Psi}{\partial t} = \frac{\partial}{\partial z}\left[K(\Psi)\,\frac{\partial \Psi}{\partial z}\right] - \frac{\partial K(\Psi)}{\partial z}\,. \qquad (16)$$

Either Equation (14) or (16) may be used to describe the flow of fluid through unsaturated media. Equation (16) is more versatile since it can also be used to describe flow through saturated media.

C. SOLUTION OF RICHARD'S EQUATION--METHODS

The solution to Richard's Equation can be obtained by analytical or approximate numerical methods. Analytical methods use integration or series solutions and treat space and time as continuous (Lappala, 1980); numerical methods involve discretization of space and time into finite intervals. The application of analytical solutions is limited to simple problems in homogeneous media because of the highly nonlinear character of the K versus Θ function. However, analytical solutions can be used to check the accuracy of approximate numerical methods. The quasi-analytical techniques of Philip (1957a, 1957b) have been used to check the accuracy of simulations produced by the one-dimensional numerical model MOMOLS (Rojstaczer, 1981) used in this study.

Numerical methods require subdivision of the spatial domain into discrete intervals, using either finite difference or finite element methods. In finite difference methods, the region of interest is divided into a series of regularly spaced nodes. Spatial derivatives are approximated by assuming that the solution varies linearly between nodes. Because the gradients in the solution variable are assumed to be linear between nodes, finite difference methods may require fine subdivision in problems involving rapidly changing gradients. Unstable, oscillatory solutions can also result if sharp moisture fronts are present; the addition of a numerical dispersion term and restrictions on the time-step length may be required to eliminate the instability. Thus, some problems can be very expensive to solve with the finite difference method.

The finite element method of discretization permits a much more accurate representation of a system with a complex geometry. In this method, the region of interest is subdivided into subregions (elements) that may have irregular shapes. Lappala (1980) found that finite element methods can simulate steeper moisture fronts than can finite difference methods. For linear problems with steep fronts, finite element methods are faster; however, for nonlinear problems they are slower than finite difference methods. Lappala concluded that for dry soils the finite difference method is preferred.

D. ONE-DIMENSIONAL MODEL--MOMOLS

For the simulation of one-dimensional moisture flow the finite difference approximation of Equation (14) was incorporated in the program MOMOLS (Moisture Movement in Layered Systems) developed by Rojstaczer (1981). A listing of the program is available upon request from the authors of this report. Nodal spacing in this program is constant, and a fully implicit scheme is used to evaluate the spatial and time derivatives. Required data in MOMOLS include data from the Ψ versus Θ curve in the form of the equation by King (1965), as previously described. The K versus Θ relationship is calculated in MOMOLS using the same procedure as KPROG. Both constant flux and constant pressure head boundary conditions can be included in MOMOLS. For a layered system the flux across the interface of the layers is calculated. The program also indicates when significant moisture across the boundary occurs.

Simulations of one-dimensional flow indicate the response of a variety of materials under simplified conditions such as those encountered in laboratory column experiments. These simulations are easily constructed and are relatively inexpensive to run. However, the extension to field-scale problems--involving irregular geometries and more complex boundary conditions such as those typically encountered in cover design--requires the use of more sophisticated, multi-dimensional methods.

E. MULTI-DIMENSIONAL MODELS

Numerous models have been developed to simulate moisture transport in multi-dimensional systems under variably saturated conditions (Lappala, 1980). The numerical models are generally either of the finite difference or finite element types described previously. Several multi-dimensional numerical models have been selected and compiled for evaluation of their applicability to the simulation of moisture transport through layered cover systems. The models currently on computer file are:

1. UNSAT2 (Neuman, 1973; Neuman et al., 1975)
   A Galerkin, finite-element, 2-dimensional model that allows for evaporation, transpiration, and all types of boundary conditions. This model has been verified, using field and lab data and comparison with analytical and other numerical models.

2. Lappala (1981, in press)
   A finite-difference, 2-dimensional model that allows for root extraction and evaporation as well as all boundary conditions. This model has also been verified with other numerical models and analytical solutions. The model has not yet been published, but a draft user's manual is available.

3. Reeves and Duguid (1975)
   A Galerkin, finite-element, 2-dimensional model that allows for all boundary conditions. Although this model has been calibrated with other FD models and field data, some very nonlinear problems have not been solvable.

4. Femwater (Yeh and Ward, 1980)
   A modified version of the Reeves and Duguid (1975) model that is more applicable to nonlinear problems. A detailed, supplementary users manual prepared by Yeh (1982) for the USNRC makes the application of the model quite straightforward.

Although the following models are not currently on computer file, copies of each program have been obtained:

1. TRUST (Narasimhan, 1975)
   An integrated, finite-difference, 2-dimensional model that includes all boundary conditions plus hysteresis and allows for deformable media. The program is reported to be slow. A listing has been obtained.

2. FLUMP (Neuman and Narasimhan, 1977)
   A Galerkin, finite-element, 2-dimensional model that has been verified with lab data, FD models, and analytical solutions; it is otherwise very similar to TRUST. A listing has been obtained.

3. TRANSAT (Pickens, Gillham and Cameron, 1979)
   A Galerkin, finite-element, 2-dimensional model that has been verified with lab data, FD models and analytical solutions. The model does not allow source or sink terms but incorporates solute transport. A card deck has been obtained.

The finite-element model UNSAT2 developed by Neuman (1973) and Neuman et al. (1975) has been used in this study to model two-dimensional moisture movement through alternative cover designs. A description of the model and the results of the initial simulations are presented in a subsequent section of this report.

F. RESULTS OF ONE-DIMENSIONAL SIMULATIONS

Initial one-dimensional initial simulations by Rojstaczer (1981)

<u>Description of initial one-dimensional simulations</u>. Moisture movement was simulated initially by Rojstaczer (1981) using a layered, vertical column of fine or medium textured soil underlain by a coarse gravel. The column was 50 cm long, the interface was at a depth of 24 cm, and nodal spacing was 2 cm. Two soils were used as overlying layers: the Rideau clay loam and the Rubicon sandy loam. Data on the saturated conductivities and Ψ vs Θ relationships for these two soils were obtained from the experiments of Topp (1969, 1973). Two different types of underlying material were also used: a hypothetical gravel with a saturated conductivity of 10 cm/sec (gravel A) and a

hypothetical material that was identical to gravel A in its internal geometry but had a saturated conductivity of only 1 cm/sec (gravel B). Gravel B, also hypothetical, was used to gauge the effect of underlying conductivity on moisture movement at the interface.

In this study the phenomenon of hysteresis was ignored and only the primary wetting curves were used. Since all of the simulations involved cases in which hysteresis had little or no effect, the use of this simplification appeared valid. Figure 17 shows the known primary wetting curves for the soils and the postulated wetting curve for the gravels. The conductivity functions for the two soils and gravel B are shown in figure 18 which indicates that the saturated conductivity of the clay loam is actually greater than that of the sandy loam.

Three basic types of simulations were run, each defined by its own surface boundary condition. Case 1 simulated flow in response to rainfall at a constant rate of .0007 cm/sec.

$$-K\frac{\partial\phi}{\partial z} = .0007; \; z = 0; \; t > 0 \qquad (17)$$

Case 2 modeled flow in response to a period of rainfall (at the same rate as in the previous case) followed by a period of no rainfall.

$$-K\frac{\partial\phi}{\partial z} = .0007, \; z = 0; \; 0 < t < t_1 \qquad (18)$$

$$-K\frac{\partial\phi}{\partial z} = 0.0, \; z = 0; \; t > t_1 \qquad (19)$$

Case 3 simulated flow in response to a prescribed pressure head of zero at the surface.

$$\Psi(0,t) = 0.0; \; t > 0 \qquad (20)$$

For all three cases the initial condition was uniform throughout space

$$\Psi(z,0) = \Psi_{in} = -300\text{cm}; \; 0 < z < L \qquad (21)$$

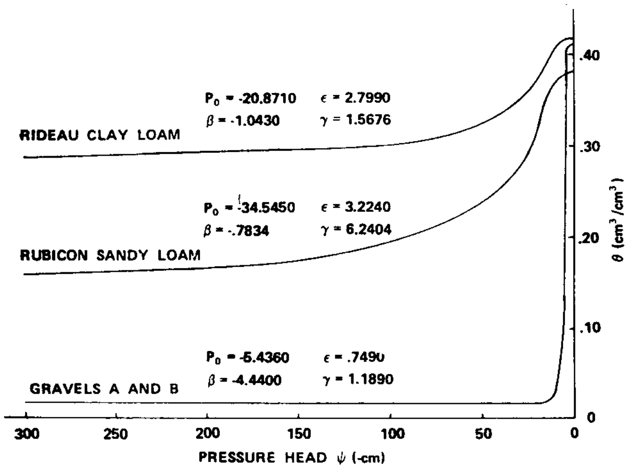

FIGURE 17. Primary wetting curves for soils used in MOMOLS one-dimensional simulations.

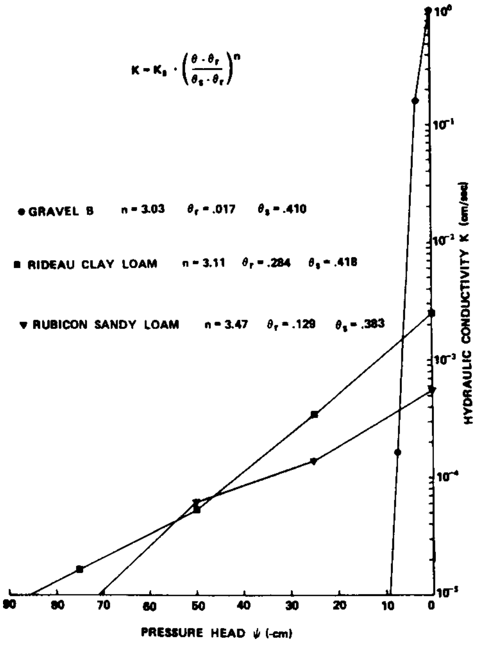

FIGURE 18. Hydraulic conductivity functions for soils used in MOMOLS one-dimensional simulations.

and a prescribed head equal to that of Ψ_{in} was used as the lower boundary condition

$$\Psi(L,t) = -300\text{cm};\ t > 0 \qquad (22)$$

These conditions eliminated the effects of hysteresis in Cases 1 and 3 and suppressed them in Case 2.

Discussion of results of initial one-dimensional simulations. The simulations showed clearly that the coarse, unsaturated material impeded moisture movement. In all simulations, progress of the moisture front temporarily or permanently ceased once the interface was reached. The lack of moisture movement across the interface caused pressure potentials and moisture contents to build in the overlying layer. Pressure and moisture build-up continued until either a static pressure profile was established (and all moisture movement ceased) or interfacial pressures achieved a critical maximum value Ψ_c. If Ψ_c was reached at the interface, the moisture front rapidly progressed into the coarse layer. The rapid infiltration into the gravel depleted moisture storage at and directly above the interface and, as a result, pressures at the interface quickly dropped from Ψ_c to a value that was more or less maintained throughout the rest of the simulation.

The critical pressure Ψ_c necessary to allow moisture movement across the interface was less than zero in all but two simulations. Deviations from zero were greater than could be attributed to computational error. In all simulations the value of Ψ_c was found to be a function of two factors; the rate at which moisture and pressure build-up was occurring in the overlying layer and the conductivity of the underlying gravel. The dependence of Ψ_c on these factors can be easily shown in a case-by-case analysis of the simulations.

Four simulations were run for Case 1 (constant flux of .0007 cm/sec). Moisture breakthrough across the interface occurred in all the simulations, and Ψ_c values varied from -5.8 cm to -3.7 cm (corresponding Θ values varied from 98.1% to 99.5% of total saturation). Variations in interfacial head values with time for the simulations, shown in figures 19 and 20, follow the general pattern outlined previously. Comparison of the interfacial Ψ values for columns that have an upper layer of clay loam with those that have an upper layer of sandy loam indicated that all other factors being equal, Ψ_c values were higher for the clay loam column. The greater pressure and moisture build-up in the clay loam columns was related to the higher conductivity of the overlying coarse material. Since the coarse material was a better transmitter of water, moisture movement and build-up occurred at a more rapid rate. Correlation between high Ψ_c values and high rates of moisture movement was also found in the other two cases.

Comparison between columns that contained gravel A and gravel B indicated that moisture build-up and Ψ_c values were also enhanced by the presence of an underlying layer with comparatively low conductivity. This observation, which was not surprising, indicated the degree that moisture movement was governed by conductivity gradients.

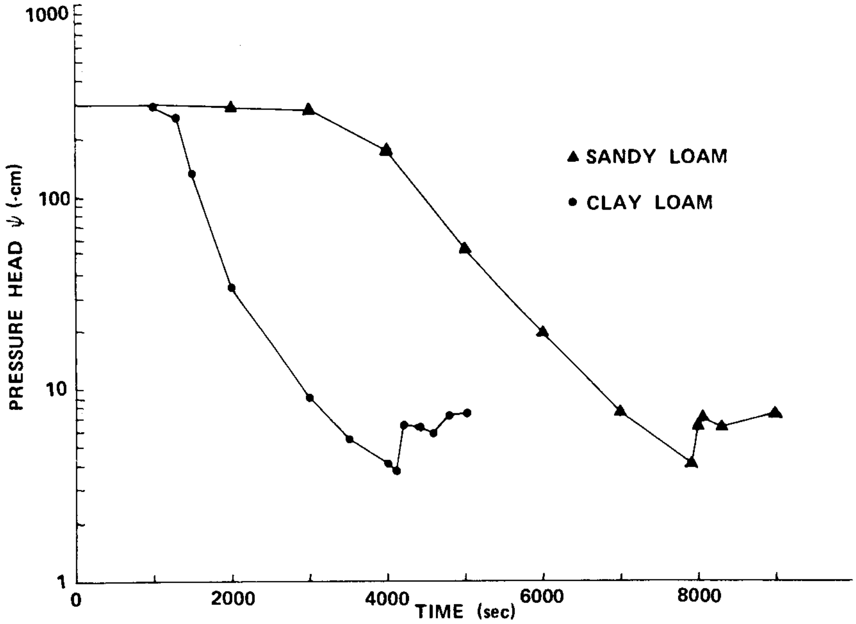

FIGURE 19. Interfacial pressure head plot for Case 1 simulations (constant surface flux) with gravel B as the underlying layer.

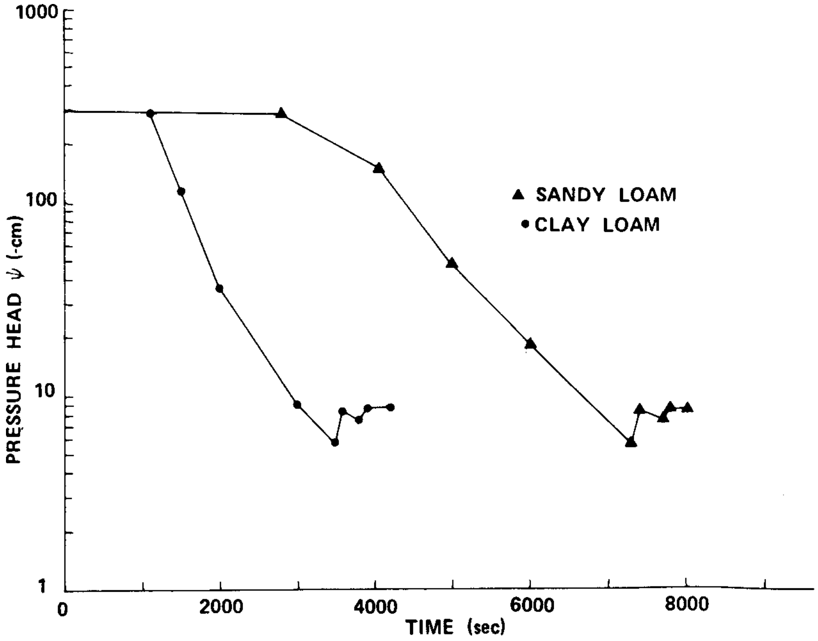

FIGURE 20. Interfacial pressure head plot for Case 1 simulations (constant surface flux) with gravel A as the underlying layer.

The almost instantaneous rise in flux across the interface that occurs once Ψ_c is reached is shown in figures 21 and 22. Because of the previously noted decrease in interfacial pressure potential after moisture breakthrough occurs, a rapid decrease in flux follows this peak. Further fluctuations were found to be primarily related to changes in pressure potential at the node beneath the interfacial node. These fluctuations were also found in simulations for the other two cases. It is difficult to discern whether they are a real phenomenon or are simply due to oscillations in the solution.

Six simulations were run for Case 2 (constant flux followed by redistribution) and are listed in table 8. As is indicated in the table, the moisture front did not cross the interface in two of the simulations. In these simulations the relatively small amount of moisture that entered the column limited the amount of moisture and pressure build-up that could take place in the overlying layer. The interfacial pressure value necessary to allow movement into the gravel was never achieved. Within the overlying layer a static pressure profile eventually developed and all moisture movement ceased.

The amount of moisture entry in the other simulations was enough to allow moisture breakthrough. Figures 23 and 24 show the interfacial pressure profiles for these simulations. The interfacial flux rates are shown in figures 25 and 26. The behavior of the moisture front in these simulations was similar to behavior observed in the simulations of Case 1. Important differences however were found. Flux rates were about one order of magnitude less than in the Case 1 simulations, and for a given layering sequence the amount of time that passed before moisture breakthrough was achieved was longer. Probably most significant was that the range of Ψ_c values (-5.5 cm to -6.5 cm with corresponding Θ values ranging from 97.7% to 98.7% of total saturation) was noticeably lower. This is clearly shown in figures 27 through 30, which compare the pressure head profiles at moisture breakthrough ($\Psi_{interface} = \Psi_c$) for the two cases. The lower Ψ_c values were related to the lower overall rate of moisture infiltration in the Case 2 simulations.

Table 8. Case 2 simulations of rainfall for limited time

Sequence of soils	Period of rainfall (seconds)	Moisture movement into gravel?
Sandy loam over Gravel B	6000	Yes
Clay loam over Gravel B	3000	Yes
Sandy loam over Gravel A	5000	No
Clay loam over Gravel A	2000	No
Sandy loam over Gravel A	6000	Yes
Clay loam over Gravel A	3000	Yes

The overall rate of infiltration in the Case 3 simulations was substantially greater than in the other cases. Four simulations were attempted. In two of the simulations (both had gravel B as the underlying layer) positive pressures developed in the overlying layer and problems occurred with continuity of flux at the interface. The interfacial head profile for the other two simulations is shown in figure 31. The critical pressure values for a

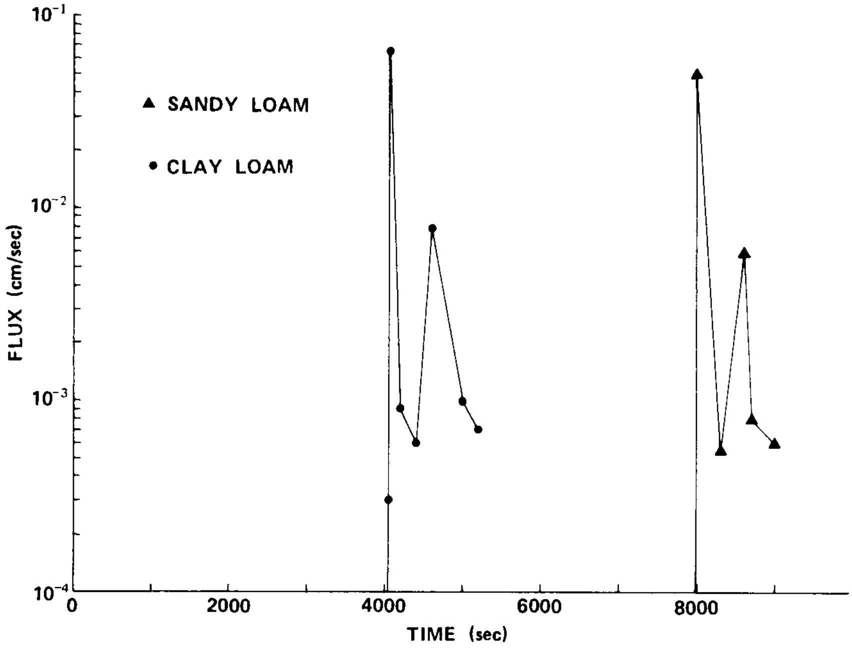

FIGURE 21. Interfacial flux plot for Case 1 simulations (constant surface flux) with gravel B as the underlying layer.

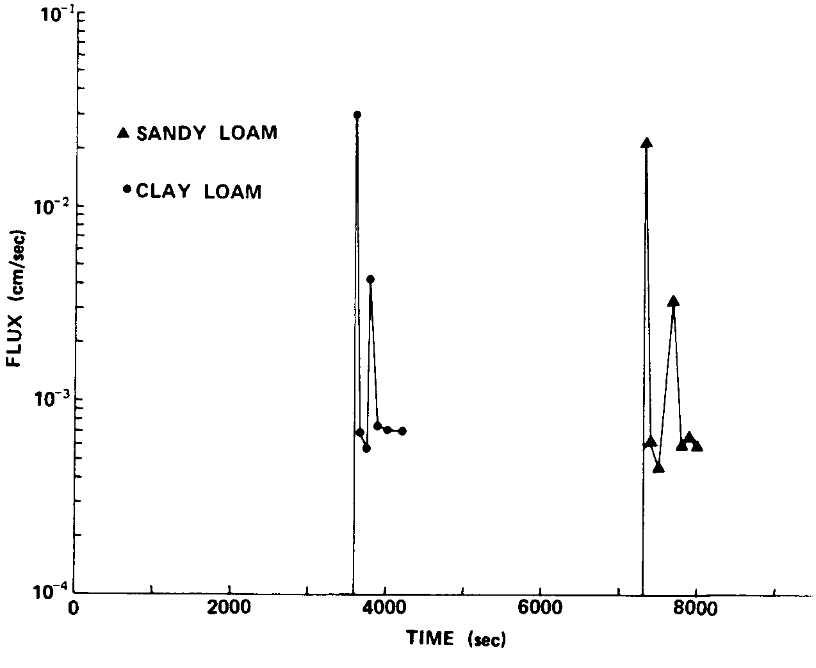

FIGURE 22. Interfacial flux plot for Case 1 simulations (constant surface flux) with gravel A as the underlying layer.

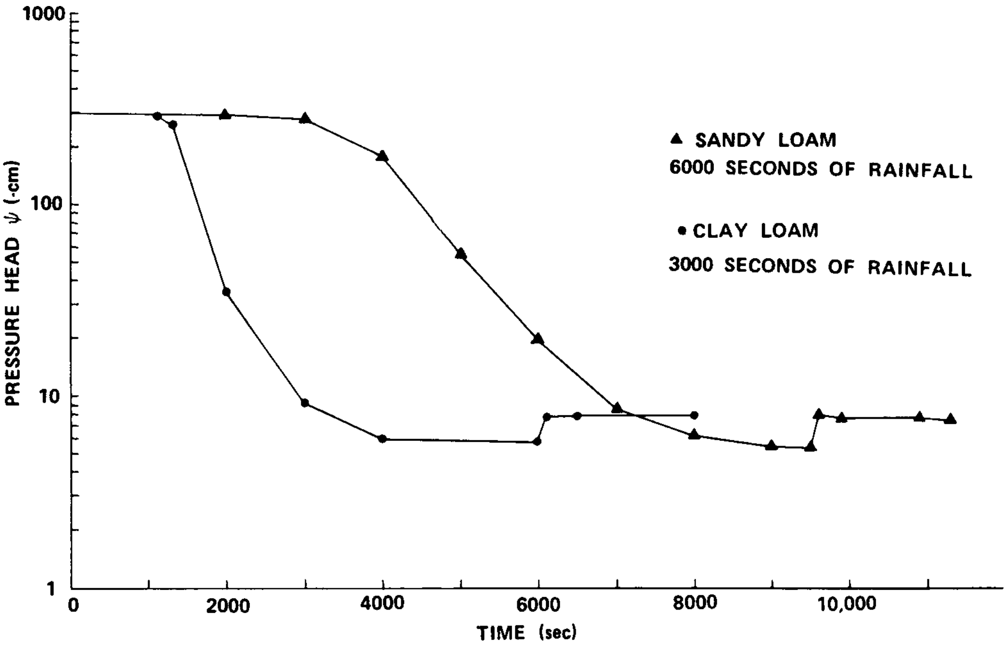

FIGURE 23. Interfacial pressure head plot for Case 2 simulations (constant flux followed by redistribution) with gravel B as the underlying layer.

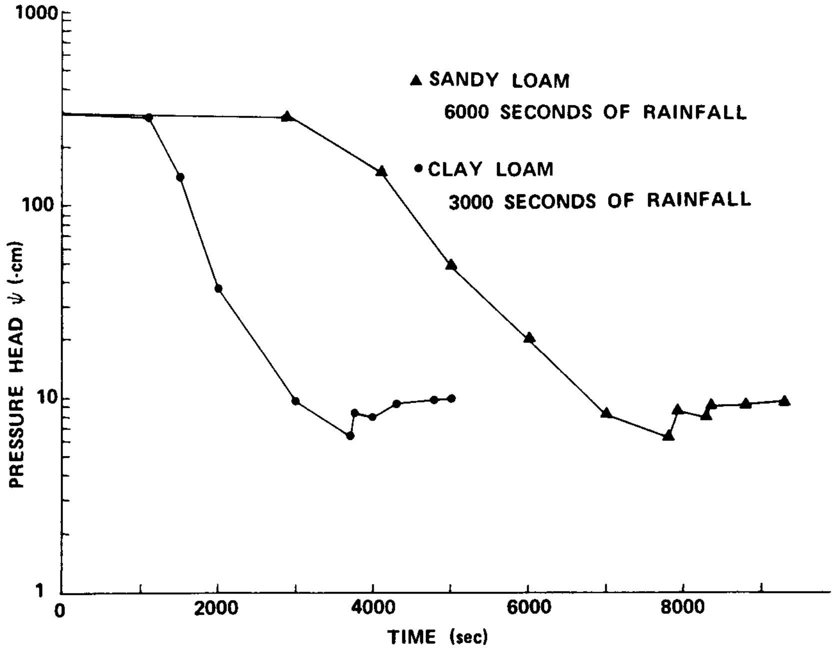

FIGURE 24. Interfacial pressure head plot for Case 2 simulations (constant flux followed by redistribution) with gravel A as the underlying layer.

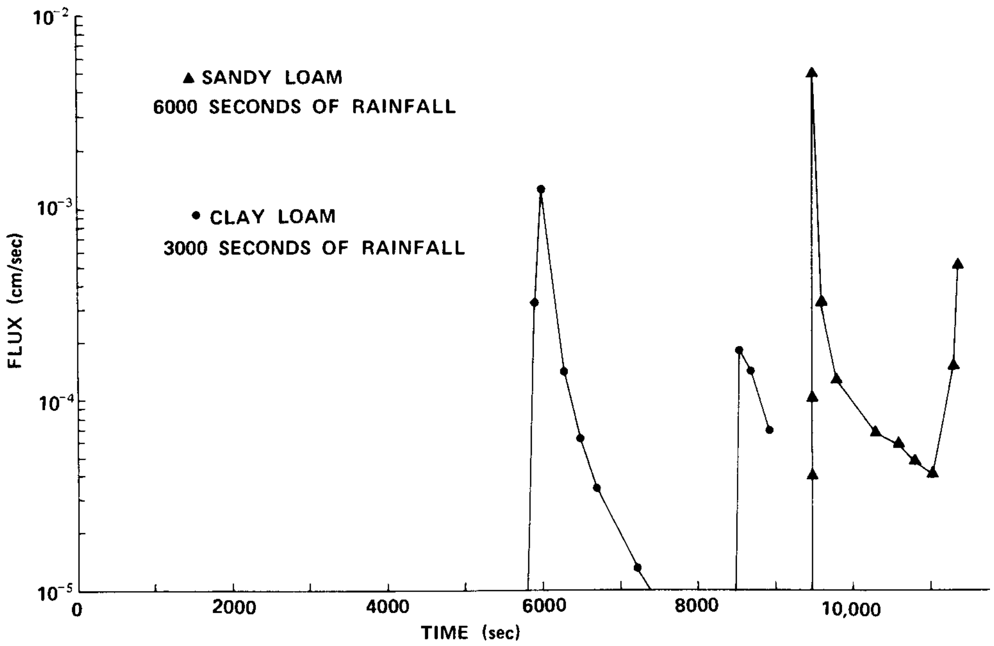

FIGURE 25. Interfacial flux plot for Case 2 simulations (constant flux followed by redistribution) with gravel B as the underlying layer.

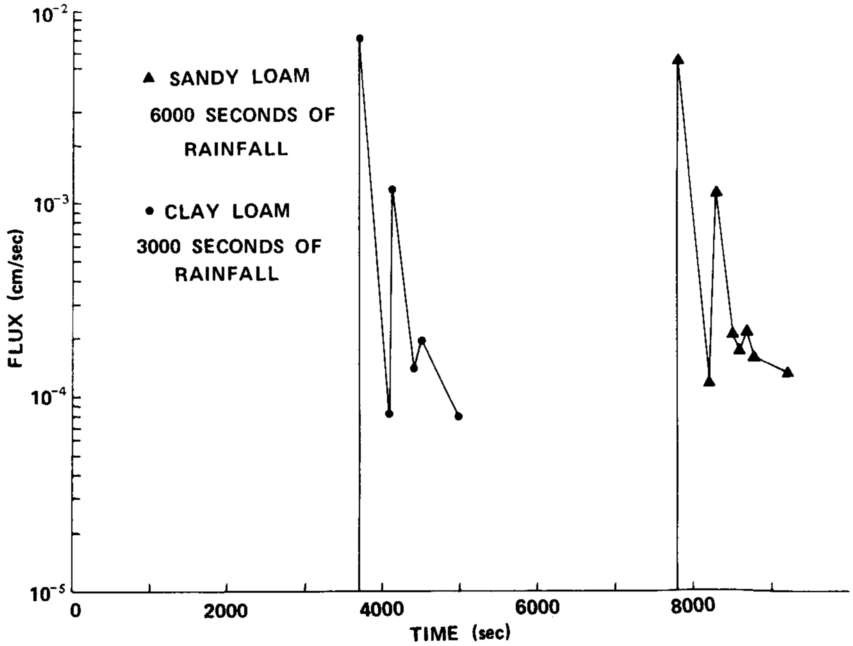

FIGURE 26. Interfacial flux plot for Case 2 simulations (constant flux followed by redistribution) with gravel A as the underlying layer.

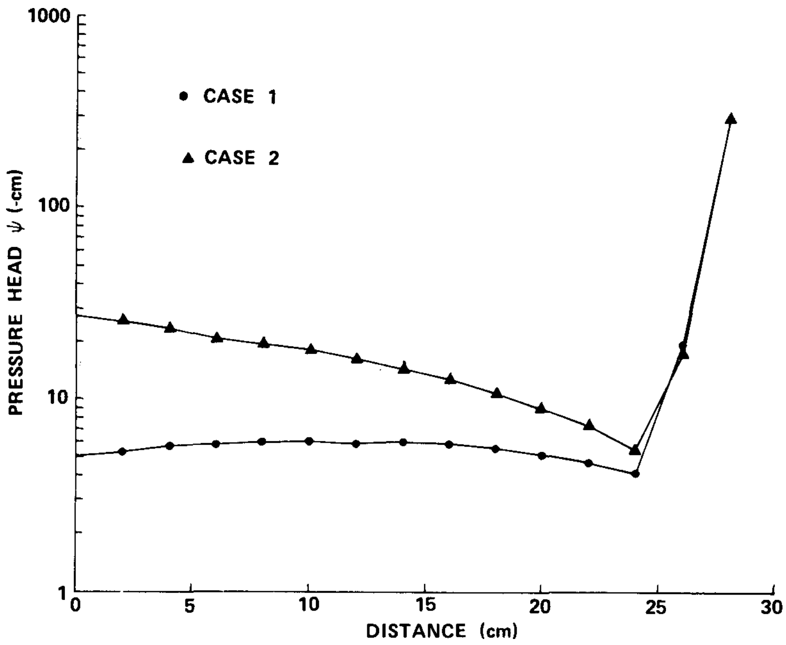

FIGURE 27. Pressure head profile at moisture breakthrough for sandy loam over gravel B. Case 1 represents constant surface flux. Case 2 represents constant flux followed by redistribution.

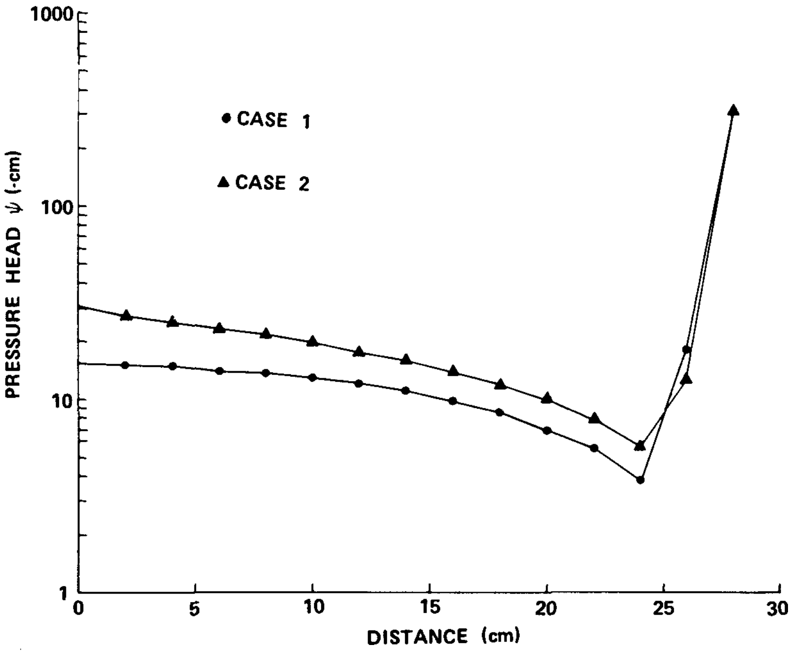

FIGURE 28. Pressure head profile at moisture breakthrough for clay loam over gravel B. Case 1 represents constant surface flux. Case 2 represents constant flux followed by redistribution.

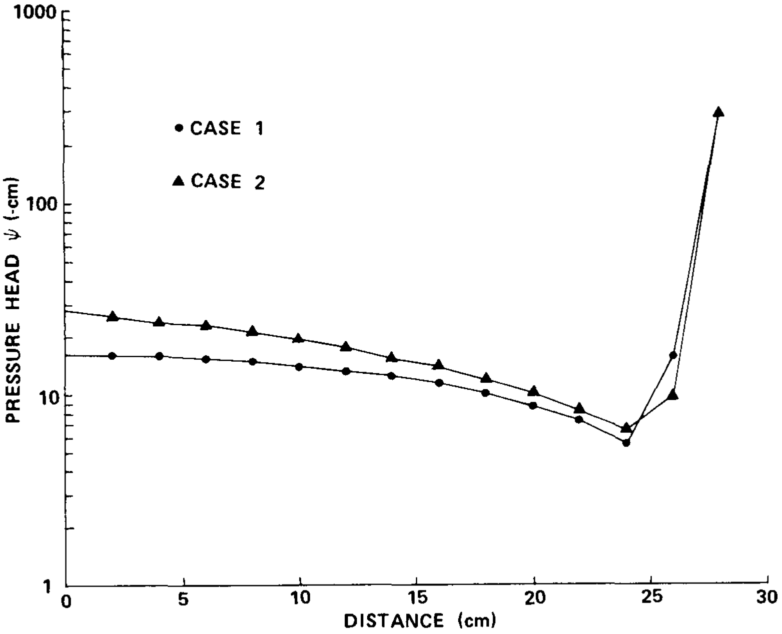

FIGURE 29. Pressure head profile at moisture breakthrough for sandy loam over gravel A. Case 1 represents constant surface flux. Case 2 represents constant flux with redistribution.

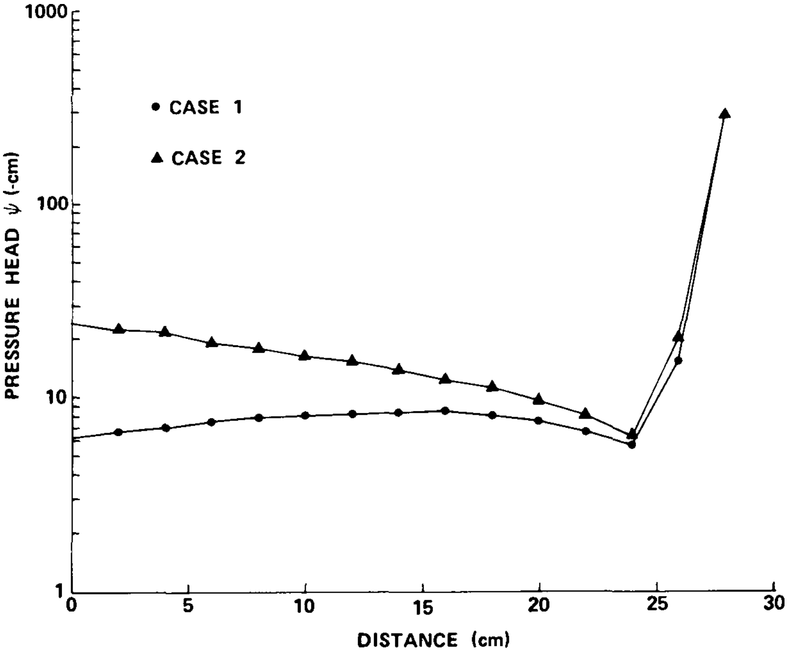

FIGURE 30. Pressure head profile at moisture breakthrough for clay loam over gravel A. Case 1 represents constant surface flux. Case 2 represents constant flux by redistribution.

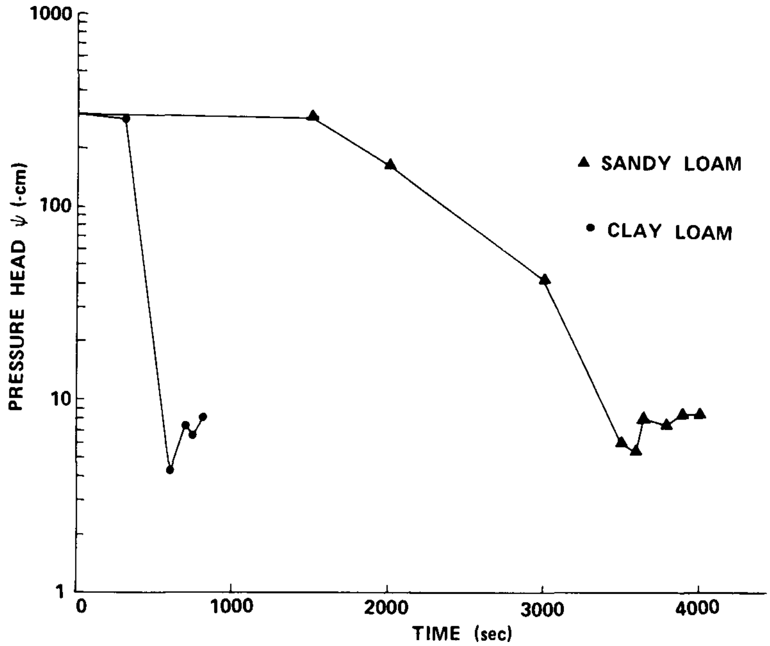

FIGURE 31. Interfacial pressure head plot for Case 3 simulations (constant surface ponding) with gravel A as the underlying layer.

given layering sequence were significantly higher than those for the other cases (-4.5 cm and -5.5 cm with corresponding Θ values 99.3% and 98.8% of total saturation). Values for interfacial fluxes were up to one order of magnitude higher than those in other case simulations (see figure 32).

Subsequent one-dimensional simulations

At the outset of this study we observed that soils compacted wet of optimum moisture content exhibited much different saturated hydraulic conductivities and soil-moisture retention characteristics than did soils compacted dry of optimum. Moisture content-retention curves for the compacted loess, sand and gravel used in these simulations are shown in figures 33 and 34. Simulations were carried out using the physical characteristics associated with soils compacted wet and dry of optimum to see what the influence is on infiltration and percolation.

Simulations were limited chiefly to one- and two-layer systems. This limitation is not serious, because the behavior of the top two layers had to be studied first anyway. Subjects that have been investigated by one-dimensional simulation include: surface boundary conditions, moisture entry into the top layer; moisture redistribution in the top layer and the influence of the second layer on moisture breakthrough from the first. Individual discussions of these are presented below.

Influence of surface boundary conditions. The computer program allows two choices for the surface boundary conditions: (1) a constant head at the surface (first node is saturated--water enters according to the hydraulic conductivity); or (2) a constant flux of water (change in mass per unit time). Figure 35 illustrates the influence of surface flux on moisture entry. Low values of surface flux inhibit moisture movement into the soil. High values of surface flux and constant head (of zero) produce maximum moisture entry.

The infiltration rate produced when the constant surface flux boundary condition is chosen is constant and equal to the flux rate. This is not realistic because the infiltration rate during an actual storm would initially be very high, decreasing asymptotically to a lower value as the surface soil becomes saturated. Figure 36, the infiltration rate for a constant head case, exhibits such behavior.

After obtaining these results, we decided to use a boundary condition of a constant surface pressure head equal to zero. The infiltration rate data showed that this condition was more realistic. Moisture entry is also high for this boundary condition, which means that the boundary condition will not inhibit moisture entry as it would if a low flux rate were selected. Similarly, moisture entry will depend on the hydraulic characteristics of the surface layer, which will allow a rational study of the layers.

Moisture entry into surface layer. Figures 37 and 38 summarize the results of simulations performed to identify the factors influencing moisture entry (infiltration) into the surface layer.

Higher values of initial capillary pressure (or tension) increase moisture entry (fig. 37). Although the soil has a lower degree of saturation

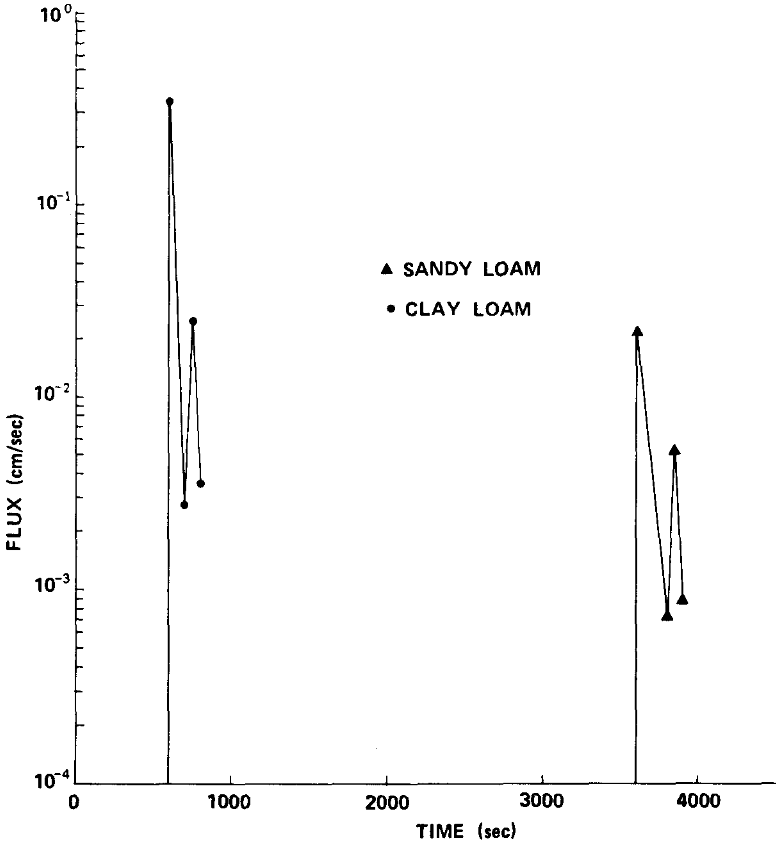

FIGURE 32. Interfacial flux plot for Case 3 simulations (constant surface ponding) with gravel A as the underlying layer.

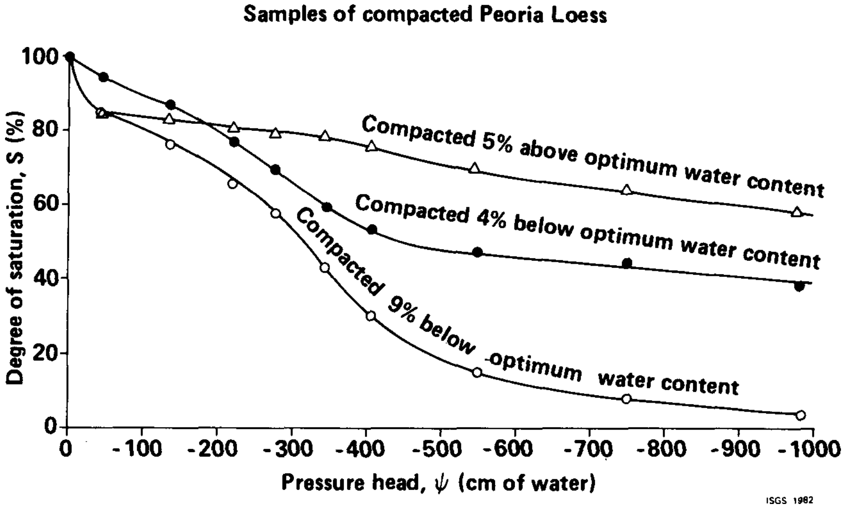

FIGURE 33. Soil-moisture retention curves for samples of compacted Peoria Loess.

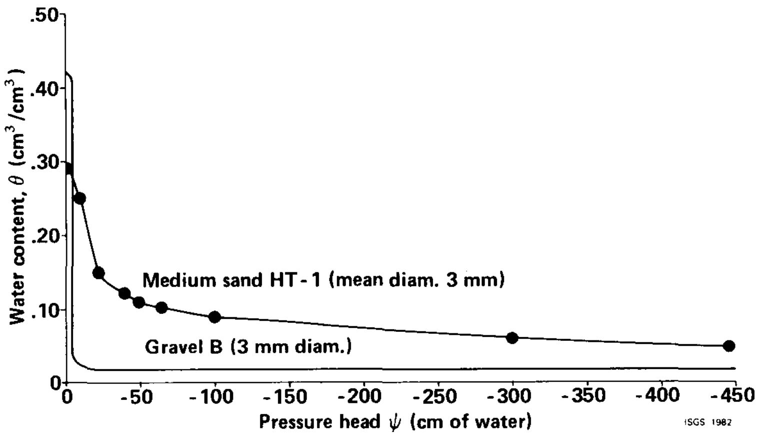

FIGURE 34. Soil-moisture retention curves for coarse-grained materials used in one-dimensional computer simulations.

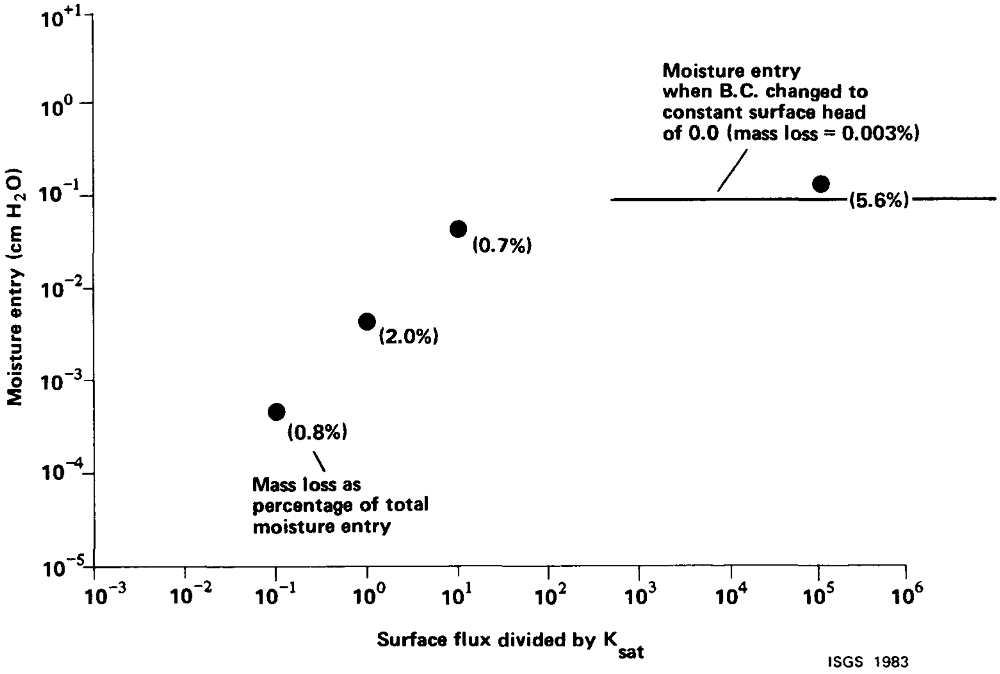

FIGURE 35. Predicted relationship between surface flux and moisture entry for a one-layer system of Peoria Loess compacted wet of optimum. Duration of rainfall is 4 hours. Initial conditions consisted of a constant pressure head of -300 cm.

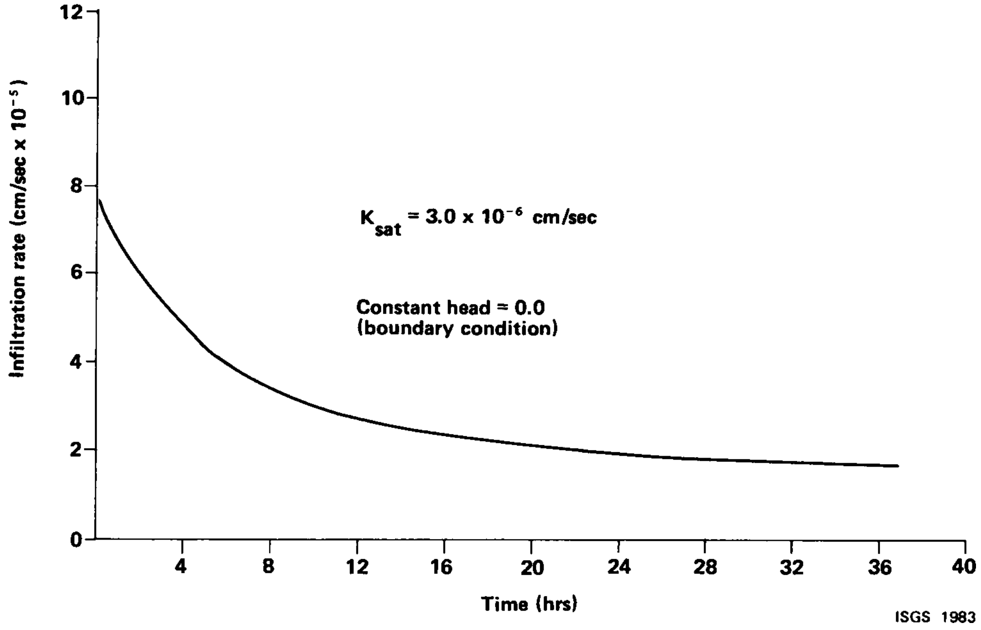

FIGURE 36. Infiltration rate vs. time for Peoria Loess compacted dry of optimum with a constant pressure head at the surface of 0 cm, indicating ponding.

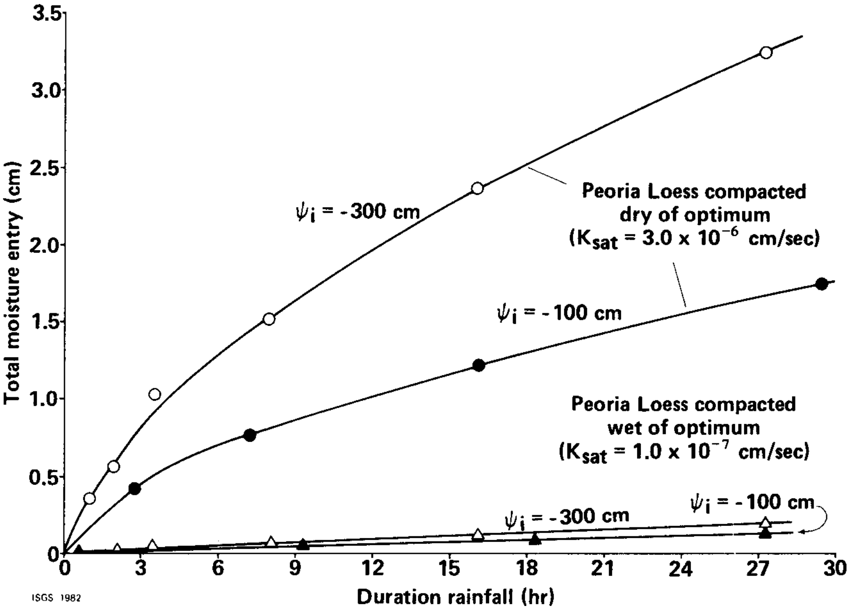

FIGURE 37. Total moisture entry into samples of compacted Peoria Loess under differing initial conditions, showing higher moisture entry (and storage capacity) primarily the result of the greater hydraulic conductivity of samples compacted dry of optimum.

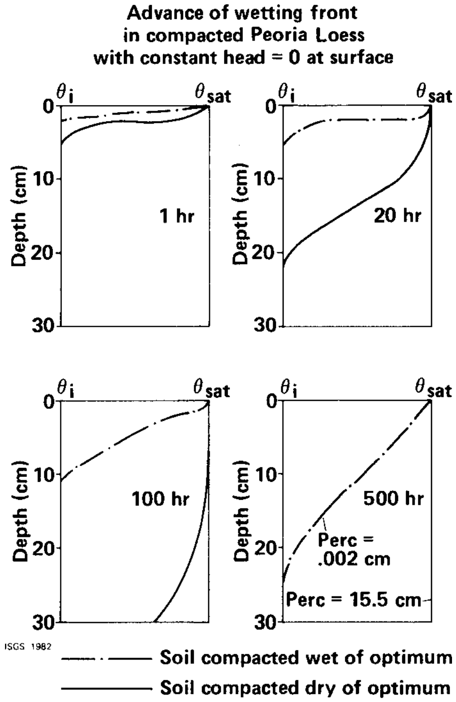

FIGURE 38. Predicted advance of wetting front in compacted Peoria Loess with constant pressure head = 0 at surface, indicating ponding.

(and therefore a lower hydraulic conductivity) when the capillary pressure is higher, the potential infiltration rate is much higher when the degree of saturation is lower. (This last effect apparently overrides the influence of the difference in conductivities, which seems reasonable because the lower the degree of saturation, the more open the pores are in the soil for incoming moisture to occupy.)

Moisture entry is also influenced by the compaction water content when fine-grained soils are used in the surface layer. In soils compacted wet of optimum there is a much lower moisture entry and a much slower rate of moisture front advance (figure 38) than in soils compacted dry of optimum moisture. This effect is partly related to the hydraulic conductivity factor discussed in the previous paragraph; soils compacted wet of optimum exhibit much lower values of saturated hydraulic conductivity than those compacted on the dry side.

Moisture redistribution. Moisture redistribution was investigated in soils compacted wet and dry of optimum moisture.

Moisture redistribution can be investigated with the model by changing the surface boundary condition from a constant head to a constant surface flux equal to zero. The capillary pressures resulting at each node after the desired rainfall duration are input as the initial pressures for the redistribution sequence.

Figure 39 shows the moisture redistribution after a 4-hour rain for a surface soil compacted dry of optimum moisture. After rainfall, the moisture front advanced deeper into the soil compacted dry of optimum (about 11 cm as compared to only 4 cm for the soil compacted wet of optimum). Redistribution in the soil compacted wet of optimum was inhibited because of a large initial mass loss that was actually larger than the total moisture entry. Moisture redistribution in the soil compacted wet of optimum showed progressive advance of the moisture front and eventually some percolation through the 30 cm layer.

Figure 40 shows the moisture front advance for a more complex rainfall sequence--4 hours of rain followed by 50 hours of dry weather, then another 4 hours of rain. For a soil compacted dry of optimum, the moisture front advance is much deeper after the second rain.

Influence of second layer on moisture breakthrough. If the texture of the second layer is much coarser than the fine-grained top layer, moisture will build up in the top layer before entering the second layer. This phenomena has been termed the "wick effect" and occurs primarily due to differences in the soil moisture retention characteristics and hydraulic conductivity of coarse and fine materials (figs. 41 and 42).

The water content in a layer of compacted Peoria Loess overlying a coarse gravel with a saturated hydraulic conductivity of 1 cm/sec builds up significantly prior to breakthrough at 2600 hours of continued surface ponding (fig. 41). For comparison, the moisture content in a single layer of Peoria Loess is also shown. Figure 42 illustrates the more limited moisture retention that occurs in compacted Peoria Loess overlying medium sand that has a hydraulic conductivity much less than that of the gravel (in this case, moisture breakthrough occurs after only 940 hours). The adjacent example of a

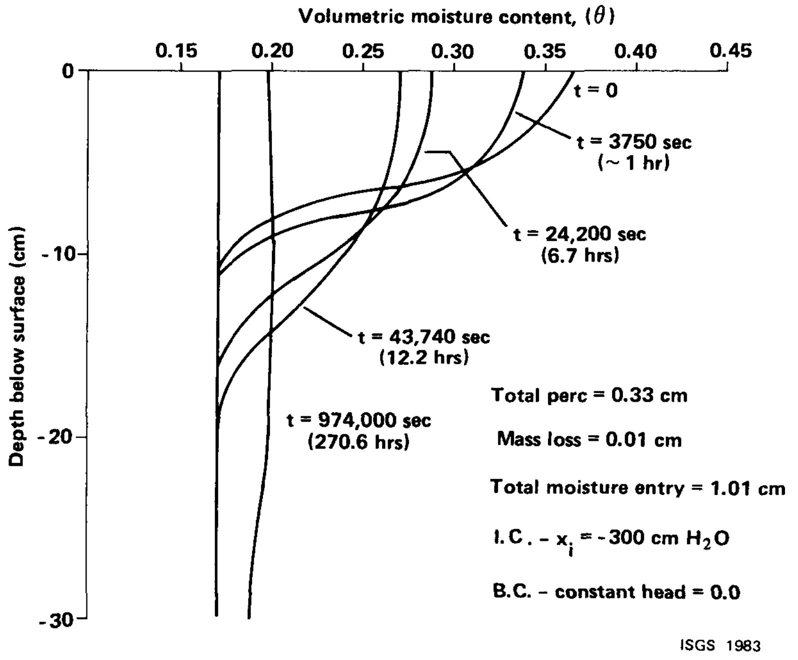

FIGURE 39. Redistribution after 4 hours of simulated rainfall in Peoria Loess (P-6) compacted dry of optimum.

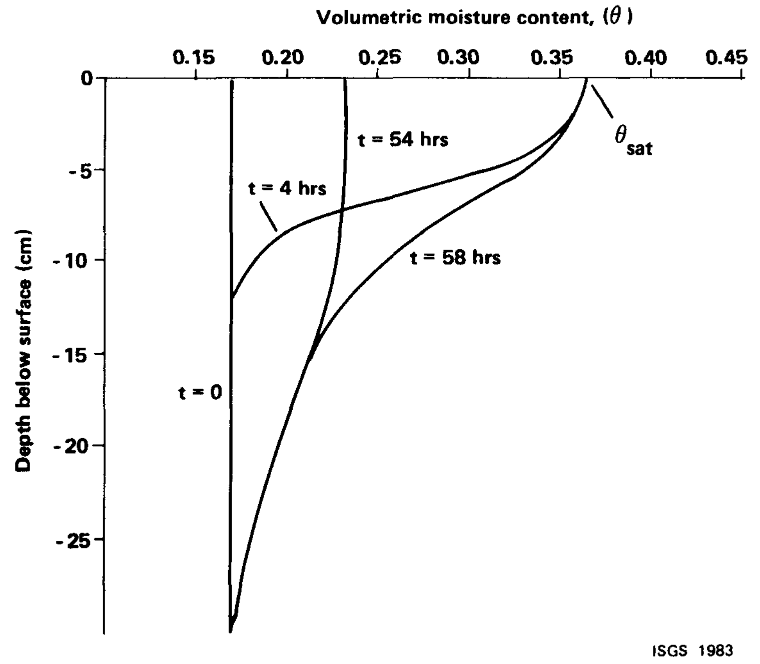

FIGURE 40. Predicted moisture redistribution in a 30 cm layer of Peoria Loess (P-6) compacted dry of optimum. The simulated rainfall sequence consists of 4 hours of rain, followed by 50 hours of redistribution, followed by 4 hours of rain. Initial conditions consist of a constant pressure head of -300 cm.

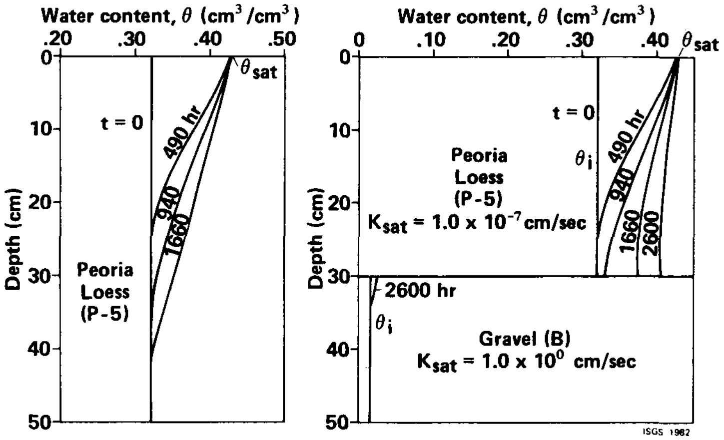

FIGURE 41. Effect of layer of coarse-grained gravel on moisture retention in the overlying fine-grained material compared to moisture movement through a single layer of fine-grained material.

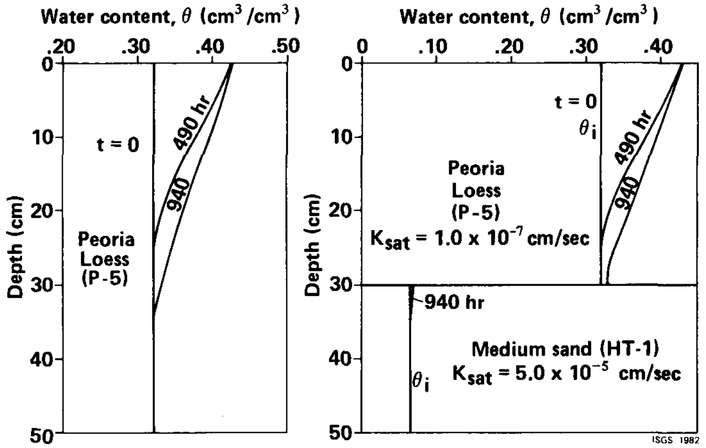

FIGURE 42. Effect of layer of medium sand on moisture retention in the overlying fine-grained material compared to moisture movement through a single layer of fine-grained material.

single layer of loess illustrates an almost negligible difference between the layered and nonlayered case.

Because coarse soils exhibit increasing values of saturated hydraulic conductivity as the degree of coarseness is increased, the relative affects of layering two materials can be expressed in terms of the ratio of the saturated hydraulic conductivities. The conductivity ratio is defined as the saturated hydraulic conductivity value of the second layer divided by the value of the first layer. The effects of differences in the soil moisture retention curves are not directly accounted for by the conductivity ratio. Large conductivity ratios simply suggest major differences in the texture of the layered soils. In this study only coarse-grained soils were used for the second layer and compacted, fine-grained soils for the first.

Figure 43 shows the relationship of conductivity ratio to the storage efficiency of the top layer. If the top layer becomes saturated before moisture breakthrough occurs, then the storage efficiency is 1.0 (or 100%). This is ideally what we would like to have happen.

The efficiency of the "wick effect" is influenced by the initial conditions and the compaction water content of the top layer. Two initial saturation conditions were evaluated (fig. 43). The higher the capillary pressure (the more unsaturated initially), the more effective is the top layer in storing moisture. Erratic behavior was observed when the pressure head was initially -100 cm of water. The intermediate values of conductivity ratio were investigated using a sand as the second layer. At -100 cm of water the sand is capable of changing its moisture content with a small pressure change (fig. 34) in contrast to the gravel--used for higher values of conductivity ratio--which cannot. As a result, moisture moved from the top layer into the second layer prematurely before arrival of the wetting front.

Compaction water content directly affects the capacity of the soil to retain moisture. Soils compacted dry of optimum exhibit much higher effective storage values, primarily because of their soil-moisture retention characteristics. As seen in figure 33, soils compacted wet of optimum possess much less potential storage because they are more highly saturated than soils compacted dry of optimum.

One conclusion that can be drawn from figure 43 is that in the most ideal case to achieve saturation of the top layer prior to moisture breakthrough, a conductivity ratio of at least 300,000 is required for soils compacted dry of optimum and greater than 10 million for soils compacted wet of optimum.

Figures 44 and 45 show the total moisture entry and time to break through data for these simulations.

G. TWO-DIMENSIONAL SIMULATIONS

Introduction

The finite element model, UNSAT2, developed by Neuman (1973) and Neuman et al. (1975), was used to simulate two-dimensional moisture movement through laboratory columns and field-scale cover designs. The model uses a Galerkin-type finite element method to simulate two-dimensional nonsteady flow of water

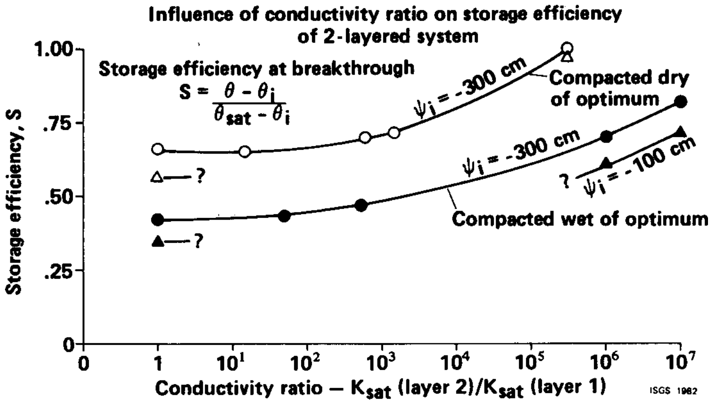

FIGURE 43. Influence of hydraulic conductivity ratio on the storage efficiency of the top layer of a two-layered system.

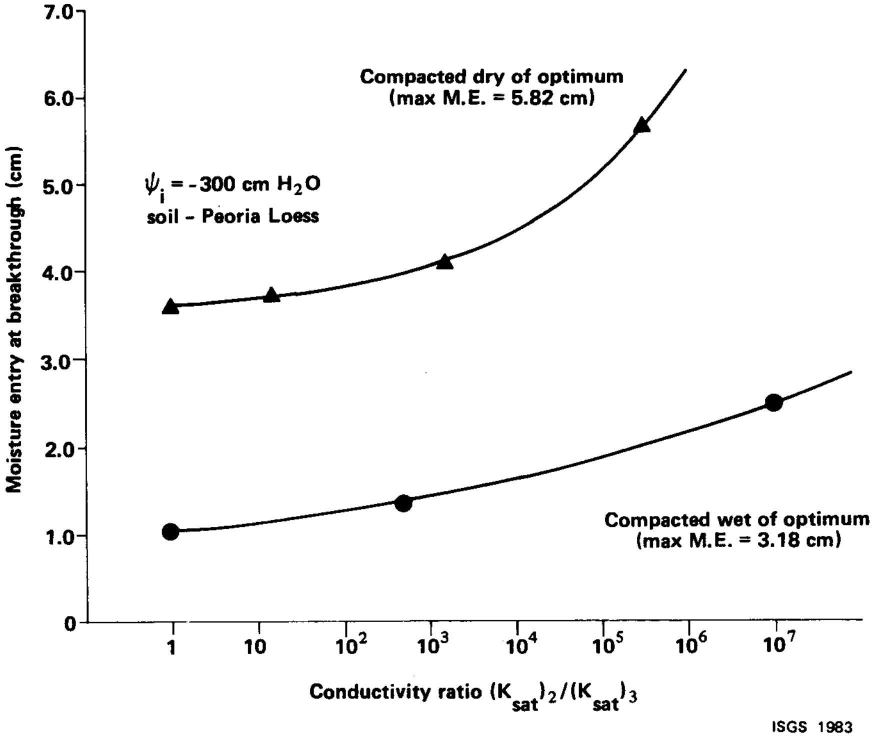

FIGURE 44. Moisture entry at breakthrough into a 30 cm layer of compacted Peoria Loess. Initial conditions consisted of a constant pressure head of -300 cm.

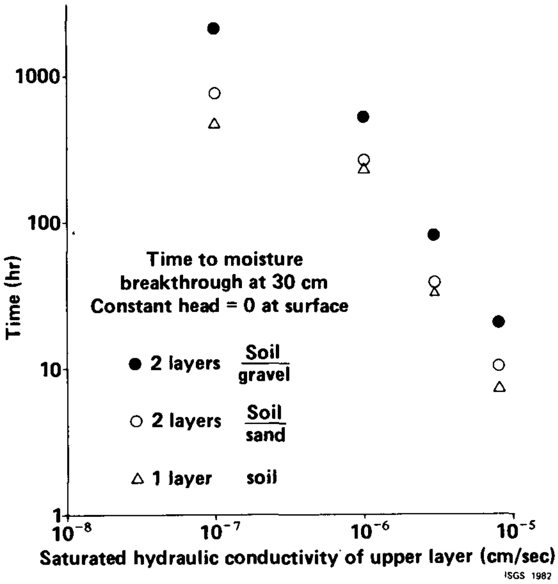

FIGURE 45. Elapsed time prior to moisture breakthrough for a single 30 cm layer of compacted soil and a 30 cm layer of compacted soil underlain by sand and gravel as a function of saturated hydraulic conductivity of the upper layer.

in incompressible, saturated-unsaturated soils; evaporation and water uptake by roots are considered. The theoretical development of the model is presented by Neuman et al. (1975), and the results of verification with field measurements and comparison with the results obtained by a finite difference technique are described in Feddes et al. (1975).

The finite element method has several advantages over finite difference techniques. It can easily handle anisotropic, nonuniform flow regions with irregular boundaries. In UNSAT2, nonlinear atmospheric boundary conditions along evaporation or infiltration surfaces and along seepage faces are based on calculations of flux normal to any boundary. The treatment of boundary conditions is described in detail in Neuman et al. (1975).

Two types of problems were studied initially. The first involved the simulation of moisture movement through a system designed to the scale of the laboratory gamma column described in Section I-E. The primary purpose of these simulations was to attempt to calibrate and verify the model for the particular soils and boundary conditions used in this study. The second type of problem involved the simulation of infiltration and two-dimensional moisture movement through a sloping, field-scale layered cover design.

Influence of boundary conditions

UNSAT2 incorporates several possible types of boundary conditions--including evaporation and infiltration boundaries and water uptake by roots--in addition to those of constant total head (h), constant pressure head (Ψ) or constant flux (Q).

Along soil-air interfaces (in the absence of ponding) the soil can lose water to the atmosphere by evaporation or gain water by infiltration. While the maximum possible rate of evaporation depends only on atmospheric conditions, the actual flux across the soil surface is limited by the ability of the soil to transmit water from below. Similarly, if the intensity of rainfall exceeds the infiltration capacity of the soil, surface runoff will occur and the actual flux depends on antecedent moisture conditions in the soil.

A seepage face is an atmospheric boundary at which water seeps out from the saturated part of an exposed face. Pressure head along the seepage face must be zero (atmospheric pressure). The extent of the seepage face varies with time.

In the simulations described here, boundary conditions at the surface included continuous rainfall (constant surface flux, Q) and continuous ponding (constant pressure head, $\Psi = 0$). At the bottom, boundary conditions consisted of either a constant pressure head, $\Psi = 0$ (water table), a prescribed constant negative pressure (tension), or a seepage face. The sides of both the column and field scale simulations are no-flow boundaries.

A seepage face conceivably might represent conditions at the bottom of a landfill cover if the waste remains unsaturated and if drains or sumps maintain atmospheric pressure. In the simulations with a seepage face at the bottom, the unsaturated part of the boundary is a prescribed flux boundary ($Q = 0$); when saturated, it is treated as a prescribed pressure head boundary with $\Psi = 0$.

As in the one-dimensional simulations, the infiltration rate resulting from a constant surface-flux boundary condition is substantially lower than that for continuous surface ponding with a constant pressure head, $\Psi = 0$. The latter appears to best represent conditions during an actual storm when the infiltration rate typically decreases asymptotically to approximately the saturated hydraulic conductivity of the upper layer as the surface soil becomes saturated.

Laboratory column-scale simulations

A soil column 29 cm long and 8 cm wide was chosen to simulate laboratory gamma column experiments. In most simulations, the column consisted of 11 cm of Peoria Loess overlain by 9 cm of a medium sand and 9 cm more of Peoria Loess. The model consisted of 116 rectangular elements with dimensions of 1 cm by 2 cm. The configuration of the finite element network is shown in figure 46.

For all simulations, the sides of the column were considered no-flow boundaries and all but the top and bottom nodes had initial pressure heads of -100 cm. The relationship between moisture content, Θ, and pressure head, Ψ, was obtained from laboratory tests. Moisture-retention curves for each of the materials in these simulations are presented in figure 47. Hydraulic conductivity as a function of water content and pressure head was calculated using the method of Green and Corey (1971) described previously. Figure 48 includes curves of hydraulic conductivity vs pressure head for each material. Only boundary conditions at the top and bottom of the column were changed between simulations to allow better comparison of results. It was not possible to calibrate the model with the results of these gamma column experiments because the soil-moisture characteristics of the sand actually used in the column had not been determined prior to the simulations and because reliable data from the column run were not yet available.

Case 1. The first case involved a three-layer column under conditions with constant ponding at the surface and a constant pressure head of -100 cm at the bottom of the column. Figures 49 and 50 show pressure head and water content distributions at various times. Initially, the pressure head decreases in the loess below the sand. The maximum tension was reached in the lower loess at about 14 hours. During the first 14 hours the tension increased significantly at the interface of the sand and underlying loess. As time progressed, the pressure head throughout the sand became equal to the pressure head at the base of the upper loess. However, the moisture content of the sand was significantly lower than the moisture content of either loess layer for the entire simulation period of nearly 10 days. Figure 51 shows the change in pressure head at various depths in the column with time. The pressure head increased substantially in the upper loess and at the upper interface after about 10,000 seconds while tensions in the lower portion of the column remained high for nearly 100,000 seconds. As noted in figure 41, pressure heads at the two interfaces became nearly equal after about 10 days.

Case 2. The second case involved a single thick layer of loess; boundary conditions remained the same. Figures 52 and 53 show pressure head and water content profiles at several times. No abrupt changes occur in pressure head or water content with depth. Initially, the pressure head profiles are similar to those of the three-layer case, but in the upper portion of the

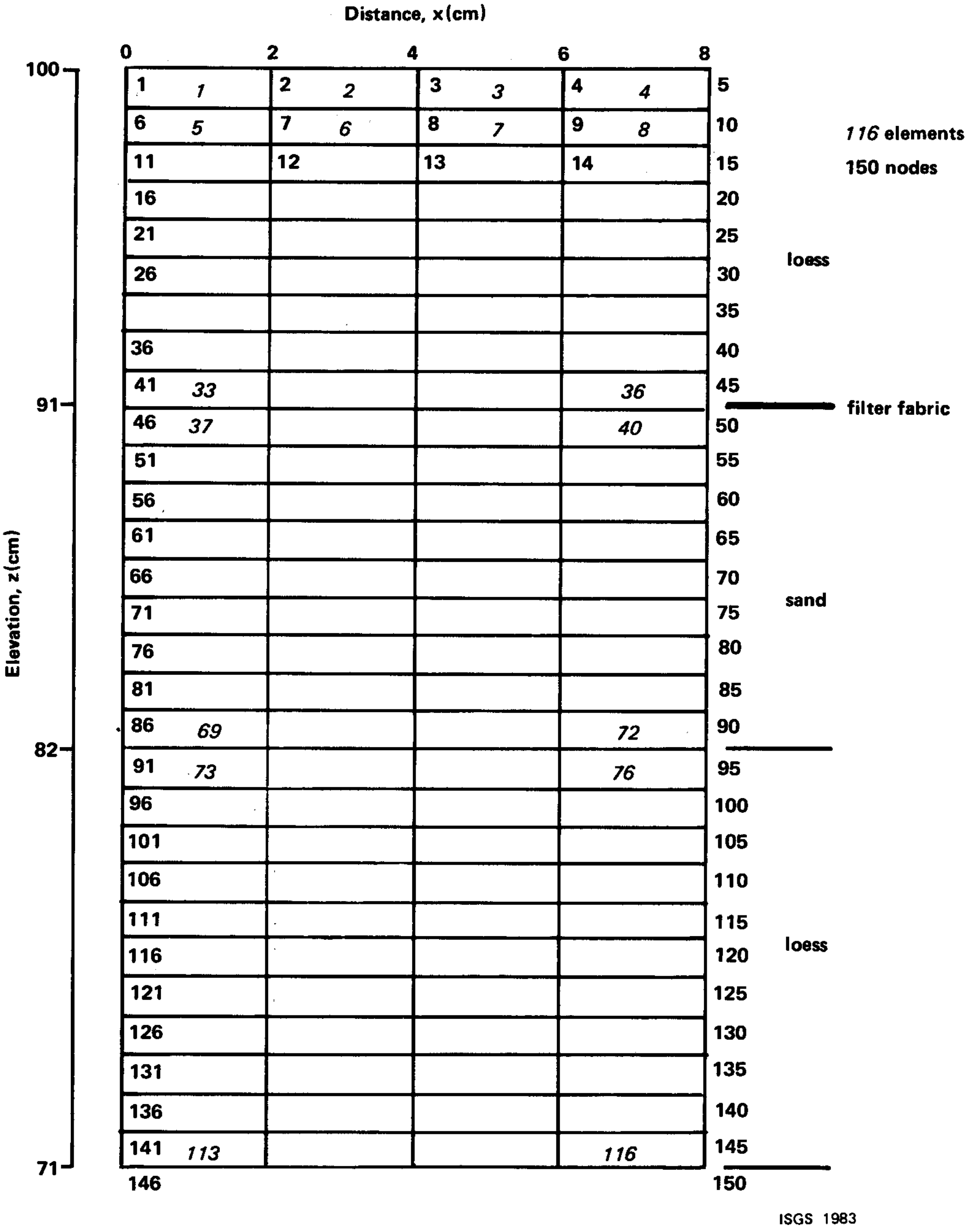

FIGURE 46. Cross section of simulated gamma column with superimposed finite element network.

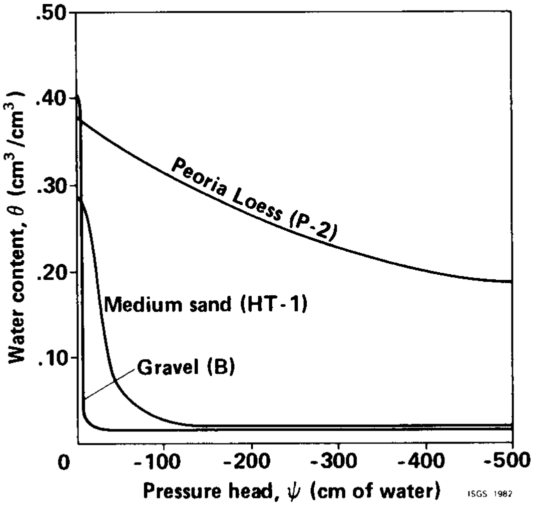

FIGURE 47. Soil water content as a function of pressure head for soils used in two-dimensional simulations.

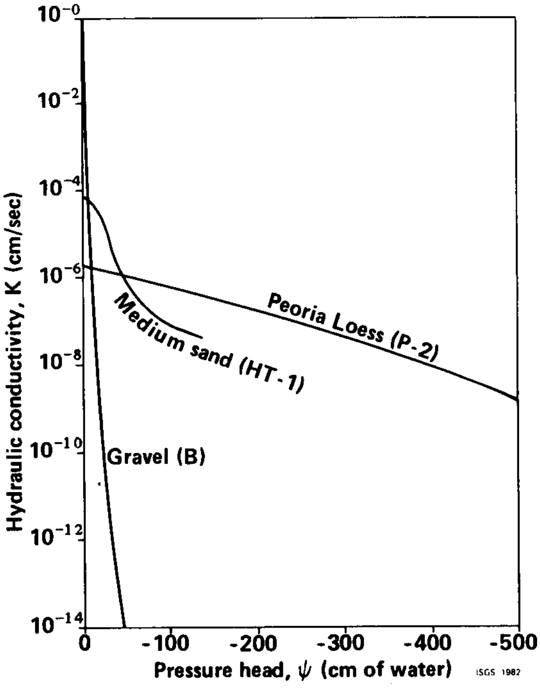

FIGURE 48. Hydraulic conductivity as a function of pressure head for soils used in the simulations. Calculations of hydraulic conductivity based on method of Green and Corey (1971).

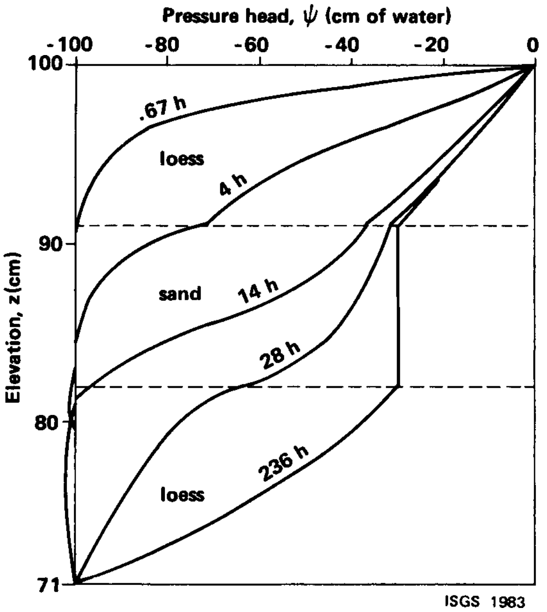

FIGURE 49. Predicted distribution of pressure head at a selected times for Case 1 simulations consisting of a three-layer cover under conditions of constant ponding at the surface and constant pressure head = -100 cm of water at the bottom.

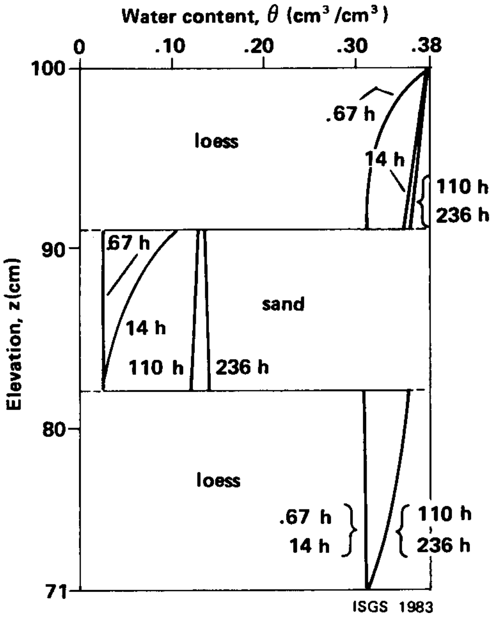

FIGURE 50. Predicted distribution of water content at selected times for Case 1 simulations consisting of a three-layer column under conditions of constant ponding at the surface and constant pressure head = -100 cm of water at the bottom.

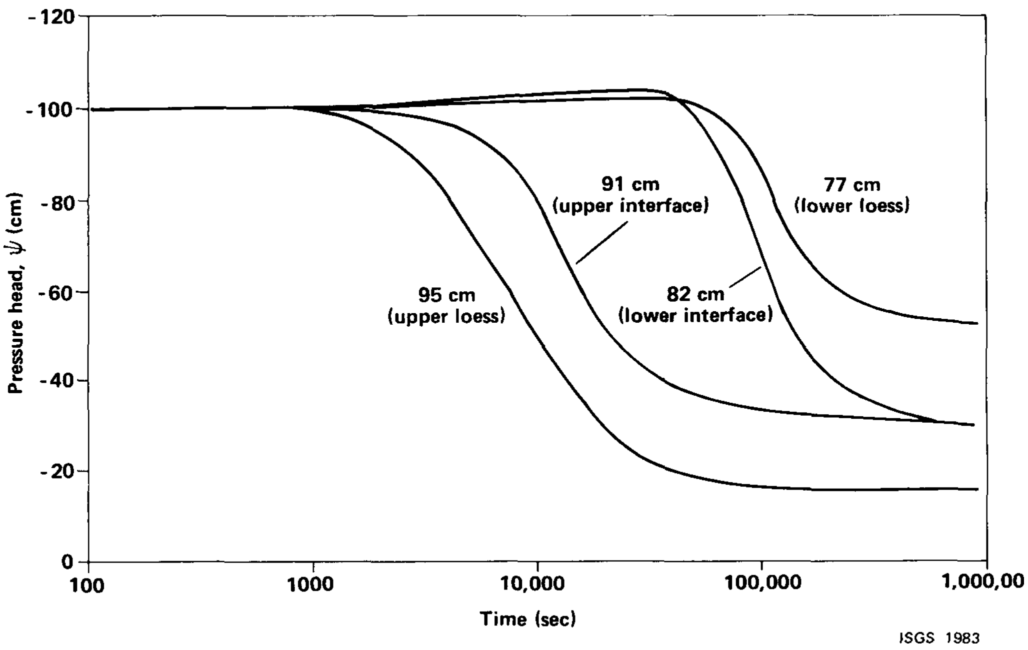

FIGURE 51. Predicted change in pressure head with time for various depths for Case 1 simulations, a three-layer column under conditions of constant ponding at the surface and constant pressure head = -100 cm of water at the bottom.

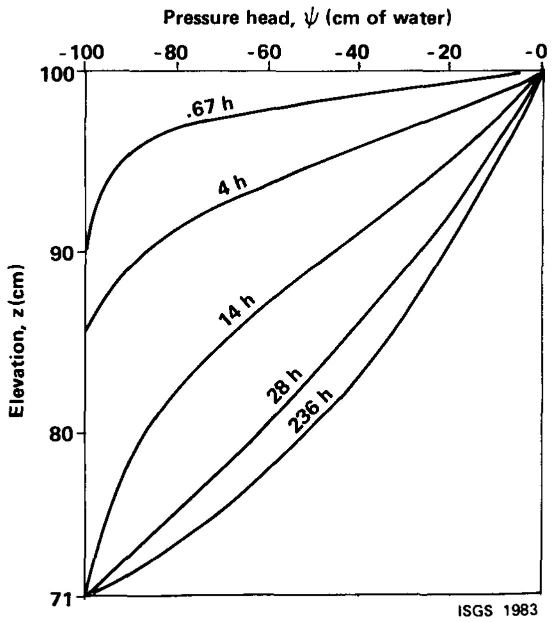

FIGURE 52. Predicted distribution of pressure head at selected times for Case 2 simulations, a one-layer column of Peoria Loess under conditions of constant ponding at the surface and constant pressure head = -100 cm of water at the bottom.

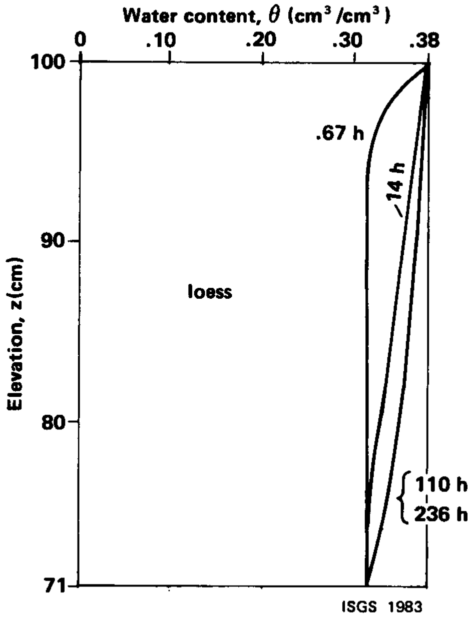

FIGURE 53. Predicted distribution of water content at selected times for Case 2 simulations, one-layer cover of Peoria Loess under conditions of constant surface ponding and constant pressure head = -100 cm of water at the bottom.

single layer column the tension decreases (increasing pressure head) more rapidly with time than in the three-layer column. The moisture content curves are also similar; however, in the single layer column the sharp drop in water content associated with the sand layer does not occur. Figure 54 shows pressure head as a function of time for various depths with the one-layer column; steady-state tension in the upper portion of the one-layer column is lower than in the three-layer column (fig. 51). However, the increase in pressure head in the lower loess in the one-layer case occurs sooner than it does in the three-layer case.

Case 3. Case 3 was identical to case 1, except that the lower boundary was assumed to have constant pressure head of zero to simulate saturated conditions in the waste below the cover. Figures 55 and 56 show the pressure head and water content profiles for various times. Profiles in the upper loess are similar for cases 1 and 3 for the first 110 hours. Over longer periods, saturation was achieved more rapidly in case 3, in which a water table was simulated at the bottom. When the base of the cover was saturated, pressure heads approached zero and water contents approached saturation much faster than they did in case 1. By the end of the simulation, the lower loess and bottom half of the sand were saturated, showing that the column became saturated from the bottom up. Figure 57 shows the change in pressure head with time. Conditions in the upper loess and at the upper interface are nearly identical to those in case 1 for approximately the first 40,000 seconds. Pressure heads increased significantly throughout the column between 10,000 and 20,000 seconds.

Case 4. In the fourth case the bottom of the column was modeled as a seepage face. We believe that this case may best represent actual conditions. The results of this simulation are shown on figures 58-60. The response of this system varied between that observed for cases 1 and 3. For approximately the first 28 hours, the results of this simulation and those for case 1 are very similar in the upper loess and sand, and the pressure heads in the lower loess are greater in case 4 with a seepage face. By the end of the simulation--when the bottom is saturated--the profile is virtually identical to that of the water table case (case 3). The observations also generally hold true for the water content profiles. The graph of change in pressure head with time (fig. 60) is similar to the graph for case 1 for all but the lower loess during the first 100,000 seconds. Final equilibrium pressures are similar to those in case 3.

Case 5. In the final case, the bottom boundary was the same as in case 1 but a constant surface flux equal to the saturated hydraulic conductivity of the loess (2×10^{-4} cm/sec) was assumed. The results are shown in figures 61-63. Both pressure head and water content remained approximately constant through the upper loess as the simulation progressed. The lower loess and interface experienced a decrease in pressure head for about the first 200,000 seconds. Subsequently, pressure head increased throughout the column. Water content and pressure head throughout the column were less than that observed in the case of a constant pressure head of zero at the surface. Little change was noted in the moisture content of the sand and lower loess. Pressure heads did not change rapidly at any point in the column until after 200,000 seconds.

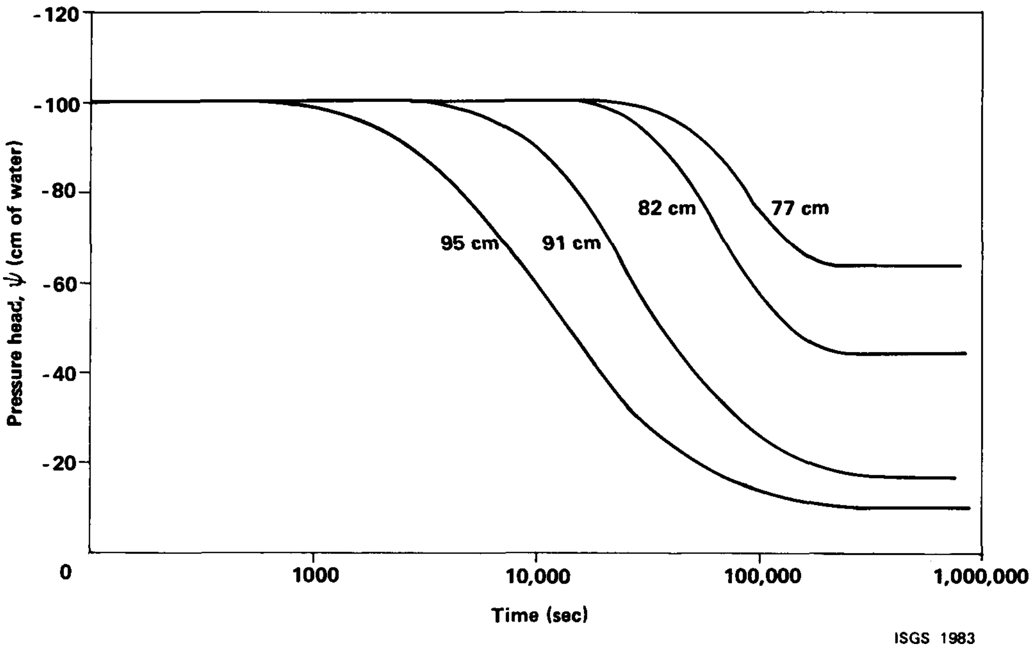

FIGURE 54. Predicted change in pressure head with time at various depths for Case 2 simulations, a one-layer column of Peoria Loess under conditions of constant ponding at the surface and constant pressure head = -100 cm of water at the bottom.

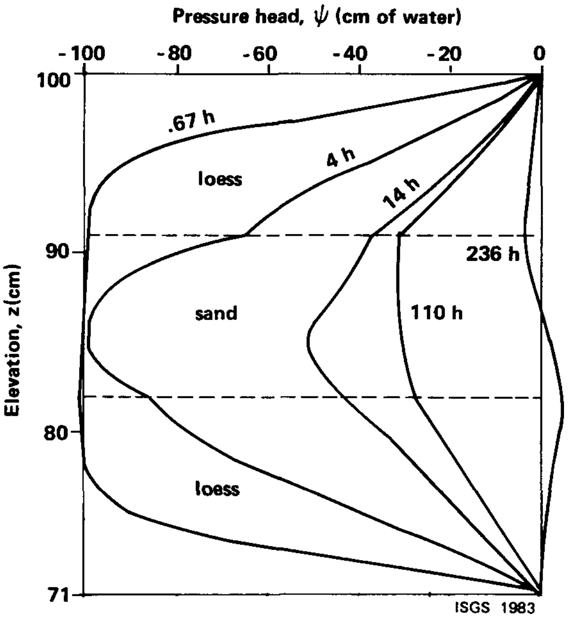

FIGURE 55. Predicted distribution of pressure head at selected times for Case 3 simulations, a three-layer column under conditions of constant pressure head = 0 (water table) at the bottom.

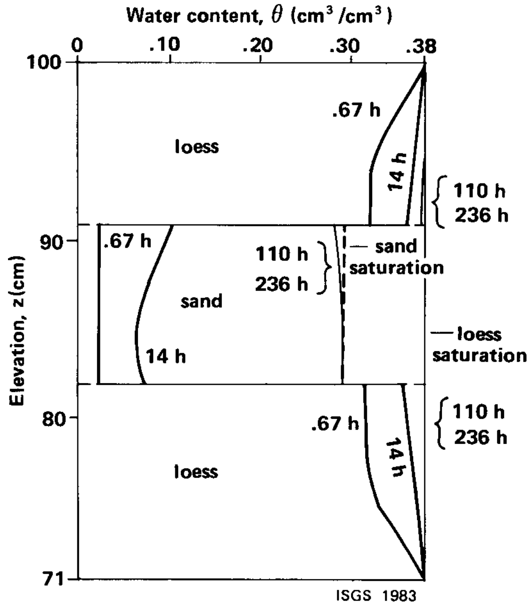

FIGURE 56. Predicted distribution of water content at selected times for Case 3 simulations, a three-layer column under conditions of constant ponding at the surface and constant pressure head = 0 (water table) at the bottom.

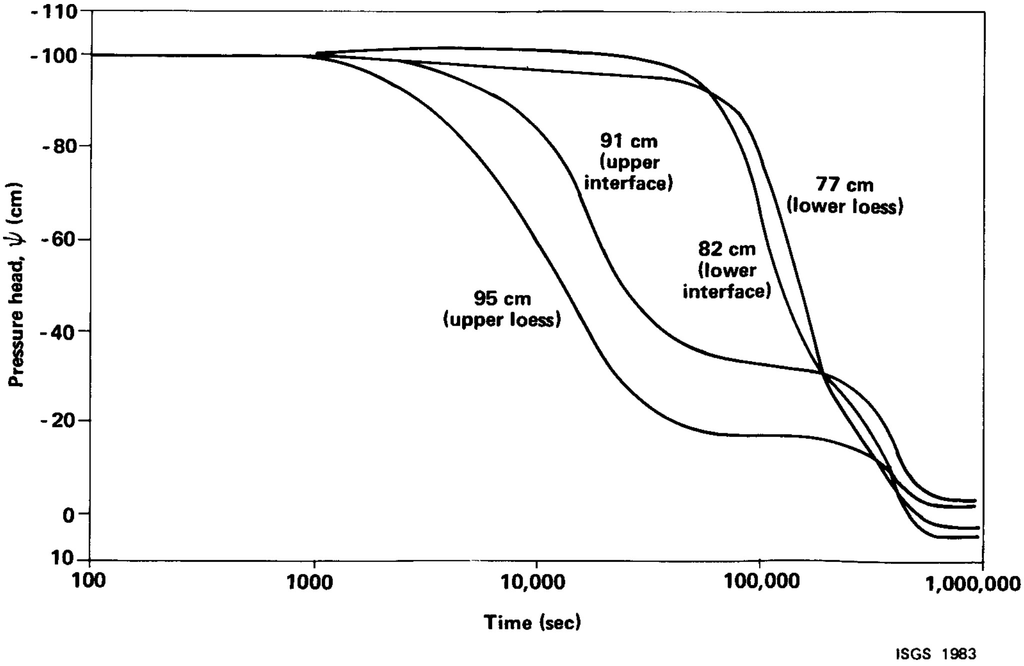

FIGURE 57. Predicted change in pressure head with time for various depths for Case 3 simulations, the three-layer column under conditions of constant ponding at the surface and constant pressure head = 0 (water table) at the bottom.

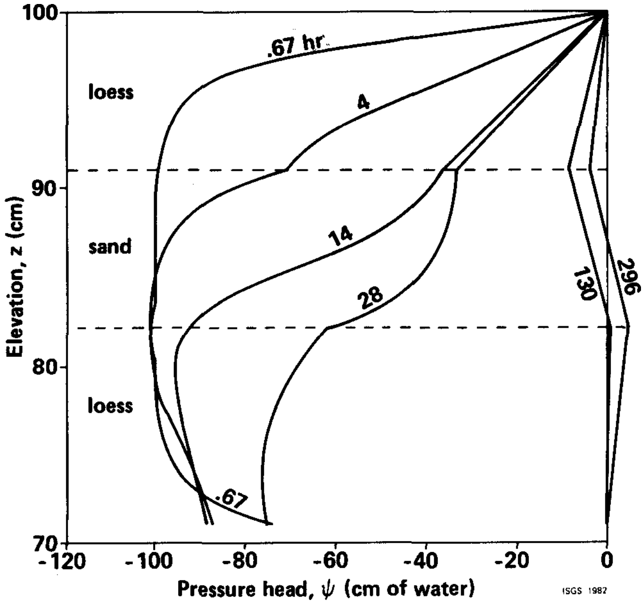

FIGURE 58. Predicted distribution of pressure head at selected times for Case 4 simulations, the three-layer column conditions of constant ponding at the surface and a seepage face at the bottom.

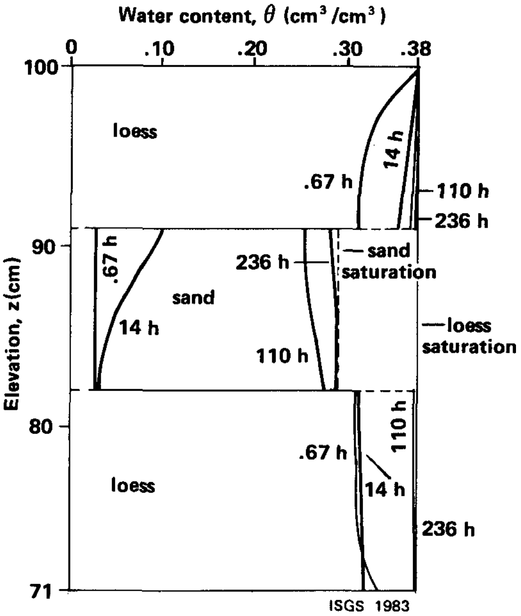

FIGURE 59. Predicted distribution of water content at selected times for Case 4 simulations, a three-layer column under conditions of constant ponding at the surface and a seepage face at the bottom.

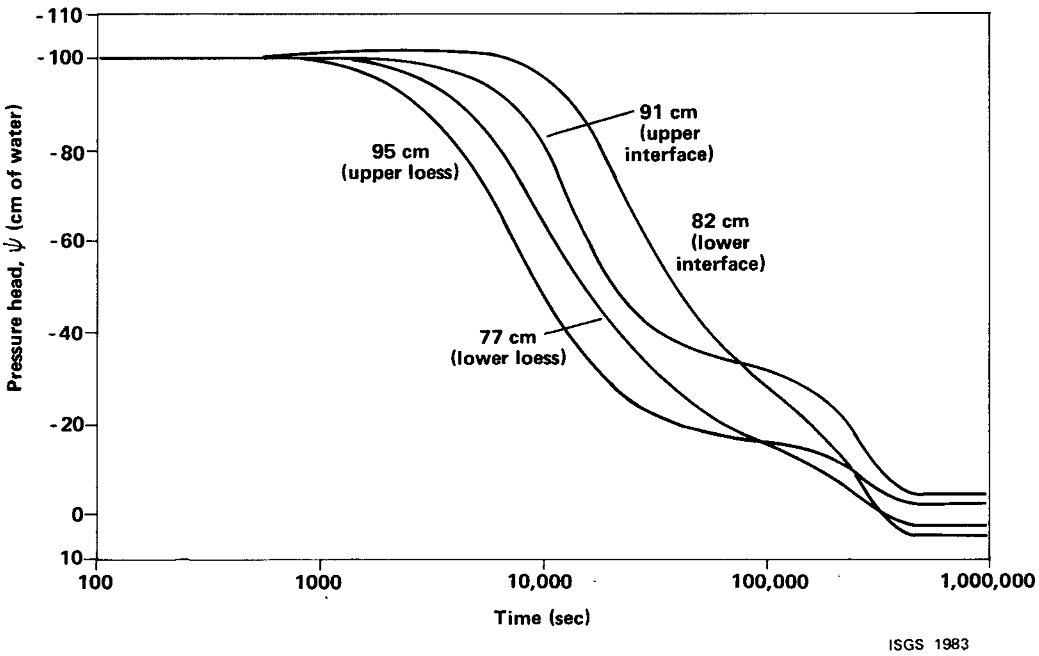

FIGURE 60. Predicted change in pressure head with time for various depths for Case 4 simulations, a three-layer column under conditions of constant ponding at the surface and a seepage face at the bottom.

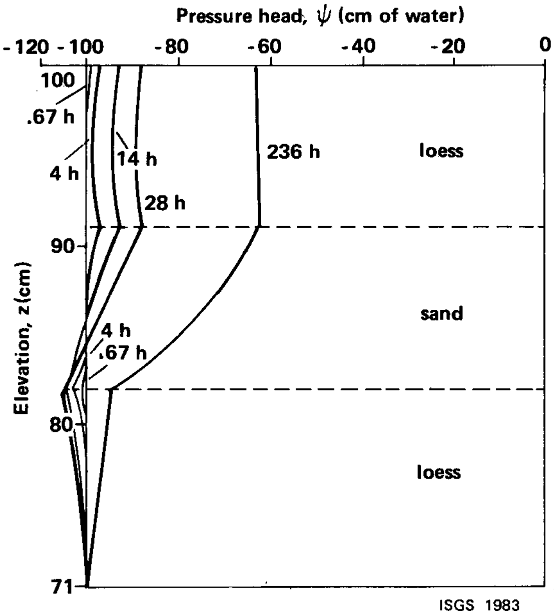

FIGURE 61. Predicted distribution of pressure head at selected times for Case 5 simulations, a three-layer column under conditions of constant discharge at the surface equal to the saturated hydraulic conductivity of the loess and constant pressure head = -100 cm of water at the bottom.

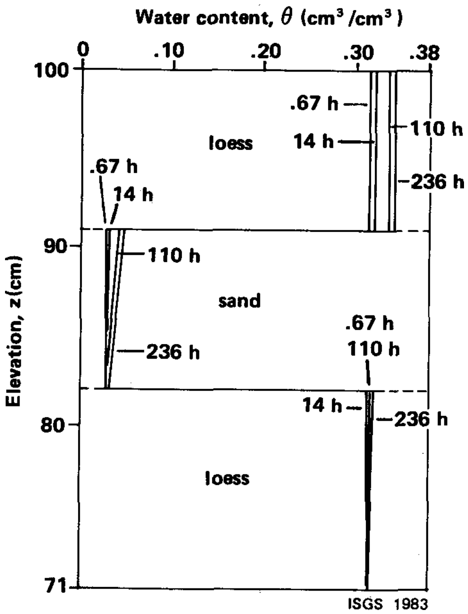

FIGURE 62. Predicted distribution of water content at selected times for Case 5 simulations, a three-layer column under conditions of constant surface discharge equal to the saturated hydraulic conductivity of the loess and constant pressure head = -100 cm of water at the bottom.

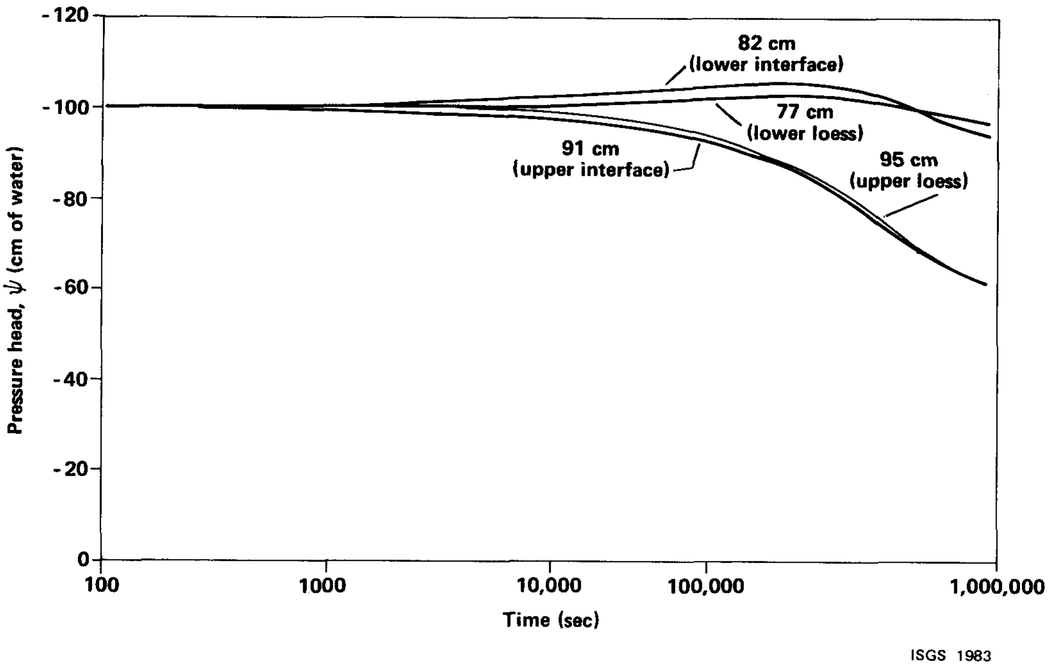

FIGURE 63. Predicted change in pressure head with time for various depths for Case 5 simulations, the three-layer column under conditions of constant discharge at the surface equal to the saturated hydraulic conductivity of the loess and constant pressure head = -100 cm of water at the bottom.

Figure 64 shows cumulative inflow for all five simulations. The inflow for the cases with a constant pressure-head boundary at the bottom is much less than that for those cases in which the bottom boundary was either continually saturated (case 3) or a seepage face (case 4). The cumulative inflow under constant ponding in cases 3 and 4 approached 28 cm at steady-state. All simulations appeared to approach inflow equilibrium after about 500,000 seconds.

Field-scale simulations

Infiltration and moisture movement through a hypothetical field-scale layered cover design was simulated using UNSAT2. The particular design chosen initially for modeling, figure 65, consists of three layers, each 60 cm thick. A single layer cover 180 cm thick was also simulated (case 1). The cover is assumed to be 6 m wide with a 5 percent slope of each layer from the center to the sides. It is anticipated that this will be the approximate configuration of one or more pilot-scale covers to be tested in the field. Since the hypothetical cover design in figure 65 is symmetrical, moisture movement through only half of the cover was modeled.

Figure 66 is a cross section of the sloping cover and superimposed finite element network used in the simulations. The region of interest was divided into 108 quadrilateral elements and 133 nodes (in the computer program each element is automatically divided into two triangles with identical, isotropic, material properties). The vertical dimensions of each element are smaller than the horizontal dimensions because of the relatively large vertical gradients expected to develop. The sides of the cover were assumed in all simulations to be no-flow boundaries. A constant pressure head of zero, indicating continual ponding, was imposed on the surface of the cover, while the boundary condition at the bottom varied in each case. Initial conditions within the cover consisted of a constant pressure head of -100 cm in each case described here.

The materials used in the field-scale cover simulations consisted of compacted Peoria Loess (P-2) and gravel (B). The saturated hydraulic conductivities of the loess and gravel were 2.0×10^{-6} cm/sec and 1.0 cm/sec, respectively. The desaturation moisture-retention curves for each material are presented in figure 47, and figure 48 illustrates the relationship between hydraulic conductivity and pressure head calculated by the method of Green and Corey (1971). The effects of hysteresis are not included in these simulations.

The magnitude of the first time-step in these calculations, $\Delta t'$, was 1 hour; subsequent time-steps increased gradually to a maximum of 3 hours. Convergence was assumed whenever the maximum change in Ψ at all nodes in the finite element network between two consecutive iterations in a time-step did not exceed 1 cm.

Case 1. In case 1, infiltration into a single-layer cover of compacted loess was simulated for a period of 297 hours of constant surface ponding. A constant pressure head of -110 cm was maintained at the bottom of the cover corresponding to its elevation above an arbitrary datum x and all interior nodes were assigned an initial pressure head of -100 cm.

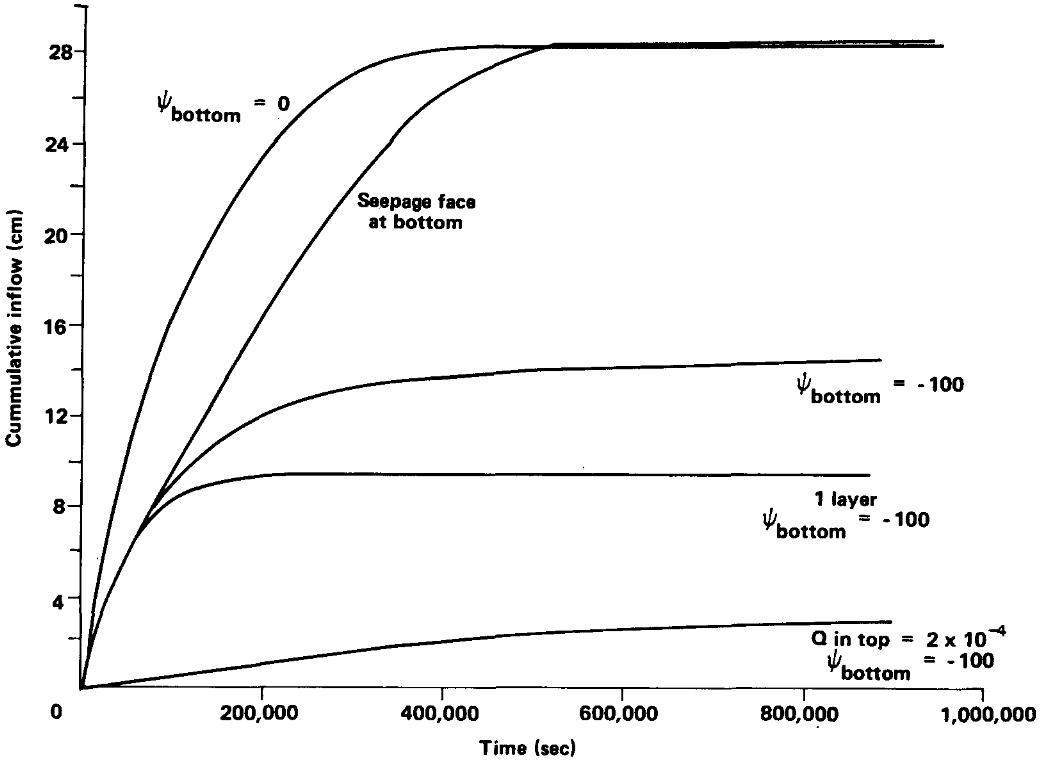

ISGS 1983

FIGURE 64. Predicted cumulative inflow as a function of time for all 5 cases of column simulations. Cases 1 and 2 have a boundary condition of $\Psi = -100$ cm at the bottom. Case 1 is a single-layer column while Case 2 is a three-layer column. In Case 3, the bottom of the three-layer column remains saturated. Case 4 has a seepage face at the bottom of the three-layer column. A constant surface flux is maintained in Case 5 with a boundary condition of $\Psi = -100$ cm of water at the bottom.

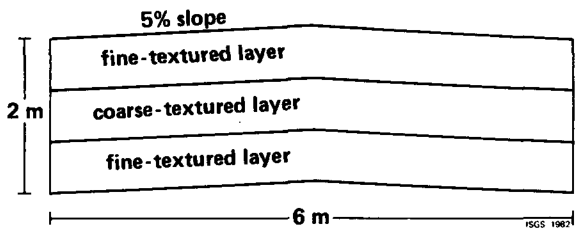

FIGURE 65. Cross section of hypothetical field-scale cover design.

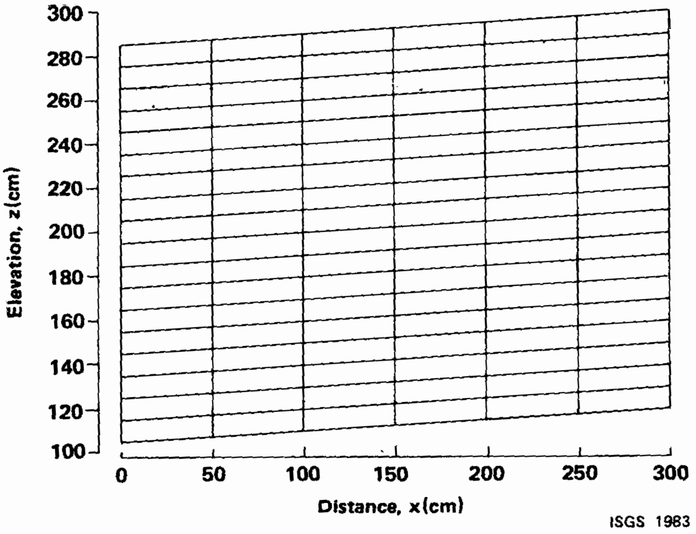

FIGURE 66. Cross section of one-half of symmetrical simulated field-scale cover with superimposed finite element network.

The wetting front in the single layer case propagates uniformly through the cover until steady-state conditions are attained. The vertical distribution of pressure head with depth at various times is shown in figure 67 at a position 100 cm from the left edge of the cover. The vertical change in water content with time at the same location is shown in figure 68. After 297 hours the wetting front has penetrated to a depth of more than 140 cm in this part of the single layer cover.

Case 2. The introduction of a coarse-grained, unsaturated layer between two layers of loess had a significant effect on infiltration and moisture movement in the cover. The simulations in case 2 utilized the same boundary conditions as in case 1; however, the cover in case 2 consisted of 60-cm layers of loess (P-2) overlying gravel (B) which in turn overlies loess (P-2).

As was shown by the one-dimensional simulations using MOMOLS, moisture movement in the loess overlying the gravel temporarily ceased once the interface was reached. The lack of moisture movement across the interface caused pressure heads and water contents to build up in the overlying layer. As shown earlier, pressure heads and moisture contents increase until the interfacial pressure reached a critical maximum value, Ψ_c. If Ψ_c was reached at the interface, the wetting front progressed rapidly into and through the coarse layer. In the one-dimensional simulations it was found that rapid infiltration into the gravel layer depleted moisture at and directly above the interface, and as a result pressure heads at the interface dropped quickly from Ψ_c to a value that was more or less maintained for the remainder of the simulation. As will be shown later, moisture content and pressure head build up in the upper layer of the simulated cover above the gravel until a critical pressure, Ψ_c, is reached and the wetting front rapidly penetrates the gravel. However, in the two-dimensional simulation, pressure heads at the interface did not drop appreciably immediately following moisture breakthrough, but remained virtually constant at the interface and in the underlying gravel.

The effects of a layered cover on infiltration are graphically illustrated in figure 69, in which the predicted distribution of pressure head at selected times in the three-layer cover is compared to that predicted for the single layer cover of case 1. Boundary conditions are the same in both cases. Especially noticeable is the increase in pressure head above the gravel layer and lack of movement into the gravel for more than 162 hours of ponding. Also apparent is the further decrease in pressure head below the gravel in response to the initial gradient applied to the system and the lack of moisture movement from the gravel into the underlying layer. It should be noted that, following breakthrough, the moisture front progresses much more rapidly through the gravel than in the one-layer case because of the higher degree of saturation in the upper layer of the three-layer case.

The predicted vertical distribution of pressure head and moisture content at several selected times are presented in figures 70 and 71 for the column of nodes at the position x = 100 cm in the cover (fig. 66). Moisture breakthrough into the gravel layer occurred quite suddenly after approximately 180 hours of moisture buildup in the overlying layer. After 382 hours, pressure heads in the gravel layer have increased substantially and the overlying loess is very nearly saturated; however, the water content of the gravel is still very low. Pressure heads in the loess beneath the gravel, however, have begun to increase after 382 hours.

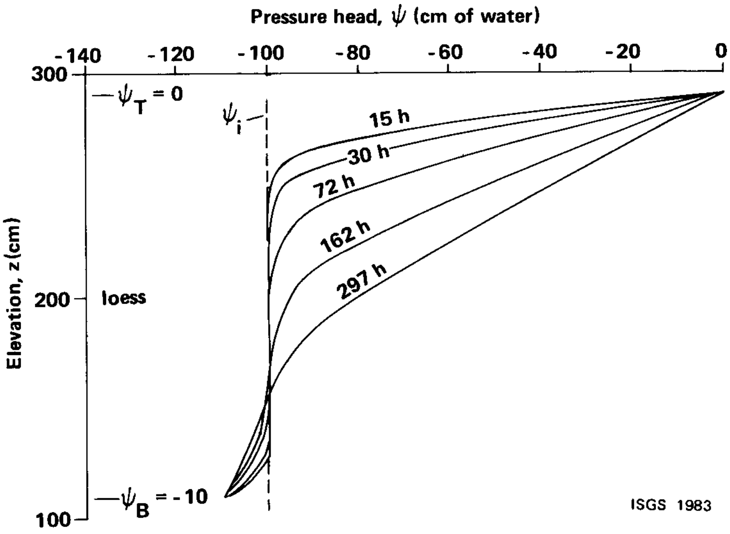

FIGURE 67. Predicted distribution of pressure head at selected times in a one-layer cover of Peoria Loess (P-2) at x = 100 cm under conditions of constant surface ponding and constant pressure head = -z at the bottom (Case 1).

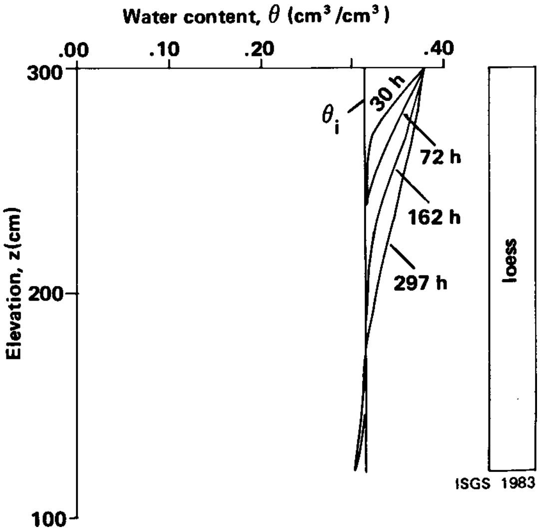

FIGURE 68. Predicted distribution of water content at selected times in a one-layer cover of Peoria Loess (P-2) at x = 100 cm under conditions of constant surface ponding and constant pressure head = -z at the bottom (Case 1).

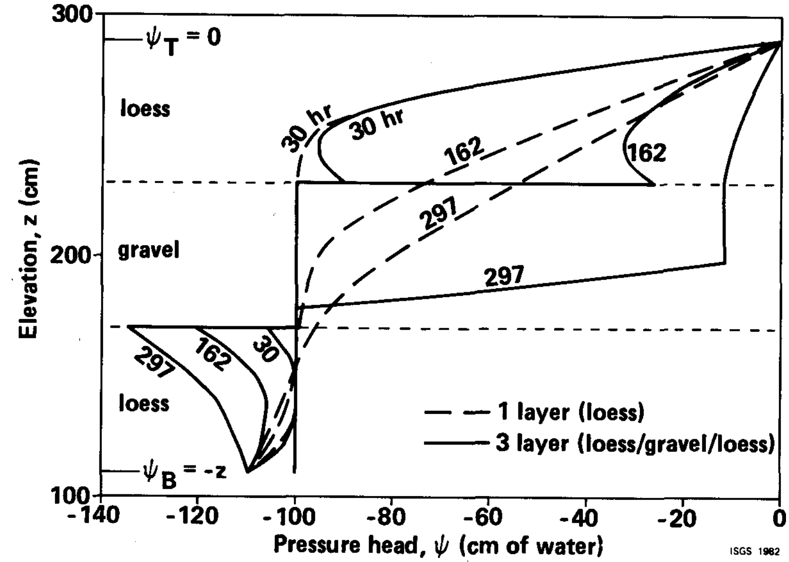

FIGURE 69. Comparison of predicted distribution of pressure head at selected times in a one-layer cover of Peoria Loess (P-2) and in a three-layer cover of Peoria Loess (P-2), gravel (B) and Peoria Loess (P-2) at x = 100 cm under conditions of constant ponding at the surface and constant pressure head = -z at the bottom (Case 2).

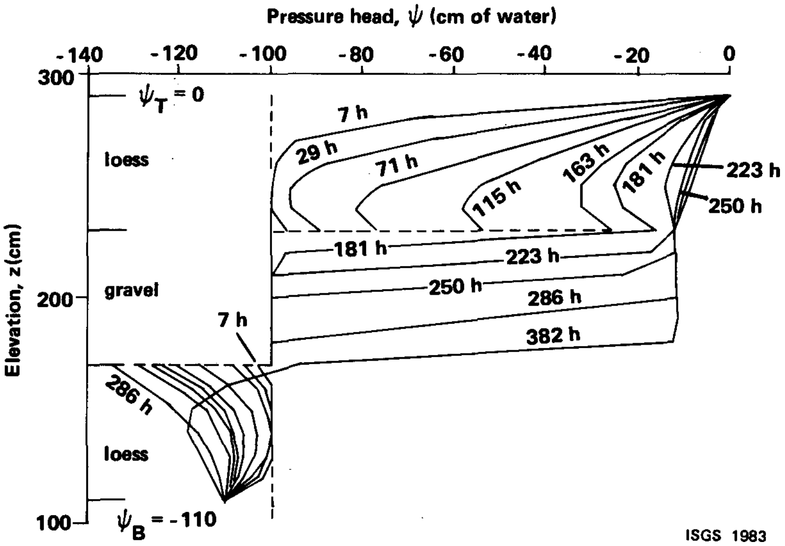

FIGURE 70. Predicted distribution of pressure head at selected times in the three-layer cover at x = 100 cm under conditions of constant ponding at the surface and constant pressure head = -z at the bottom (Case 2).

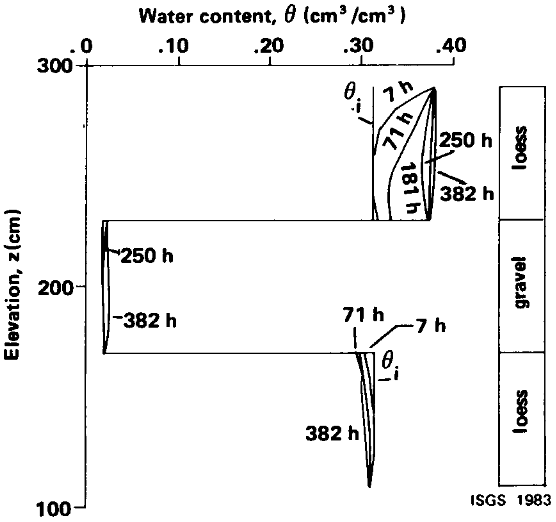

FIGURE 71. Predicted distribution of soil water content at selected times in the three-layer cover at x = 100 cm under conditions of constant ponding at the surface and constant pressure head = -z at the bottom (Case 2).

The layered cover system has a slope of 5 percent (4.5^{o}). The effects of this slope on moisture flow are illustrated in figures 72, 73, and 74, which show the predicted distribution of total hydraulic head in the cover. Initial hydraulic head conditions at the onset of ponding at the surface are shown in figure 72. The initial gradient associated with the assumption of a constant initial pressure head for the entire system is apparent. The head distribution after 162.5 hours (fig. 73) shows the buildup in pressure head and moisture content above the gravel layer; the vertical gradient in total head at the interface is significant. The presence of a lateral component of flow in response to the slope of the cover is also apparent in both the upper and lower loess layers. Although the loess is still unsaturated, some of the moisture that builds up in the upper layer of loess begins to move laterally through the loess above the gravel. The no-flow boundary along the edge of the cover stops this lateral flow; however, it may be possible to direct this lateral movement of infiltration off the trench cover through the fine-grained layer overlying the gravel. Future efforts will investigate this phenomenon.

The breakthrough of the moisture front into the gravel is shown in figure 74, which presents the total predicted hydraulic head distribution in the cover after 382 hours of surface ponding. The maximum vertical head gradient is now at the base of the gravel, and there is no predicted lateral flow in the loess overlying the gravel once breakthrough has occurred. Infiltration into the upper loess and gravel has become nearly vertical. Lateral flow of moisture is still apparent in the lower layer of loess into which the wetting front has not yet progressed.

Case 3. The system modeled in case 3 is identical to that in case 2 except for the boundary condition at the bottom of the cover. In case 3 the pressure head of zero was held constant at the bottom of the three-layer cover. This corresponds to saturated conditions in the waste beneath the cover.

The principal effect of this boundary condition is that, given the initial conditions, significant upward flow of moisture into the lower layer of loess occurs in response to pressure head gradients. Figure 75 illustrates the predicted vertical pressure head distribution at 14 hours and 139 hours for the column of nodes at x = 100 cm. As shown in the previous cases, however, the gravel layer forms a barrier to moisture flow because of contrasts in unsaturated hydraulic conductivity with the overlying fine-grained layer. The same phenomenon is shown in case 3 to limit the upward flow of moisture from the water table. Figure 76 shows the total head distribution in the cover after 13.9 hours. As expected, the wetting front has not progressed very far below the surface; however, the upward flow from the saturated base of the cover into the loess is readily apparent. This upward flow also results in a significant lateral component of flow toward the edge of the cover, partly because of the downward gradient initially imposed on the system. The onset of lateral flow in the loess overlying the gravel is also already evident after 13.9 hours.

Case 4. Case 4 incorporates a possible seepage face at the bottom of the three-layer cover. As indicated previously, the seepage face behaves as a no-flow boundary as long as the boundary remains unsaturated; however, once the boundary is saturated, seepage occurs in response to hydraulic gradients and atmospheric conditions.

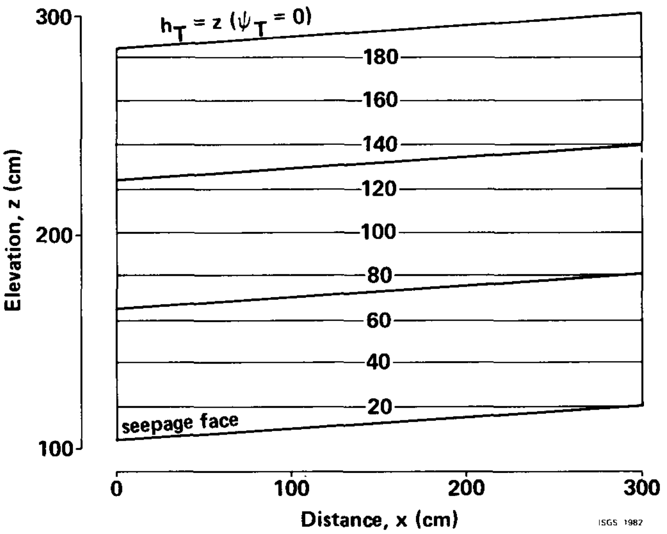

FIGURE 72. Initial distribution of total hydraulic head (cm) in the three-layer cover corresponding to a constant initial pressure head of -100 cm (Case 2).

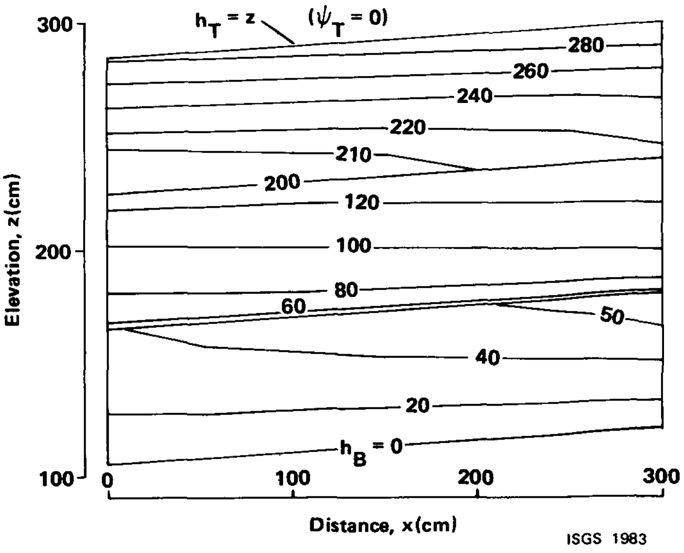

FIGURE 73. Predicted distribution of hydraulic head (cm) in the three-layer cover under conditions of constant surface ponding and constant pressure head = -z at the bottom after 162.5 hours (Case 2).

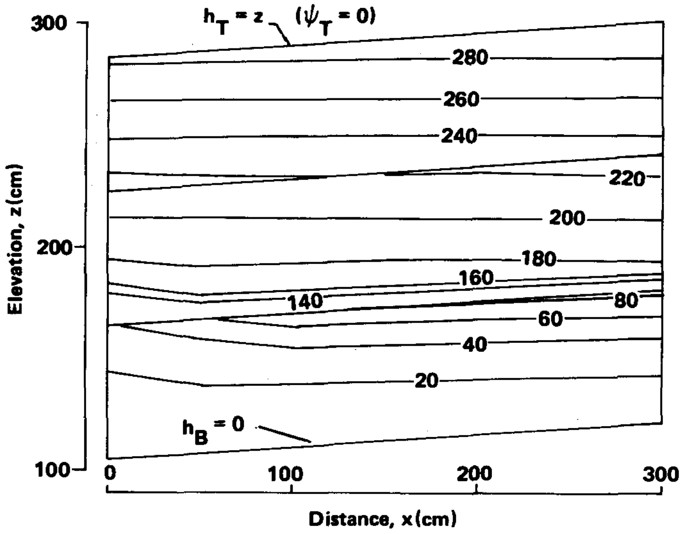

ISGS 1983

FIGURE 74. Predicted distribution of hydraulic head (cm) after 382 hours in the three-layer cover under conditions of constant surface ponding and constant pressure head = -z at the bottom (Case 2).

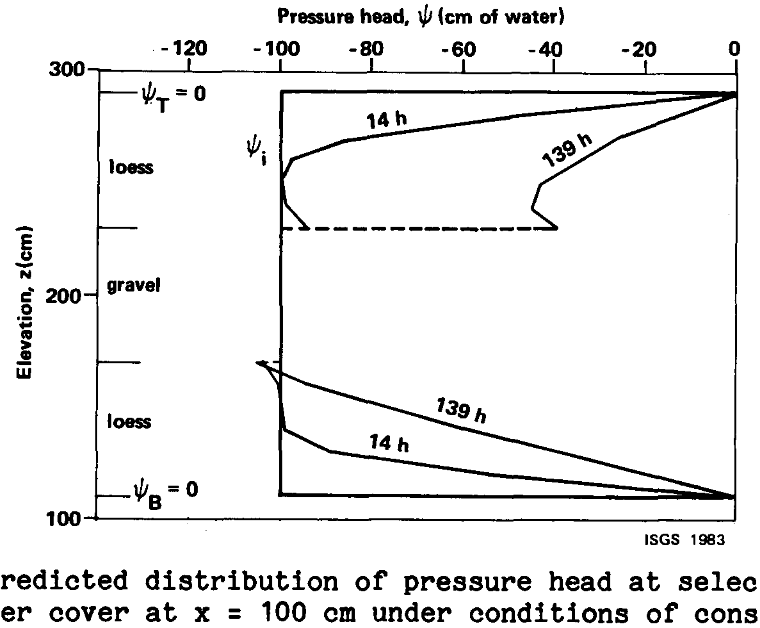

ISGS 1983

FIGURE 75. Predicted distribution of pressure head at selected times in the three-layer cover at x = 100 cm under conditions of constant ponding at the surface and constant pressure head = 0 (water table) at the bottom (Case 3).

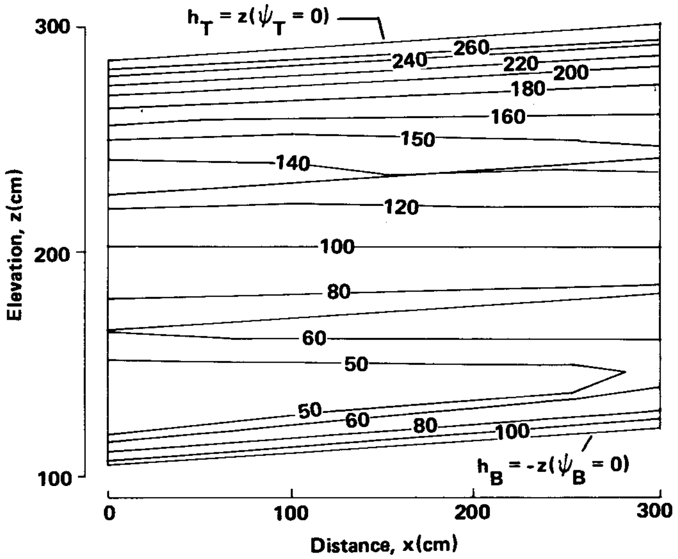

ISGS 1983

FIGURE 76. Predicted distribution of hydraulic head after 13.9 hours in the three-layer cover under conditions of constant ponding at the surface and constant pressure head = 0 (water table) at the bottom (Case 3).

Figures 77 and 78 illustrate predicted vertical distributions of pressure head and moisture content at selected times for the column of nodes at the right edge of the cover at x = 300 cm. These results are quite similar to those for cases 2 and 3 in the upper two layers. However, the seepage face at the bottom of the cover in case 4 is initially unsaturated and, therefore, initially represents a no-flow boundary. Pressure head in the bottom layer, which initially was assumed to be -100 cm throughout, attains a steady-state distribution until the wetting front reaches it after approximately 286 hours. As in case 2, the pressure head in the gravel attains a relatively constant value (Ψ_c) equal to that at the interface with the overlying loess. The moisture content of the gravel remains quite low, however, and increases significantly only when the wetting front had penetrated the entire system.

The distribution of total hydraulic head in the three-layer cover with a seepage face at the bottom is shown after 171 hours and 289 hours in figures 79 and 80. The total head distribution after 171 hours in figure 79 shows conditions immediately prior to moisture breakthrough into the gravel layer. Very sharp vertical gradients are evident at the interface of the upper loess and the gravel. As in cases 2 and 3 there is a lateral down-slope component of moisture flow in the loess overlying the gravel prior to moisture breakthrough; there is also a noticeable lateral gradient in the bottom layer because of the slope and no-flow nature of the unsaturated seepage boundary. Figure 80 shows the predicted distribution of total head after 289 hours. The moisture front has penetrated the gravel layer and there is no longer any noticeable lateral component of flow in the loess overlying the gravel; however, some apparent lateral flow occurs within the gravel layer and in the underlying loess.

Figure 81 shows the predicted changes in pressure head as a function of time at four positions within the cover system in case 4. Pressure heads increase steadily corresponding to increasing water content, in the upper layer of loess, approaching zero saturation 10 cm below the surface. At the interface between the upper loess and the gravel, pressure head begins to rise after 1 hour and increases rapidly after about 30 hours. However, when the pressure head increases to approximately 12 cm (Ψ_c), moisture breakthrough into the gravel occurs and the pressure head at the interface remains constant during the remainder of the simulation. In the gravel, 10 cm below the interface, the pressure head remains at the initial pressure of -100 cm until the moisture front passes after approximately 170 hours and the pressure head increases rapidly to that measured at the interface above. Subsequently, the pressure head in the gravel also remains constant throughout the remainder of the simulation. The pressure head at the interface of the gravel and the underlying loess, on the other hand, decreases steadily after about 1 hour in response to redistribution of moisture from the initial condition of constant pressure head of -100 cm, to a steady-state distribution of no-flow.

Figure 82 shows the predicted cumulative inflow into each cover system under conditions of constant surface ponding. Maximum inflow occurs in case 3 with a constant pressure head, $\Psi = 0$, at the bottom of the cover. In that case inflow from the water table at the base of the cover is significant, in response to initial conditions. Cumulative inflow in case 4 with a seepage face is significantly less due to the no-flow boundary at the bottom, which existed throughout the simulation. Cumulative inflow was the least for cases 1 and 2 in which a constant pressure head was maintained at the bottom of the

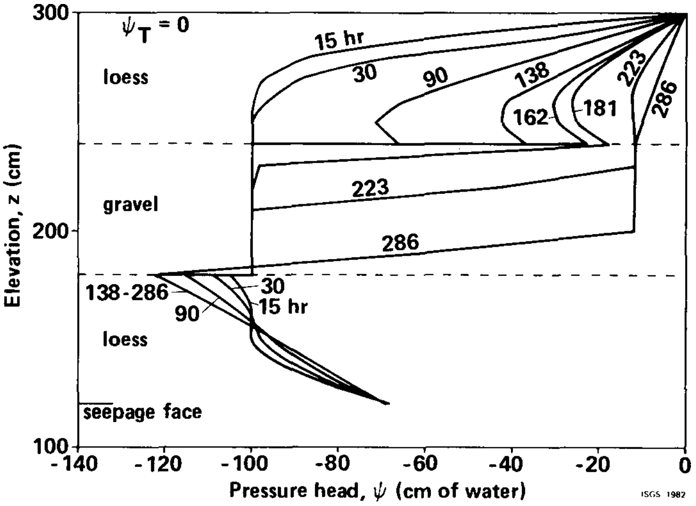

FIGURE 77. Predicted distribution of pressure head at selected times in the three-layer cover at x = 300 cm under conditions of constant ponding at the surface and a seepage face at the bottom (Case 4).

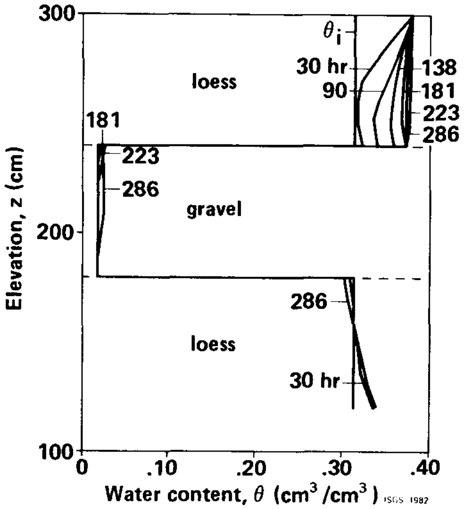

FIGURE 78. Predicted distribution of soil-water content at selected times in the three-layer cover at x = 300 cm under conditions of constant ponding at the surface and a seepage face at the bottom (Case 4).

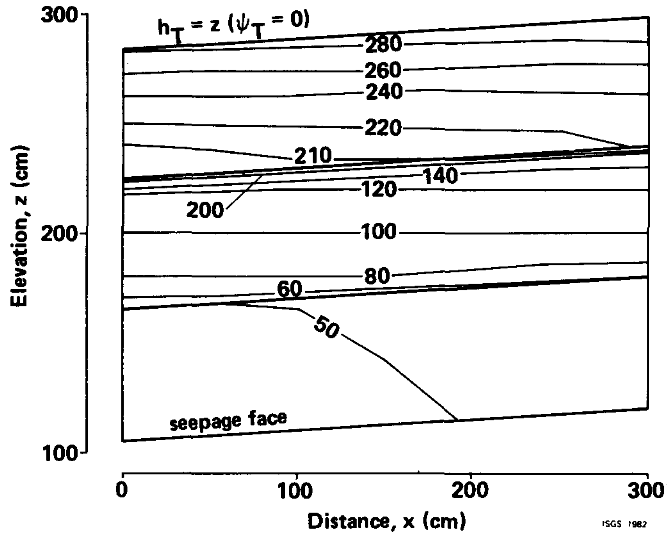

FIGURE 79. Predicted distribution of hydraulic head (cm) after 171 hours in the three-layer cover under conditions of constant ponding at the surface and a seepage face at the bottom (Case 4).

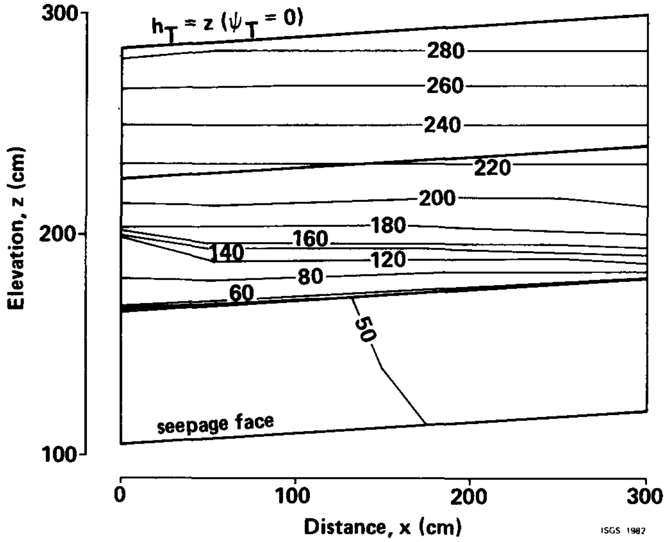

FIGURE 80. Predicted distribution of hydraulic head (cm) after 289 hours in the three-layer cover under conditions of constant ponding at the surface and a seepage face at the bottom (Case 4).

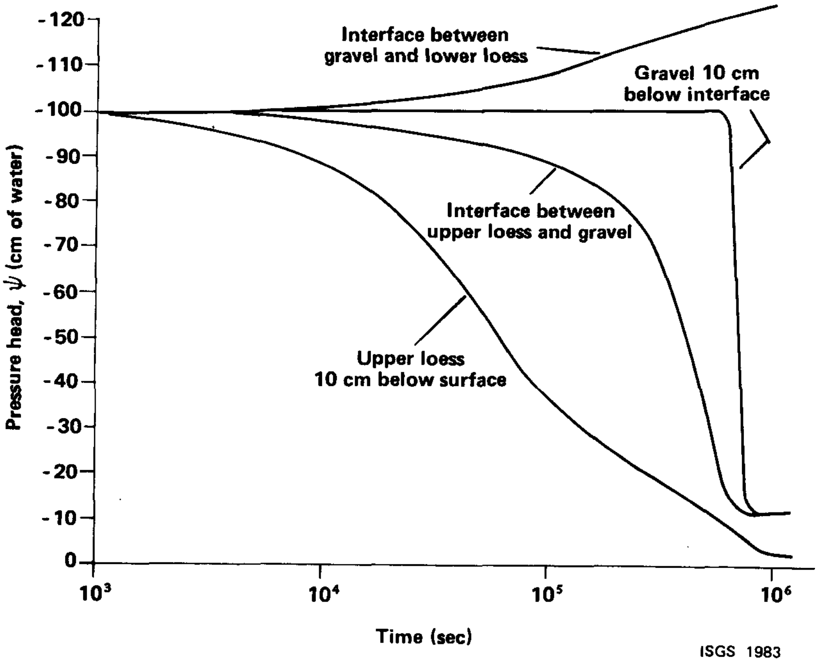

FIGURE 81. Predicted changes in pressure head with time at selected positions in the three-layer cover under conditions of constant ponding at the surface and a seepage face at the bottom (Case 4).

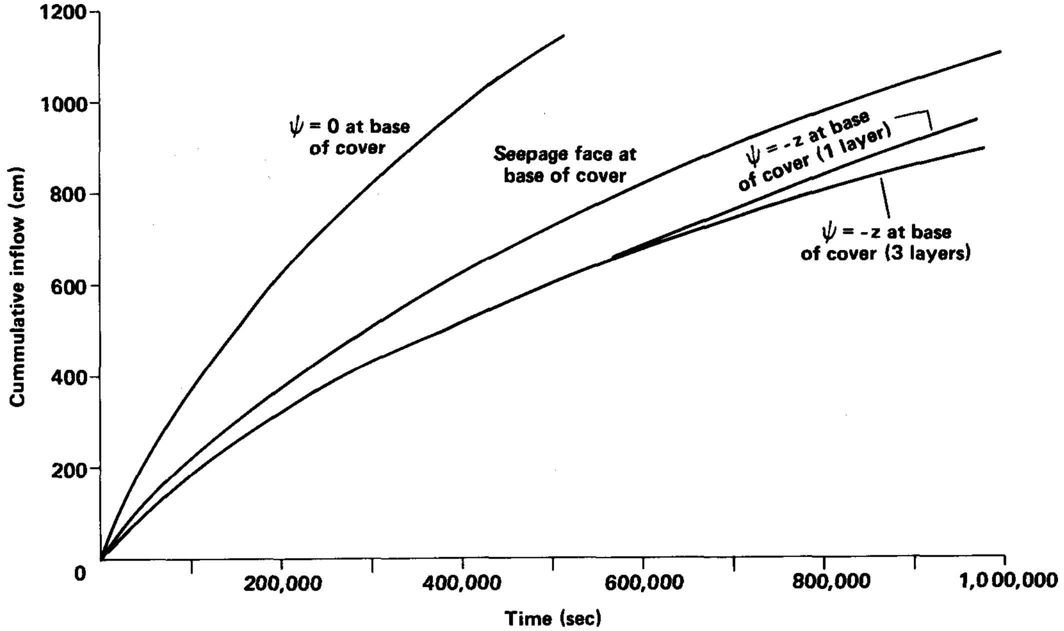

ISGS 1983

FIGURE 82. Predicted cumulative inflow as a function of time for field-scale simulations. In Cases 1 and 2, a boundary condition of constant pressure head $\psi = -z$ is maintained at the base of the covers. Case 1 consists of a single-layer cover while Case 2 consists of a three-layer cover. In Case 3, the base of the three-layer column remains saturated ($\psi = 0$). Case 4 has a seepage face at the base of the three-layer cover.

cover equal to the elevation at that point. In these cases an initial gradient applied to the system results in flow out the bottom of the cover from the bottom layer of loess. The cumulative inflow for the 1-layer and 3-layer cases is very similar for the first 560,000 seconds (6.5 days) because of the accumulation of water within the 1-layer cover and the upper layer of the 3-layer cover. Subsequently, the inflow into the 3-layer cover begins to decrease significantly because of the presence of the gravel layer. For the period of simulation steady-state inflow was not achieved for any of the cases.

IV. FIELD TEST OF SELECTED COVER DESIGNS

Based on the results of laboratory tests and computer modeling, four layered-soil cover designs were selected for field-scale tests in experimental trenches at the Sheffield, Illinois, study site. Construction of the experimental trench covers was scheduled to be completed in the spring of 1983. The approximately 1-hectare (2.5 ac) study site in Bureau County, approximately 250 km (150 mi) northwest of Champaign, is located adjacent to the closed Sheffield low-level radioactive waste disposal site.

The geologic materials selected for detailed laboratory testing and computer simulation were selected based on their similarity to materials already tested and their actual presence in the vicinity of the study site. These geologic materials include Peoria Loess, a windblown silt common in Illinois and present near the study site, which has been used in covers at the adjacent Sheffield waste-disposal site. The fine-grained Fairgrange Till of Wisconsinan-age included in laboratory tests and computer simulations is genetically related to and has physical properties similar to the Tiskilwa Till found near the field study site. The fine-grained materials actually used in construction of the experimental trench covers consist of Peoria Loess and Tiskilwa Till. The coarse-grained material used in the trenches is pea gravel.

The four experimental layered tench covers, each identical in size, are approximately 6 m (20 ft) wide and 15 m (50 ft) long. Each cover is installed within a shallow trench excavated to a depth of 90 cm (3 ft). The width and thickness of the experimental covers are virtually identical to those used in the two-dimensional, field-scale simulation described in Section III.G. of this report. Figure 83 presents a cross section of the experimental trench covers. The base of the trenches slope 5 percent toward the center and 5 percent longitudinally (toward the north) so that any water which penetrates the cover can be collected. The bottom of each trench is lined with an impermeable PVC plastic liner to prevent moisture movement into or out of the surrounding soils. A polypropylene filter geofabric was used above and below the plastic liner to protect the liner during construction. A 30 cm (1 ft) layer of pea gravel with drains simulates stable waste and constitutes a base for the overlying trench cover. Geofabric is used to separate the gravel from the overlying compact soil.

A 60-75 cm (2-2.5 ft) thick layer of Tiskilwa Till, compacted 2 percent wet of optimum, fills each trench. Compacting till at a moisture content wet of optimum should further decrease its hydraulic conductivity.

Cross section of layered trench cover (No. 1 and 2)

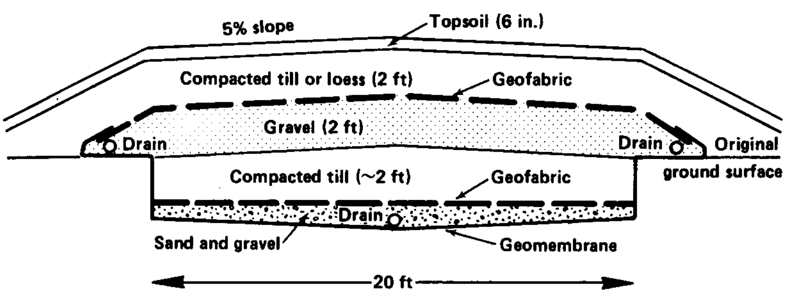

ISGS 1982

Cross section of layered trench cover (No. 4)

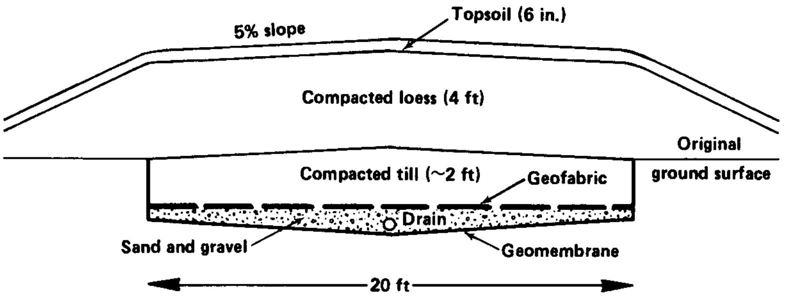

ISGS 1982

FIGURE 83. Cross sections of experimental trench covers. The upper layer in cover no. 1 is till while the upper layer in cover no. 2 is loess. Cover no. 3 is similar to cover no. 2 except that the gravel layer in cover no. 3 is only 1 foot thick and the overlying loess is 3 feet thick.

For Cover 1, the middle layer is 60 cm (2 ft) of pea gravel. Geofabric is used again above the gravel to maintain the interface with the overlying fine-grained material. The top layer is 60 cm (2 ft) of Tiskilwa Till, compacted 2 percent dry of optimum. This layer is compacted dry of optimum to increase its capacity to store water for subsequent evapotranspiration.

Cover 2 is designed to test the importance of the contast in hydraulic conductivity between the upper, fine-grained layer and the intermediate, coarse-grained layer. In this cover, Peoria Loess, compacted 2 percent dry of optimum is substituted for the Tiskilwa Till in the Upper layer. The loess/gravel sequence provides a saturated hydraulic conductivity contrast of 10^7 cm/sec, while the till/gravel sequence provides a contrast of 10^9 cm/sec.

The effects associated with varying the thickness of the upper two layers will be studied in Cover 3. Cover 3 has the same composition as Cover 2 (loess over gravel over till), but the gravel layer is reduced to 30 cm (1 ft) in thickness and the loess is increased to 90 cm (3 ft) in thickness.

Cover 4 will be used to compare the proposed layered design to currently used cover designs. Cover 4 is modeled after the newer covers at the Barnwell, South Carolina site. It consists of 1.2 m (4 ft) of compacted Peoria Loess over 60 cm (2 ft) of compacted Tislikwa Till without an intermediate gravel layer.

All of the layers slope laterally 5 percent from the center of the trench and 5 percent longitudinally (to the north). A 15 cm (6 in) layer of top soil was placed over each cover as a rooting medium and then sown with a mixture of grasses.

Each of the experimental trench covers is instrumented to collect data on soil-moisture movement. Soil-moisture content is measured using a neutron moisture probe, tensiometers, and electrical resistance blocks. Samples of soil moisture will be collected at various depths within the covers using small porous-cup suction samplers to study the movement of chemical tracers applied during construction at different horizons in each cover.

V. SUMMARY

Materials selected for laboratory testing were chosen on the basis of availability and potential suitability for use in covers for waste disposal sites. The materials included: (1) loess, a wind-blown silt of glacial origin, common in Illinois, which has been used in covers at the existing waste disposal site in Bureau County, Illinois; (2) fine-grained glacial till of Wisconsinan age, which is also widespread in Illinois and, because it typically has a very low saturated hydraulic conductivity, is commonly used in covers and liners for waste disposal sites; and (3) various coarse-grained materials that might be used in drainage systems associated with a cover design. The physical, engineering, and hydrologic properties of these materials were determined with respect to their performance in trench covers.

A dual energy gamma-ray attenuation unit was constructed to provide for laboratory calibration and verification of numerical models. Changes in moisture content and density of a laboratory soil column can be measured simultaneously and nondestructively with the fully operational system. Testing with the single, high-energy source has been successful, and an initial 160-hour soil column experiment has yielded results consistent with one-dimensional simulations. Movement of moisture, under constant head, is inhibited for a substantial length of time by the presence of a large and sharply defined textural contrast in soil materials. Further testing of the low-energy source will result in the capability of dual energy operation of the system and verification of the movement of moisture within the clay-rich, variably dense, fine-textured layers of the simulated covers. Meanwhile, additional single-source experiments will provide more detailed information concerning moisture movement within the coarse-textured, constant-density layer of the simulated cover.

Computer simulations of several initial cover designs were conducted. A one-dimensional model (MOMOLS) was developed by Rojstaczer (1981) and used to evaluate the effects of material properties and various boundary conditions on infiltration, and a two-dimensional model (UNSAT2) developed by Neuman et al. (1975) was used to simulate flow in the laboratory column and in a preliminary field-scale cover. The modeling verified that a layer of coarse-textured, unsaturated material overlain by fine-grained material could serve as a barrier to moisture movement. The effectiveness of the barrier is related to the contrast in saturated hydraulic conductivity and texture between the two layers. It was also shown that moisture buildup in the fine-grained layer overlying the coarse-textured layer in a sloping cover will flow laterally downslope above the interface prior to breakthrough.

It has been suggested previously that saturation of the overlying layer is required before moisture breakthrough will occur in such layered systems. However, as shown by Richards (1950), Hillel and Talpaz (1977), Rojstaczer (1981) and others, the simulations in this study indicate that moisture movement through layered systems of highly contrasting texture can occur when the moisture content of the overlying layer is less than saturation and the pressure head at the interface is less than zero. The significance of these results must be evaluated in reference to observed behavior in laboratory column and field experiments, and to limitations of instrument measurement of the parameters of interest.

Laboratory evaluation of fine-grained materials from the immediate vicinity of the proposed field-study site in Bureau County is underway in preparation for additional laboratory column experiments, more-refined computer modeling, and construction of actual pilot-scale trench covers. The actual materials to be tested consist of loess, till, and gravel very similar to those already characterized in laboratory tests.

Calibration and verification of the mathematical models with observed behavior in the laboratory column experiments are also underway. Previous simulations of moisture movement in layered, sloping cover systems described in this report have included only compacted loess, sand, and gravel, and have not yet simulated actual conditions of intermittent rainfall, evapotranspiration, or drainage of water from within the cover. Modeling currently underway incorporates these conditions in covers composed of loess, glacial till, and several types of coarse-grained materials with various slopes and boundary conditions. Specifically, the effects of slope and texture on the lateral flow and diversion of moisture through the upper layer and the efficacy of drains installed in the coarse-grained drainage layer will be investigated.

APPENDIX I. PROTOCOL FOR SAMPLE HANDLING AND METHODS OF ANALYSIS

The following protocol was established at the ISGS for sample handling and testing to provide reproducible results.

SAMPLE PREPARATION AND STORAGE

Samples for this study were collected at outcrops and from borings. Outcrop samples were taken by exposing a fresh face where the soils were moist, not on the dry face of the outcrop.

Bagged samples were stored in large insulated containers. This method limits the loss of water from the samples, and prevents change of material components due to dehydration.

Samples prepared for long-term storage were kept in a plastic container with water in the bottom, to maintain condition of near 100 percent humidity. Under these conditions, the potential for an increase in moisture content of the sample is slight. If a sample bag was broken, the sample was placed in a new bag.

For some tests, samples were prepared according to ASTM D421-58. Others were prepared without sieving and/or were not permitted to air dry.

Attention to sample handling and sample preparation is important for interpreting test results. Test results may differ because of the behavior of clay minerals and the hydration history. Making sure that soil minerals are hydrated prior to testing would be a complex undertaking involving petrographic and clay mineral analyses and a fundamental understanding of the hydration characteristics of all soil components. Some researchers (i.e., Sangrey et al., 1976, and Sherard et al., 1963) have noted significant changes in test results, due to the method of sample storage.

Samples for testing were permitted to dry by placing them outside, but not in direct sunlight. Indoors, samples were placed in a pan, mixed by hand, and periodically sampled for moisture content.

Wetting of the samples was accomplished by adding distilled water, mixing the soil by hand, and covering the sample to allow the samples to hydrate for several days.

ATTERBERG LIMITS

The Atterberg limits are tests for the liquid, plastic, and shrinkage limits of soils. Comparisons of results of these three tests with natural moisture content of the soils are made for inference of soil behavior in other tests. For most soils, the liquid limit exceeds the plastic limit, which in turn exceeds the shrinkage limit.

The Atterberg limits procedures are outlined, respectively, in ASTM D423-66, D424-59, and D427-61. Deviations from those procedures in our study were as follows:

a. Loess material was found to have marginal plasticity. An ASTM grooving tool was required to perform the liquid limit test for the loess. In addition, the technician was uncertain whether the soil slipped on the cup surface or if flow of the soil had occurred during the liquid limit test.

b. Till material was air-dried and disaggregated twice in both large and small jaw crushers. Particles larger than a number 40 sieve were removed. The finer fraction was "seasoned" with distilled water for 24 hours.

PARTICLE SIZE

The principal concerns in particle-size analysis are to look for gradation (skewness), more than one mode (kurtosis), and range of distribution. Excess or absence of material in a particle-size range influences soil behavior.

Particle-size analyses were done using a Micromeritics(R) SediGraph 5000D, particle-size analyzer. The machine uses an x-ray source to measure particle concentration by comparing the transmittance of the suspended soil with the transmittance of the suspending fluid.

Analysis by the SediGraph is comparable to that of the pipette method, according to tests run by the Illinois State Geological Survey.

SPECIFIC GRAVITY

Specific gravity of soil solids was approximated by calculations from the shrinkage factors tests, ASTM D427-61.

MOISTURE CONTENT

Moisture content was determined according to ASTM D2216-71 with the following changes:

a. Samples were dried in an open top container; no lids were used to cover the container after removal from the oven.

b. Samples and containers were weighed immediately upon removal from the oven.

c. All sample were oven-dried at 110o ± 5oC.

The natural moisture content gives an indication of the state in which the material presently exists.

MOISTURE-DENSITY RELATIONSHIP: COMPACTION TEST

Moisture-density relationships are crucial for the determination of the moisture at which a material can be compacted to its highest density under a given mechanical effort. This relationship also relates to the hydraulic conductivity of the material.

Two tests were used to study moisture-density relationships of soil materials:

Standard Proctor Test ASTM D698-78
Modified Proctor Test ASTM D1557-78

Loess samples were compacted using the Standard Proctor Test ASTM D698-78; however, the soil samples were not sieved prior to testing. The few large calcareous concretions in the soil were removed by hand. Moisture content was determined by sampling material from the mold. Compaction was by a manual hammer. Following the test, brass rings were either driven or pressed into the mold for hydraulic conductivity testing.

Scalping and replacement was necessary in order to achieve the proper volume of material for weighing. Replacement was made with the use of a laboratory spatula.

Glacial till samples were compacted according to specifications of the Modified Proctor Test, ASTM D1157-78, except that soil was not sieved prior to testing. The gravel in the sample constituted less than 10 percent of the sample by weight and was not removed. Some researchers have reported that removal of coarse-grained material by scalping significantly alters the density and moisture content of the material tested.

Moisture content was taken from material dug out of the mold. Some scalping and replacement was necessary in order to achieve the required volume for weighing. Replacement was made with a laboratory spatula.

Till materials compacted using this procedure could not be ejected from the mold by a screw-type ejector device designed for this purpose. Removal of compacted material was done manually by digging it out.

DISPERSION TEST

Dispersive soils are prone to severe piping and erosion. Treatment of the dispersive soils is necessary in order to preserve the integrity of the structure.

The dispersion characteristics of soils are determined from two tests: (1) the double hydrometer test, and (2) the pinhole test.

The double hydrometer test consists of two soil particle-size analyses using the hydrometer method; however, dispersant is added to only one column. The remaining column consists only of soil and distilled water.

The pinhole test was devised by the Soil Conservation Service (Sherard et al., 1976) in order to identify soils that would be unsuitable for dam construction. This procedure, with minor alterations, was used for our experiments. The cylinder used to hold the test specimen was the standard Harvard miniature compaction mold, which is slightly shorter than the SCS pinhole test apparatus. The soil specimen is the same size as that specified for the SCS test; however, the pea gravel filter is slightly reduced. We anticipate that this minor modification will not significantly alter the test results.

LINEAR SHRINKAGE

This is a sample test whereby soil is moistened and placed in a trough. The filled trough is permitted to air-dry, then oven-dry, and the amount of shrinkage is reported as a percentage of the original length. Samples will be prepared at various moisture contents and densities.

SWELL TEST

The swell test procedure is one designed for the Federal Housing Administration. The test measures the change in a soil sample that has been compacted into a mold in the testing apparatus. A porous stone and a platten are placed over the confined sample, and a proving ring and measuring device are then attached. As water is added and permitted to saturate the sample, the soil swells. The swelling of the soil exerts a pressure against the calibrated proving ring which is measured.

The test measures the uplift pressure (heave) and potential volume change. The test should be performed in moist conditions such as at optimum moisture content.

Scalping and replacement have been necessary for previous tests. Scalping has been performed with a straight-edge ruler. Replacement has been done with a laboratory spatula.

CLAY MINERAL ANALYSIS

Clay minerals are primarily responsible for swelling behavior in soils. The presence of unusual soil components existing in the material can be determined by clay mineral analysis.

Clay minerals were analyzed by x-ray diffraction methods. Samples were run as ground, whole rock, and less than 2 μm smears. Calculations of peak heights and areas on the diffractograms permit identification and estimation of proportions of clay minerals present. Nonclay mineral proportions are normalized to quartz.

FALLING HEAD PERMEABILITY

The saturated hydraulic conductivity was determined using a modified permeameter apparatus manufactured by Soiltest, Inc., Evanston, Illinois (Model K-620). Remolded soil samples are saturated and then a water pressure held constant by a storage tank and a flexible diaphragm with pressured air behind it. Water flows upward through the sample and rises in a standpipe decreasing the head loss across the sample. Since the decrease in head loss across the sample is small, the test can also be interpreted as a constant head test.

Samples were prepared using Harvard Miniature Compaction apparatus. The samples were compacted at selected moisture contents in a steel cylinder (33 mm in diameter and 72 mm high) using five lifts to obtain a predetermined dry density to prepare samples having the same porosity but having different moisture contents and dry densities. Consequently, the influence of the soil structure upon permeability can be investigated. Samples were prepared to densities of about 95 percent of the maximum density for the loess and 90 percent for the till, as determined from Standard Proctor compaction tests. The contact pressure of the tamper was 200 p.s.i. and the compaction energy required to produce samples of the desired density varied from 50,000 to 90,000 ft-lbs/cubic ft.

Samples were saturated by applying a vacuum to one end of the sample and water pressure to the other for at least 24 hours. Hydraulic gradients varied from 11 to 21.

MOISTURE CONTENT-CAPILLARY PRESSURE RELATIONSHIP

Measurements of the moisture content-capillary pressure relationship were performed using Tempe cells obtained from Soil Moisture Equipment Corp., Santa Barbara, CA (catalog no. 1400). Undisturbed or remolded specimens are placed in the cell, saturated and subjected to air pressure that is sequentially increased. The Tempe cell apparatus can be used up to a pressure of about 1000 cm of water (1 bar). Higher pressures require a ceramic plate or pressure membrane extractor. The reduction in weight is measured as the sample is desaturated, to investigate the moisture content-capillary pressure relation.

Till samples were compacted in brass rings approximately 54 mm in diameter and 30 mm high using the Harvard miniature compaction apparatus as described in the previous section. Loess samples were obtained by pushing rings of the same size into soil that had been compacted into a standard 1/30 cubic foot compaction mold.

For extraction of moisture at pressures from one to three bars, a pressure membrane extractor from Soil Moisture Equipment Corporation, catalog no. 1000, was used. Procedures for the pressure membrane extractor followed ASTM D3152-72 except for saturation of samples and compaction of remolded samples. The samples and the membrane were saturated before placement into the extractor. Remolded samples were compacted using the procedure described for the Tempe cells except that the samples were compacted in three lifts into P.V.C. cylinders (5.1 cm I.D., 1.1 cm high). After reaching equilibrium at one bar in the Tempe cell apparatus, some samples were transferred to the pressure membrane extractor in the brass Tempe cell retaining rings.

The same samples were used for all tensions as described in ASTM D3152, note 7.

REFERENCES

Brooks, R. H., and A. T. Corey, 1964, Hydraulic properties of porous media: Colorado State University Hydrology Papers, no. 3, 27 p.

Cary, A. S., B. H. Walter, and H. T. Howard, 1943, Permeability of Mud Mountain Dam core material: Transactions of the ASCE, v. 108, p. 719-737.

Elzeftawy, A., and K. Cartwright, 1979, Evaluating the saturated and unsaturated hydraulic conductivity of soils: ASTM Special Technical Publication 746, Philadelphia, Pennsylvania, p. 168-181.

Feddes, R. A., S. P. Neuman, and E. Bresler, 1975, Finite element analysis of two-dimensional flow in soils considering water uptake by roots: II. field applications: Soil Science Society of America Proceedings, v. 39, p. 231-237.

Green, R. E., and J. C. Corey, 1971, Calculation of hydraulic conductivity: a further evaluation of some predictive methods: Soil Science Society of America Proceedings, v. 35, p. 3-8.

Herzog, Beverly L. et al., 1981, A study of trench covers to minimize infiltration at waste disposal sites: Task I Report, Review of Present Practices and Annotated Bibliography: Illinois State Geological Survey Contract Rept. No. 1981-5, 245 p.

Hillel, D., and H. Talpaz, 1977, Simulation of soil water dynamics in layered soils: Soil Science, v. 123, no. 1, p. 54-62.

King, L. G., 1965, Description of soil characteristics for partially saturated flow: Soil Science Society of America Journal, v. 29, p. 359-362.

Lambe, T. W., 1954, The permeability of fine-grained soils: ASTM Special Technical Publication 163, Philadelphia, Pennsylvania, p. 56-67.

Lambe, T. W., 1960, Compacted Clay: structure: Transactions of the ASCE, v. 125, Part I, p. 682-716.

Lappala, E. G., 1980, Modeling of water and solute transport under variably saturated conditions: state of the art: Proceedings of the Interagency Workshop on Radioactive Waste Modeling, December, 1980, Denver, Colorado, Oak Ridge National Laboratory, Oak Ridge, TN, 57 p.

*

Marshall, T. J., 1958, A relation between permeability and size distribution of pores: Journal of Soil Science, v. 9, p. 1-8.

Millington, R. J., and J. P. Quirk, 1959, Permeability of porous media: Nature, v. 183, p. 387-388.

Mitchell, J. K., D. R. Hooper, and R. G. Campanella, 1965, Permeability of compacted clay: ASCE Journal of the Soil Mechanics and Foundations Division (JSMFD), v. 91, no. SM4, p. 41.

Mualem, Y., 1976, A new model for predicting the hydraulic conductivity of unsaturated porous media: Water Resources Research, v. 12, p. 513-522.

Mualem, Y., 1978, Hydraulic conductivity of unsaturated porous media: generalized macroscopic approach: Water Resources Research, v. 14, p. 325-334.

Narasimhan, T. N., 1975, A unified numerical model for saturated-unsaturated groundwater flows: Ph.D. dissertation, Department of Civil Engineering, Univ. of Calif., Berkeley.

Neuman, S. P., 1973, Saturated-unsaturated seepage by finite elements: Journal of Hydraulics Division of American Society of Civil Engineering, v. 99, HY12, p. 2233-2250.

Neuman, S. P., R. A. Feddes, and E. Bresler, 1975, Finite element analysis of two-dimensional flow in soils considering water uptake by roots: I. theory: Soil Science Society of America Proceedings, v. 39, p. 224-230.

Neuman, S. P., and T. N. Narasimhan, 1977, Mixed explicit-implicit iterative finite element scheme for diffusion-type problems: I. theory: International Journal for Numerical Methods in Engineering, v. 11, p. 309-323.

Nofziger, D. L., and D. Swartzendruber, 1974, Material content of binary physical mixtures as measured with a dual-energy beam of gamma-rays: Journal of Applied Physics 45 (12): 5443-5449.

Philip, J. R., 1957a, The theory of infiltration: 1. the infiltration equation and its solution: Soil Science, v. 83, p. 354-357.

Philip, J. R., 1957b, The theory of infiltration: 2. the profile at infinity: Soil Science, v. 83, p. 435-448.

Pickens, J. F., R. W. Gillham, and D. R. Cameron, 1979, Finite-element analysis of the transport of water and solutes in tile-drained soils: Journal of Hydrology, v. 40, p. 243-264.

Reeves, M., and J. O. Duguid, 1975, Water movement through saturated-unsaturated porous media: a finite-element Galerkin model: Oak Ridge National Laboratory, ORNL-4927, 232 p.

Richards, L. A., 1931, Capillary conduction of liquids through porous mediums: Physics, v. 1, p. 318-333.

Richards, L. A., 1950, Laws of soil moisture: Transactions, American Geophysical Union, v. 31, no. 5, p. 750-756.

Rojstaczer, S. A., 1981, Moisture movement through layered soils of highly contrasting texture: University of Illinois Master's thesis, unpublished, Urbana, IL, 86 p.

Sangrey, D. A., D. K. Noonan, and G. S. Webb, 1976, Variation in Atterberg Limits of soils due to hydration history and specimen preparation: Soil Specimen Preparation for Laboratory Testing, ASTM STP599, American Society for Testing and Materials, p. 158-168.

Santo, L. T., and G. Y. Tsuji, 1977, Soil bulk density and water content measurements by gamma-ray attenuation techniques: Hawaii Agricultural Experiment Station, University of Hawaii, Technical Bulletin 98.

Sherard, J. L., R. J. Woodward, S. F. Ginienski, and W. A. Clevenger, 1963, Earth-rock dams: John Wiley and Sons, New York.

Sherard, J. L., L. P. Dunnigan, R. S. Decker, and E. F. Steele, 1976, Pinhole test for identifying dispersive soils: Journal of the Geotechnical Engineering Division, American Society of Civil Engineers, p. 69-85.

Topp, G. C., 1969, Soil-water hysteresis measured in a sandy loam and compared with the hysteretic domain model: Soil Science Society of America Journal, v. 33, p. 646-651.

Topp, G. C., 1973, Soil-water hysteresis in silt loam and clay loam soils: Water Resources Research, v. 7, p. 914-920.

Topp, G. C., and E. E. Miller, 1966, Hysteretic moisture characteristics and hydraulic conductivities for glass-bead media: Soil Science Society of America Journal, v. 30, p. 156-161.

Yeh, G. T., 1982, Training course no. 1: the implementation of FEMWATER (ORNL-5567) computer program: U.S. Nuclear Regulatory Commission NUREG/CR-2705, ORNL/TM-8327, 163 p.

Yeh, G. T., and D. S. Ward, 1980, FEMWATER: a finite-element model of water flow through saturated-unsaturated porous media: Oak Ridge National Laboratory, ORNL-5567, 153 p.

* Liakopoulos, A. C., 1965, "Theoretical Solution of Unsteady, Unsaturated Flow Problems in Soils: Bulletin of the International Association of Scientific Hydrology, V. 10, p. 5-39.